M 2022

U.PORTO
FEUP FACULDADE DE ENGENHARIA
UNIVERSIDADE DO PORTO

MODELLING AND OPTIMIZATION OF ADSORPTION-BASED HEAT PUMPS

BEATRIZ CAMBÃO DA SILVA
MASTER THESIS IN CHEMICAL ENGINEERING
PRESENTED TO THE FACULTY OF ENGINEERING
OF THE UNIVERSITY OF PORTO

Master in Chemical Engineering

Modelling and optimization of adsorption-based heat pumps

Master dissertation

of

Beatriz Cambão da Silva

Developed within the course of dissertation

held in

LSRE – LCM – Laboratory of Separation and Reaction Engineering – Laboratory of Catalysis and Materials, part of ALiCE- Associate Laboratory in Chemical Engineering

Supervisor at FEUP: **Prof. Idelfonso Nogueira**

Joint supervisors at FEUP: **Prof. Alexandre Ferreira**

Prof. Ana Mafalda Ribeiro

July 2022

Acknowledgment

First of all, I would like to thank all people that walked alongside me in these last 5 years.

To my mum and dad, who always believed in me especially when I did not, and were always there during this path. To my brother who, unlike me, hates hugs but was always there with arms wide open when I most needed them to be. To my aunts, who would not rest until I ensure them I was fine with at least 3 different types of evidence.

To my outer family, whose eyes sparkle with pride as this journey gets closer to the end.

To my hometown friends “Friends 4evah”, who have been here since the early days. Even though we grew up to have so distinct personalities we remained like an intertwined yin-yang, where our flaws complement our qualities to emphasize the best in each other. Thank you for hearing all my complaints in life and being able to make me laugh through them. I would like to highlight my dearest friend Joana Faria, who knows me since I was 3 years old and has provided for countless adventures, both in life and on paper. She is the one to blame for my love for books and has offered herself multiple times to do video calls while we both had excel sheets to analyze so we could deal with our book abstinence.

To the members of “Stâdi sech”, that shared the despair hours in every exam season so far, being with the malfunctioning of the calculators or with the last-minute questions before stepping into the exam room. Thank you for making me a little bit less “Lost in the woods” in “Waterloo”.

To the team “MarketMasters”, my companions in case studies, with whom I have learned that life must be taken one step at a time and that we are all in the same boat so the best we can do is sail through the storms.

To Nuno Dias and Ana Sousa, for always cheering me up and remembering me that life is simple, and we are usually the ones who complicate it. Thank you for being here and for introducing me to the wonderful people of “COVIvio 19”. And for always knowing when I required a chocolate boost to enhance my creativity.

To Rita Borges, Marta Sacramento, Andreia Lopes, and Sérgio Santos for making studying in the first year of the course a joyful adventure.

To Beata Shymon and Sara Pestana for putting up with my burnouts during the pandemic season and reminding me that being away from people does not mean we are not close in heart.

To the Vixit family, for teaching me that despite the imposed rules we can always find a way to maintain our individuality.

To Rita Alfenim, who has been here for every fall I took and whose joy to live will always light up the room.

To the ones who understood the need of being close to the front line in the auditoriums.

To Luana Queiroz, who was my teammate during the dissertation, who walked through the bugs with me and always believed we would be here crossing the finish line.

To my lab partners in Lab E406, where the best scientific discussions were born, particularly "Impacts of anti-stress balls in the well-being of Ph.D. and Master students" and "Novel approach on afternoon treats in research development". Thank you for welcoming me into your family and always helping me put things in perspective.

To Professor Alexandre Ferreira, who presented me with the opportunity of realizing this dissertation on the day my world turned upside down. Thank you for the continuous support, the cultural sessions, and the certainty that I can always keep the "travesseiros de Sintra" for myself.

To Professor Ana Mafalda, who became my role model during this journey, by demonstrating it was possible to do everything we propose ourselves to, even if it means running miles a day. Thank you for the friendly words, and for instigating me to move forward whenever I got stuck in a problem.

To Professor Idelfonso Nogueira, who endured my existential crises through multiple clusterization methods and coding issues. Thank you for the knowledge provided, and for always being able to give an optimistic point of view. A special acknowledgment for introducing me to Carine Rebello, whose help in the study of optimization theory was crucial to the development of this work.

To the best person that FEUP has given me the chance to cross paths with, my boyfriend Manuel Monteiro. Thank you for always providing a safe space, for accepting my lunar side, and for showing me the importance of having the courage of taking the first step. Thank you for always being here to shed light in the darkest hour, for being the best medicine for my headaches, and for hearing me talk so much about this work that you were almost capable of reciting the variable list by heart.

And at last, to the ones who initiated this journey with me but to whom no more time on this planet was allowed. To my grandad João, to my grandmother Maria. I hope you are seeing this final chapter from up there. Thank you for being my stars.

To mark the end of this section, I leave three sentences that I have carried with me during these 5 years:

"To the stars who listen-and dreams who are answered" (Sarah J. Mass, A court of Mist and Fury)

"Even through your hardest days, remember we are all made of stardust" (Carl Sagan)

"Tudo fica bem no final. E se ainda não está bem é sinal que ainda não chegou ao fim" (Joana Faria)

The supervisors of this dissertation are members of LSRE-LCM - Laboratory of Separation and Reaction Engineering – Laboratory of Catalysis and Materials, financially supported by LA/P/0045/2020 (ALiCE), UIDB/50020/2020, and UIDP/50020/2020 (LSRE-LCM), funded by national funds through FCT/MCTES (PIDDAC).

Abstract

Adsorption heat pumps have a growing interest in the heat production field, posing a sustainable alternative to the traditional routes. The big disadvantage with this type of device is the lower performance compared to the more polluting alternatives. Therefore, material screening plays an essential role in the search for means to increase the heat production of the adsorption heat pumps. Most works in literature compare materials on a fixed-temperature basis or manual "optimization" of one of the temperatures involved. This work aimed to implement an optimization strategy, in this case, Particle Swarm Optimization, to optimize the material screening procedure by testing multiple temperatures at once and searching in the viable zones of operation for the optimal performance within a given adsorbent database.

Two objectives were defined, with those being the maximization of performance and the reduction of the cost of heat supply, evaluated in three different ways. In the first step, the performance was assessed individually, followed by a single-objective approximation of the multi-objective problem. At last, a multi-objective approach was adopted with the construction of a Pareto Front. The Fisher-Snedecor test was applied to compare the results obtained during PSO application with the optima points and built a Feasible Operating Region around those optima.

During the single-objective optimization, MIL-100 (Fe) and MIL-125_NH_2 (Ti) were pictured as the best performing materials, being able to deliver when the priority is performance and when there must be a balance between the cost and performance. In multi-optimization, MIL-160 (Al), Al-FUM, and AQSOA FAM-Z02 also revealed a reasonable performance. Thus, multi-optimization approach allowed for a broader evaluation of the materials when combined with the construction of the Feasible Operating Region. The optimization procedure also revealed a codependence between all the temperatures. With the particle values generated during the PSO implementation, it was possible to map the different sets of values that lead to higher performance with the lowest cost possible.

Keywords: Adsorption Heat Pumps, Particle Swarm Optimization, Material Screening, Water adsorption, Feasible Operating Region

Resumo

As bombas de calor de adsorção têm vindo a despertar interesse no campo da produção de energia calorífica, apresentando-se como uma alternativa sustentável às vias tradicionais. No entanto, um problema que é frequentemente apontado é o seu menor desempenho quando comparadas às bombas de calor mais poluentes. Um passo auxiliar na procura de meios que permitam aumentar o desempenho das bombas de calor baseadas em adsorção é a triagem e seleção dos adsorventes que podem ser aplicados nestes equipamentos. Grande parte das triagens presentes na literatura baseiam-se num conjunto fixo de valores de temperatura ou na variação manual de uma das temperaturas chave do processo. O objetivo desta dissertação foi implementar um método de otimização, neste caso o *Particle Swarm Optimization*, para melhorar o processo de seleção de materiais viáveis ao localizar as diferentes combinações de temperaturas que permitiam o melhor desempenho do sistema.

A otimização foi efetuada tendo em vista dois objetivos: a maximização do desempenho do sistema e a diminuição do custo de operação durante um ciclo. Estes objetivos foram avaliados de três maneiras distintas. A primeira consistiu na maximização do desempenho de forma individualizada. De seguida, foi feita uma abordagem aproximada do problema multiobjectivo por um problema de objetivo único. Por último, foi efetuada a abordagem de otimização multiobjectivo com a construção da curva de Pareto. Os pontos ótimos obtidos em cada uma destas abordagens foram transformados numa região ótima através do teste de Fisher-Snedecor.

Com os pontos dessa região ótima foi possível concluir que os materiais que apresentaram o melhor desempenho foram o MIL-100 (Fe) e MIL-125_NH_2 (Ti), que apresentaram a possibilidade de operarem tanto na zona de compromisso entre o custo e o desempenho como na zona de alto desempenho. Nas soluções apresentadas no problema multiobjetivo, o MIL-160 (Al), o Al-FUM e o AQSOA FAM-Z02 também revelaram a possibilidade de operar na zona de desempenho mediada com o custo, levando a uma melhor avaliação do sistema. Durante a otimização foi também possível observar uma co-dependência entre as temperaturas e com as partículas geradas foi possível mapear os diferentes valores que conduzem ao desempenho desejado.

Declaration

I, Beatriz Cambão da Silva, hereby declare, under word of honour, that this work is original and that all non-original contributions is indicated, and due reference is given to the author and source

Beatriz Cambão da Silva

Porto, 4th of July of 2022

Index

List of Figures

List of Tables

Notation and Glossary

a^v	Initialization factor of velocity	[-]
C_0	Acceleration coefficient	[-]
$C_{0,f}$	Final value of C_0	[-]
$C_{0,i}$	Initial value of C_0	[-]
C_1	Acceleration coefficient	[-]
C_2	Acceleration coefficient	[-]
CF	Coverage Factor	[-]
COP_{heat}	Coefficient of Performance for heating applications	[-]
$Cost$	Cost of an adsorption heat pump operating cycle	[€]
$Cost_{GN}$	Cost of natural gas	[€ GJ^{-1}]
$Cost_{IF}$	Cost with Impact Factor	[€]
$C_{p,water}$	Specific heat capacity of water	[J mol^{-1} K^{-1}]
$C_{p,ads}$	Specific heat capacity of the adsorbent	[J kg^{-1} K^{-1}]
EF	Equalization factor	[€]
G	Integration Constant	[-]
G_{best}	Vector of the best positions for global swarm	[-]
IF	Impact factor	[-]
k	Current iteration	[-]
K_0	Adsorption equilibrium constant of Ising-Langmuir isotherm	[bar^{-1}]
K_∞	Adsorption equilibrium constant of Ising-Langmuir isotherm	[bar^{-1}]
K_L	Adsorption equilibrium constant of Ising-Langmuir isotherm	[bar^{-1}]
$K_{o,\infty}$	Adsorption equilibrium constant of Ising-Langmuir isotherm at infinite temperature	[bar^{-1}]
$K_{I,\infty}$	Adsorption equilibrium constant of Ising-Langmuir isotherm at infinite temperature	[bar^{-1}]
$K_{L,\infty}$	Adsorption equilibrium constant of Ising-Langmuir isotherm at infinite temperature	[bar^{-1}]
LF	Loss factor	[-]
m_{ads}	Mass of adsorbent	[kg]
N	Number of points	[-]
$\mathrm{N_{DV}}$	Number of decision variables	[-]
$\mathrm{N_{exp}}$	Number of experiments	[-]
$\mathrm{N_{it\_max}}$	Maximum number of iterations	[-]
$\mathrm{N_{part\_max}}$	Maximum number of particles	[-]
P	Pressure	[bar]
P_{best}	Vector of the best positions for each particle	[-]
P_{cond}	Condensation Pressure	[bar]
P_{evap}	Evaporation Pressure	[bar]
q	Adsorbed amount	[mol kg^{-1}]
$q_{sat,L}$	Specific saturation adsorption capacity in Langmuir isotherm	[mol kg^{-1}]
$q_{sat,I}$	Specific saturation adsorption capacity in Ising isotherm	[mol kg^{-1}]
q_{max}	Maximum adsorbed amount	[mol kg^{-1}]
q_{min}	Minimum adsorbed amount	[mol kg^{-1}]
Q_{ads}	Heat of isobaric adsorption	[J]
Q_{cond}	Heat of condensation	[J]
Q_{cool}	Heat of isosteric cooling	[J]
Q_{des}	Heat of desorption	[J]
Q_{evap}	Heat of evaporation	[J]
Q_{heat}	Heat of isosteric heating	[J]
R	Ideal gas constant	[J mol^{-1} K^{-1}]
r	Random number	[-]

T	Temperature	[K]
T_2	Intermediate temperature	[K]
T_{ads}	Temperature of adsorption	[K]
T_4	Intermediate temperature	[K]
T_{cond}	Condensation temperature	[K]
T_{des}	Temperature of desorption	[K]
T_{evap}	Evaporation temperature	[K]
U	Uncertainty (Standard deviation within the Feasible Operating Region data)	[-]
$v_{i,n}$	Velocity for each particle in each decision variable	[-]
$v_{i,n,new}$	Updated velocity for each particle in each decision variable	[-]
w	Maximum violation rate	[-]
w_i	Parameter of Ising-Langmuir isotherm	[-]
w_L	Maximum violation rate for lower side constraints	[-]
w_U	Maximum violation rate for upper side constraints	[-]
$x_{i,n}$	Position for each particle in each decision variable	[-]
$x^*_{i,n,k}$	Candidate position	[-]
$x_{i,n,k}$	Accepted position	[-]
$x_{n,lower}$	Lower side constraints of decision variables	[-]
$x_n^{G_{best}}$	Guide position within global best	[-]
$x_n^{P_{best}}$	Guide position for each particle	[-]
$x_{n,upper}$	Upper side constraints of decision variables	[-]
$y\ (x)$	Objective function vector for each set of positions	[-]
y_{best}	Set of objective function values for a particle belonging to G_{best}	[-]
y_i	Set of all the objective function values produced by a particle during the PSO optimization	[-]

Greek Letters

α	Level of confidence	[-]
$(-\Delta H_{ads})$	Isosteric heat of adsorption	[J mol^{-1}]
ΔH_V	Vaporization enthalpy	[J mol^{-1}]
$(-\Delta H_o)$	Heat of adsorption	[J mol^{-1}]
$(-\Delta H_I)$	Heat of adsorption	[J mol^{-1}]
$(-\Delta H_L)$	Heat of adsorption	[J mol^{-1}]
Δq	Difference between q_{min} and q_{max}	[mol kg^{-1}]

Indexes

A, B	Cages of MIL-100 (Fe)
i	Particle
k	Iteration
n	Decision variable

List of Acronyms

AIPO	Aluminophosphate
CI	Confidence intervals
CSPSO	Constrained Sliding Particle Swarm Optimization
DISL	Dual Ising-Single Langmuir
FOR	Feasible Operating Region

GA	Genetic Algorithms
LHS_MDU	Latin Hypercube Sampling with Multi-Dimensional Uniformity
MOF	Metal-organic Framework
MOFEPSO	Multi-Objective Feasibility Enhanced Particle Swarm Optimization
MPV	Most probable value
OF	Objective function
PSO	Particle Swarm Optimization
RAM	Random Access Memory
SAPO	Silico-aluminophosphate
SPSO	Sliding Particle Swarm Optimization

1 Introduction

1.1 Framing and presentation of the work

Energy demand is continuously increasing, along with demographic growth. The energy consumption for domestic uses is about one-third of the global value [1,2]. Most of that energy is spent on heating spaces or water for various ends [2].

Usually, heating relies on electricity mainly generated through the burn of fossil fuels (ca. 40%)[3,4]. Due to environmental concerns, alternatives for the traditional heat production mechanism (such as vapor compression systems or conventional heat pumps) are being searched.

A possible alternative is the adsorption-based heat pumps. The operation of these heat pumps is based on thermal energy, reducing the electric power dependency. Furthermore, the heat can be produced based on renewable sources of heat (solar power), waste heat from industrial applications, or natural gas combustion as the least sustainable alternative. In addition, the adsorbent-adsorbate working pairs used in these pumps tend to be more sustainable than the working fluids employed in the vapor compression systems [4,5].

The main core of these heat pumps is the adsorbent heat exchanger. Many studies have been published comparing different coatings, configurations, and, most importantly, different adsorbent-adsorbate working pairs to choose the best design.

In the literature, the screening of working pairs is usually done by resorting to relatively simple models. However, the evaluation is done based on fixed values of temperatures or keeping only one temperature variable [6,7]. In this way, other operation points within the feasible temperature range are not being considered. Furthermore, other possible solutions where different materials could have similar performances are not computed.

Therefore, this dissertation aims to propose an optimization strategy for heat pumps that considers the temperatures involved in the process and the type of adsorbent material as decision variables. Two optimization approaches, single-objective and multi-objective, are proposed to study the numerical problem related to this optimization and address the most suitable approach. The optimization is proposed to be done using a meta-heuristic population-based method, Particle Swarm Optimization. Hence, the population provided by the optimization algorithm can be used to access the Feasible Operating Regions of the heat pumps.

1.2 Contribution of the author to the work

My contributions to this dissertation were the research of possible materials to compare during the study, adsorption and heat capacity data for the chosen materials, the comparison of those datasets, and the fitting of the referred isotherms to the chosen isotherm model. The heat of adsorption was also calculated and fitted through a polynomial regression. The isotherms of five Metal-organic Frameworks used in this work had been previously measured and fitted by Márcia Silva during her Ph.D. thesis[8].

For the simulation and optimization part, I wrote the code for the simulation of the heat pumps with the thermodynamic model. Then, I adapted an in-house-made PSO algorithm to the model and obtained and analyzed the results.

1.3 Organization of the dissertation

Chapter 2 introduces a brief revision of the state-of-the-art and the basic knowledge required to understand the remaining work, starting with a historical introduction (section 2.1), followed by a comparison between the adsorption-based heat pumps and the traditional mechanical heat pumps (section 2.2). Then the core of adsorption heat pumps theory is described with the operation basis (section 2.3), the possible models for simulation (section 2.4), and a revision of the literature on simulation and screening of working materials (section 2.5). At last, a state of the art for optimization procedures is also presented (section 2.6).

In Chapter 3, the model implemented for the simulation is presented, as well as the different materials considered during the study. The optimization problem is also described, with the design of the objective functions, specification of the decision variables, and the respective side constraints. Furthermore, the Particle Swarm Optimization is depicted together with the uncertainty calculation and the method for identifying feasible regions.

Chapter 4 shows the results obtained during both single and multi-objective optimizations, as well as the comparison of the results obtained with each strategy.

The main conclusions of this dissertation are presented in Chapter 5, followed by Chapter 6 where the assessment of the work developed is performed.

In Appendix A, the data related to the adsorbent material is presented.

In Appendix B, the figures for evaluating particle distribution during the PSO algorithm are displayed.

In Appendix C are pictured the lines of thought for mapping the temperatures and materials that lead to a certain performance of the adsorption heat pump when there is no overlapping in the temperature values for each region.

2 Context and state of the art

2.1 Historical context

Heat pumps development began with the need for refrigeration technologies[9]. While Mankind had the means to produce heat through multiple techniques since early ages, the cooling required for better food conservation, ice production, and house temperature regulation only had significant developments in the 19th century [10].

The scientific approach to this problem was initiated by Carnot when he established a relationship between work and heat transformations. His ideas were developed and reformulated by other scientists such as Clausius, Kelvin, and Mollier[11].

Peter von Ritting is responsible for the first industrial application of heat pumps in 1857 by employing vapor compression in a closed circuit working in batches for salt production from concentrated brine. The heat produced by the compression was used to evaporate the water from brine, replacing the heat previously provided by burning wood [9].

In the 40s, heat pumps became more popular in house heating applications due to the coal shortage provoked by the Second World War. With the war's end, the oil price decreased, reducing the interest in the heating pump technology[9]. This interest was renewed during the oil crisis in 1973 when the International Energy Agency recognized heat pumps as a cornerstone to reducing the energetic dependence on fossil fuels. Since then, the interest in such technologies has been growing, leading to increased efficiency and reliability of heat pumps [11].

2.2 Types of heat pumps

Various types of base concepts have been explored during the development of heat pumps[12].

The most common type is the mechanical heat pumps, considered the traditional heat pumps. This kind of heat pump resorts to mechanical power in the form of work energy to retrieve heat from a cold source and transfer it to a hot source. The mechanic power is obtained by compressing and decompressing the working fluid in a closed-cycle operation [12,13].

Another type of heat pumps is the thermally driven heat pumps, whose operation is based on the use of heat energy to perform the heat transfer instead of mechanical power, as mentioned previously. There are multiple subsections in this category. The adsorption-based heat pumps are the most relevant for the work in question. These pumps fulfill the compression and decompression of the working fluid through adsorption processes, where the adsorbent is typically solid and fixed [13–15].

The mechanical heat pumps were the most frequently used during the 20th century due to the low number of components, ease of access to electricity in industrialized cities, and the high performance provided by the synthetic refrigerants employed[13].

As environmental concerns increased, those refrigerants started to raise uneasiness due to their ozone depletion effect and global warming potential[15–17]. Thus, sustainable alternatives to the use of these refrigerants were in order.

While some research paths diverted to developing new and more sustainable refrigerants to be the working fluids in the traditional heat pumps[17–19], others proceeded to improve heat pumps based on different working principles, such as the adsorption-based heat pumps[15,16].

Since the aforementioned heat pumps can operate with natural working fluids, the environmental concerns are reduced. Besides that, the heating source required is one of low temperature, so their operation is compatible with the use of solar energy, geothermal energy, or other residual heat sources. In addition, the lack of moving parts lowers the operation noise can be seen as an advantage in domestic applications [1,4,15]. At last, adsorption heat pumps have also been studied and aligned with water harvesting [20].

However, they present some disadvantages, such as the propensity to present worse performance indicators compared to mechanical heat pumps since the operating temperatures are also lower. Moreover, if the heat source relies on burning fossil fuels, it would result in CO_2 emissions. Furthermore, the heat production is not continuous, although this might depend on the heat pump design[1,4,15].

2.3 Operating basis

The simplest design for an adsorption heat pump consists of four main components: an adsorption heat exchanger, an evaporator, a condenser, and valves (including an expansion valve)[4].

The working steps of adsorption heat pumps are well described in the literature[1,4,13–15].

a) Isosteric heating: the adsorbent bed is isolated and heated to increase the pressure from P_{evap} to P_{cond} (the pressure value in evaporator and condenser, respectively). When the desired pressure is obtained, the valve that connects the adsorbent heat exchanger to the condenser is opened. The adsorbed amount is considered constant during this stage.
b) Isobaric desorption: heat is provided to the system to promote the adsorbent regeneration by increasing the temperature and heating the adsorbent bed. The desorbed adsorbate flows to the condenser, where it releases latent heat through the phase shifting at constant pressure.

c) Isosteric cooling: in similarity with isosteric heating, the adsorption heat exchanger is isolated and cooled to reduce the pressure back to P_{evap} value, releasing sensible heat.

d) Isobaric adsorption: the valve between the evaporator and the adsorption heat exchanger is opened. The working fluid in the evaporator receives heat from the environment, shifting into the vapor phase and later being adsorbed in the fixed bed. The heat produced during the adsorption process is then retrieved from the system. This step lasts until the equilibrium uptake is reached or when the difference in temperature between the adsorbent bed and the fluid is no longer significant.

The condenser and evaporator operating conditions are related to the liquid-vapor equilibrium and the temperature of the heating fluids used in the process.

The working steps are pictured in Figure 1.

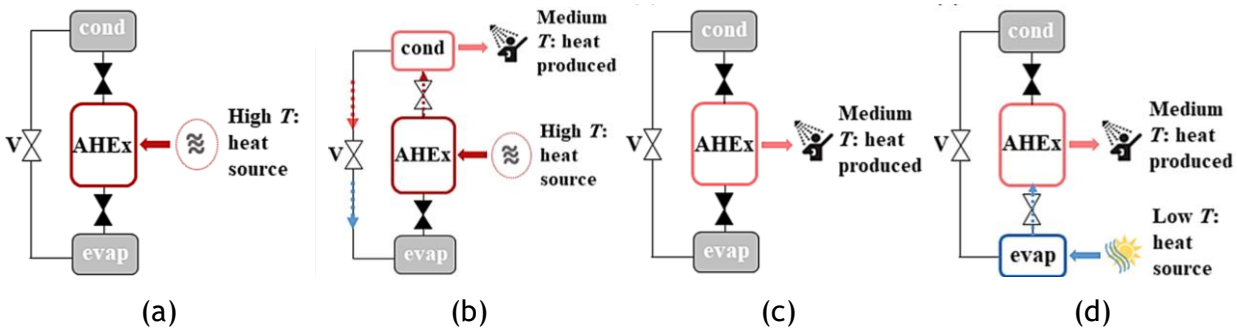

Figure 1. Working steps of the adsorption heat pumps (isosteric heating (a), isobaric desorption (b), isosteric cooling (c) and isobaric adsorption (d)) (adapted from Pinheiro et al. [4]).

Another important component of adsorption heat pumps is the adsorbent-adsorbate working pair. Several combinations are reported in the literature.

Amongst the adsorbents, the more commonly used are silica gel, zeolites, activated carbon, aluminophosphates (AlPOs) and silico-aluminophosphates (SAPOs), composite materials, and Metal-organic Frameworks (MOFs) [1,4,5,13,15,21,22].

Silica gel presents the capacity to be regenerated at low temperatures, which poses an advantage for these processes alongside their low cost and reliability. Although some reports mention the loss of some adsorption capacity above 473 K, others refer that such phenomenon is common among the adsorbents, so it must not be seen as a disadvantage. However, the adsorption process occurs at higher relative pressures, limiting the use of this adsorbent [5,13,22].

Zeolites allow for more freedom when it comes to operating temperature ranges. However, since they have a high affinity to water, they require a higher desorption temperature [5,13,22].

Activated carbons' performance varies with the adsorbate chosen, so one cannot directly compare it with other adsorbents [5,13,22].

AlPOs and SAPOs are modified materials similar to zeolites with a high water adsorption capacity while presenting lower desorption temperatures when compared to zeolites [5].

Composite materials originate from the insertion of inorganic salts in porous matrixes. The base compounds used in their formation are directly linked with the characteristics of the final material obtained. In some cases, this type of adsorbent presents a high adsorption capacity with lower desorption temperatures [5,13,22].

MOFs present high adsorption capacities within mild operating conditions. Some of these materials present low stability when exposed to water. Others might suffer degradation, but studies about their stability and new combinations can result in more stable materials without compromising the adsorption phenomena. Another concern related to using such materials in adsorption heat pumps is that MOFs are considered quite expensive materials. However, their price has decreased due to increasing interest, so this might no longer be a problem in the near future [1,5,13].

The adsorbents presented above often combine with adsorbates such as water, ammonia, ethanol, and methanol [1,13].

Water is the most used adsorbate since it is a natural compound with no toxicity and no major risks associated. It presents a high heat of vaporization, but the range of temperatures for operation is limited because of the triple point (at 0.0061 bar) and fusion point (at 1.01 bar) near 273 K [13].

Ammonia presents a high heat of vaporization and has the advantage of allowing a broader range of temperatures since its fusion temperature is about 240 K at 1.01 bar, making the heat pumps that use ammonia as adsorbate suited for a larger number of applications. However, this working fluid has a higher level of toxicity and is flammable [13].

Ethanol is not so frequently used because its vaporization heat is lower than the last two compounds, meaning that the adsorbed amount needs to be higher to obtain similar heating device performance. Due to the lower fusion temperature, its refrigeration capacity is higher than ammonia. This compound is also flammable [13].

Methanol is studied as a possible adsorbate since its heat of vaporization is higher than ethanol. However, it suffers thermal decomposition at temperatures higher than 383-423 K and surpasses ethanol toxicity while presenting the same flammability levels [13].

Water is frequently combined with silica gel, zeolites, AlPOs and SAPOs, composite materials, and MOFs. Ammonia is paired up with activated carbons and composite materials. Ethanol and

methanol share the same list of adsorbents: activated carbon, composite materials, and MOFs. [13]

In an attempt to improve the performance of adsorption-based heat pumps, several modifications in their design have been idealized in the fields of heat exchangers geometry[4,5,13], adsorbent morphology [4,5,13,23], and heat and mass integration for multiple bed heat pumps[13].

As it is possible to see from the above description, several potential adsorbents and adsorbates can be employed within an adsorption heat pump. The systematic evaluation of their performance concomitantly with the assessment of the optimal process performance is a complex task. Hence, the need for a strategy that allows a reliable optimization of the system while considering the possible materials used within the unit.

2.4 Heat pumps modeling

Three types of models are described in the literature: the thermodynamic models, the lumped parameters models, and the distributed parameters models[13,24].

The thermodynamic ones are the simpler models since they disregard the kinetics of heat and mass transfer inside the adsorbent bed, accounting only for the thermodynamic equilibrium between adsorbate and adsorbent associated with their isotherm. These models allow an optimistic system performance prediction with low computational effort [24].

The lumped parameters models consider the resistances to heat and mass transfer between the neighborhood of the system and the adsorbent bed while ignoring the resistances to those transfers in the adsorbent bed. In other words, the evolution of the system is only dependent on time and is uniform for every position of the bed. The accuracy of this type of models is reported to be of a good level with a medium level of computation requirements. Still, it ultimately depends on the geometry of the heat exchanger considered in the model [13,24].

The most complete models are the distributed parameters models. They account for both internal and external heat and mass transfer resistances, shifts in vapor pressure due to pressure drop, and temperature differences between the adsorbent and adsorbate, although sometimes some simplifications in terms of temperature and pressure are considered. In these models, the system evolution depends on time and space within the adsorbent heat exchanger, so the results are largely affected by the geometry chosen, as the temperature and mass profiles might change in a unidimensional, bidimensional, or tridimensional way [13,24].

2.5 Heat pumps adsorbent material screening and optimization

As seen in the previous section, there are three types of models, and each one of these is usually employed for a specific purpose. For process simulation and optimization purposes, the

more complex models, namely the lumped and distributed parameters, are the preferred ones[25,26].

For comparing the performance of the different materials, the use of thermodynamic models becomes more frequent.

For instance, Boman et al. [7] combined thermodynamic models with the addition of a heat transfer model based on the Fourier-Bessel series for an annular tube with constant temperature on the inside and adiabatic heat transfer to the outer radius. The Engineering Equation Solver was employed in the referred study to fulfill a parametric analysis. The analysis aimed to determine the desorption temperature that results in the best performance coefficient for each pair of adsorbent-adsorbate.

The work of Liu et al.[6] is an example of using a pure thermodynamic model to select the top materials for cooling and heating applications, employing water as a working fluid. The adsorbent properties were also connected with their performance in both modes of heat pumping.

In this scenario, the usual approach used in the literature for material screening in heat pumps presents limitations. For starters, some approximations for the required parameters are used in the screening process, which may lead to the equivocated evaluation of materials. In addition, as aforementioned, it is frequent to see fixed temperature limits for each step of the process or the variation of one of those temperatures. Therefore, operating conditions where the performance might be similar will be disregarded. This has particular importance for industrial processes, where conditions might vary and affect the system's performance. Hence, justifying the pertinence of this work.

2.6 Systems optimization

A way to expand the range of temperatures in the study and avoid overlooking solutions that will lead to similar performances is to introduce material screening in the context of the process optimization.

As reviewed by Venter[27], optimization procedures can be divided into two categories: local techniques and global ones.

Local techniques are typically based on gradients and tend to be more efficient since fewer objective function evaluations are required to find the optimum. In addition to this fact, multiple design parameters can be used. However, these methods do not distinguish between global and local optima. Other disadvantages are the poor behavior when facing discrete variables and the complexity required for applying such methods. An example of this type of technique is Newton's method [27].

Global methodologies have the advantage of allowing local and global optima localization. This set of methods can be divided into two subsections: the evolutionary models and the deterministic ones [27].

In the first subsection, there is no need to calculate gradient information. The multiple points used allow for multiple starting conditions. These starting conditions can be random or predetermined using the Design of Experiments. The evolutionary methods are more consistent, providing a broader possibility of finding the global optimum and adaptability to discrete variables. On the downside, they demand more computational effort, limiting the size of the problems that can be solved through this type of methodologies. Another disadvantage is the required tunning of the parameters (such as the size of the initial set of points) before the optimization procedure. The most typical models of this kind are the Genetic Algorithm (GA) and the Particle Swarm Optimization (PSO) [27].

Another type of division between the optimization methods established by Cavazzuti [28] is between stochastic and deterministic methods. The deterministic methods are related to the deterministic and gradient-based methodologies, with no randomness associated. They are more frequently employed in single-objective optimization. The stochastic ones englobe the evolutionary methods, usually possessing some degree of randomness, and can be used in both single and multi-objective optimizations.

Multi-objective optimizations can be treated as a single-objective problem where the objective function is a weighted sum of each individual objective. Yet, this poses the need to introduce more variables (the weight of each objective function) and cannot describe the entire problem. Nowadays, the most common approach is the construction of a Pareto Front, which allows the evaluation of the trade-off between the objective functions and provides a better general picture of the system [29].

Optimization in chemical engineering processes is quite usual[29], whether in food industries[30], energetic consumption optimization[31], or even cyclic processes optimization[32].

In fact, evolutionary methods of optimization have been used in heat pumping. Lee et al. [33] used the PSO algorithm to optimize the energy recovery in an indoor pool using discrete and continuous parameters. In the work of Rahman et al. [34], the specific cooling power was also maximized based on the optimal cycle time using PSO. During the multi-objective optimization carried out by Li et al.[35], the energetic, environmental, and economic impacts of a solar hybrid heat pump heating and cooling system were optimized by resorting to the GA method.

However, it was not found any report of the employment of the adsorbent material as one of the variables in the optimization of adsorption heat pumps. Even when different materials are

considered, the overall tendency in cyclic processes is to treat each material individually and then compare the optimal points for each adsorbent [36].

Nevertheless, the use of the adsorbents as a discrete variable is starting to grow in this type of process.

In the recent work of Nogueira et al.[37], the adsorbent material is treated as a discrete decision variable during a PSA process optimization using a modified version of the PSO algorithm. This modified version was named Constrained Sliding Particle Swarm Optimization (CSPSO) and allowed for a compartmentalized search within the constraints and the defined variable limits [38]. Furthermore, a Feasible Operating Region (FOR) is built based on the Fisher-Snedecor test. This step allows the widening of the operating conditions to contemplate combinations of parameters that will result in a close-to-optimal performance. The authors of this work concluded that different materials could be employed in different conditions with similar performance, despite their metric's criteria.

Building a feasible operating region is, thereby, a valuable tool in chemical engineering. The insurance that the productivity of a process will remain very close to the maximum for a certain range of values of the variables can help in the design of the process or even in process control operations.

This tool was introduced by Nogueira et al.[39] in Sliding Particle Swarm Optimization (SPSO) method. It was later extended to constrained problems by Rebello et al.[38] in CSPSO for single-objective optimization, afterward expanded to a multi-objective optimization problem in Rebello et al.[40]. In the lattermost, the optimal points in the feasible region are grouped in clusters. Typically, the clusters divide the data into three regions: two where one of the objectives prevails and one region where there is a compromise between the two goals. The decision variables can also be represented in this cluster system, as demonstrated in the work of Rebello et. al [41].

Considering these facts, there is room for improvements in the material screening in adsorption heat pumps. The present work proposes employing the material as a discrete variable with an optimization methodology, evaluating the different materials in an ampler range of temperatures, attached with constructing a feasible region to evaluate variables that may lead to similar performances.

3 Materials and methods

3.1 Adsorption heat pump model

For the simulation of the adsorption heat pumps behavior, a pure thermodynamic model was considered [5-7,13-15]. Figure 2 is a schematic representation of these models temperature limits and heat exchanges.

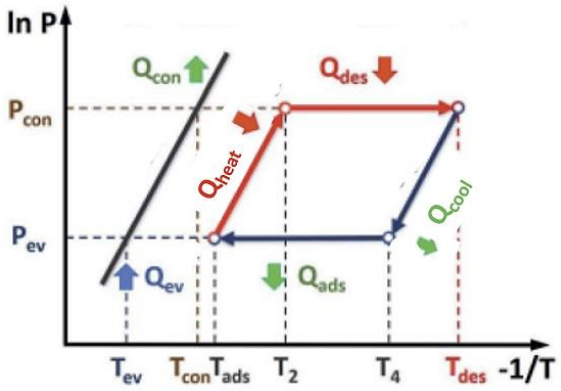

Figure 2. Diagram of ln(P) vs -1/T of an adsorption heat pump's cycle operation (adapted from Liu et al.[6]).

In this model, the heat transferred in isosteric heating (Q_{heat}), isobaric desorption (Q_{des}), isosteric cooling (Q_{cool}), and isobaric adsorption (Q_{ads}), as well as in condensation (Q_{cond}) and evaporation (Q_{evap}) were calculated by Equations 1-6, respectively:

$$Q_{heat} = \int_{T_{ads}}^{T_2} m_{ads}\left(c_{p,ads}(T) + q_{max}\, c_{p,water}(T)\right) dT \tag{1}$$

$$Q_{des} = \int_{T_2}^{T_{des}} m_{ads}\left(c_{p,ads}(T) + q(T)\, c_{p,water}(T)\right) dT + \int_{q_{max}}^{q_{min}} m_{ads}\,(-\Delta H_{ads})(q)\, dq \tag{2}$$

$$Q_{cool} = \int_{T_{des}}^{T_4} m_{ads}\left(c_{p,ads}(T) + q_{min} c_{p,water}(T)\right) dT \tag{3}$$

$$Q_{ads} = \int_{T_4}^{T_{ads}} m_{ads}\left(c_{p,ads}(T) + q(T)\, c_{p,water}(T)\right) dT + \int_{q_{min}}^{q_{max}} m_{ads}\,(-\Delta H_{ads})(q)\, dq \tag{4}$$

$$Q_{evap} = m_{ads}\, \Delta q\, \Delta H_v + \int_{T_{cond}}^{T_{evap}} m_{ads}\, \Delta q\, c_{p,water}(T)\, dT \tag{5}$$

$$Q_{cond} = m_{ads}\, \Delta q\, \Delta H_v \tag{6}$$

Where m_{ads} it the mass of adsorbent, $c_{p,ads}$ is the specific heat capacity of the adsorbent, q_{max} and q_{min} are the maximum and minimum adsorbed quantities during the cyclic operation, with

$\Delta q = q_{max} - q_{min}$, $c_{p,water}$ is the water specific heating capacity, $(-\Delta H_{ads})$ is the isosteric heat of adsorption, and ΔH_v is the vaporization enthalpy of water.

Unlike some thermodynamic models presented in the literature[5,13–15], the mass of inerts (the mass of metal tubes in the adsorbent heat exchanger, for example) was disregarded since this simulation process is not based on experimental data and, therefore, there would be no valid foundation in the value attributed to the said parameter.

Furthermore, every term of Equations 1-6 depends on the adsorbent mass. So, a value of 1 kg was assumed because changing it would be equivalent to a simple multiplication of the obtained value by the mass of the absorbent.

Regarding the temperatures of the system, T_{ads} was considered equal to T_{cond} [4]. Besides that, the intermediate temperatures (T_2 and T_4) can be calculated based on the remaining temperatures with Equations 7 and 8 [6,42,43].

$$T_2 = \frac{T_{cond}^2}{T_{evap}} \tag{7}$$

$$T_4 = \frac{T_{evap}\ T_{des}}{T_{cond}} \tag{8}$$

The value of water's heat capacity in J mol^{-1} K^{-1} was assumed to depend on the system temperature according to Equation 9 [44].

$$c_{p,water}(t) = \left(A + B\,t + C\,t^2 + D\,t^3 + \frac{E}{t^2}\right) \tag{9}$$

With $t = \frac{T}{1000}$, $A = -203.6060, B = 1523.290, C = -3196.413, D = 2474.455,$ and $E = 3.855326$ in the corresponding units.

The heat of vaporization of water in J mol^{-1} is calculated by Equation 10 [6].

$$\Delta H_v = (2502 - 2.51\,(T - 273)) \times 18.02 \tag{10}$$

The limits for the adsorbed water amount are determined by $q_{max} = q\,(T_{ads}, P_{evap})$ and $q_{min} = q\,(T_{des}, P_{cond})$. The values of P_{cond} and P_{evap} are calculated through the Antoine Equation (Equation 11) with the values of T_{cond} and T_{evap} [45].

$$P = 10^{A - \frac{B}{C+T}} \tag{11}$$

With $A = 4.6543,\ B = 1435.264$, and $C = -64.848$ in the corresponding units for temperatures and between 255.9 K and 375 K.

The parameters $c_{p,ads}$, q and ΔH_{ads} depend on the adsorbent material. For this work, the adsorbents used were MIL-160 (Al), MIL-100 (Fe), MIL-125_NH_2 (Ti), CAU-10, Al-FUM, Zeolite 3A, Zeolite 4A, Zeolite 5A, Zeolite 13X, and AQSOA FAM-Z02 (SAPO-34).

The first 5 materials belong to the MOF's family. They have been studied previously in the LSRE-LCM research group for water harvesting by adsorption in (P)TSA units[8,46–48]. The remaining have been identified in the literature as common adsorbents for water adsorption units[4].

While the isotherms for the MOFs have been measured and adjusted in other works developed in LSRE-LCM, the other isotherms were adjusted based on the experimental data collected from scientific articles, either from a direct collection of the values of the adsorbed quantities or the graphic reading using the ScanIt software.

The data was collected from different sources and compared to choose the most consensual dataset with the larger amplitude in terms of temperature and pressure. That dataset was then adjusted to the Ising-Langmuir isotherm equation, presented in Equation 10 [8].

$$q = q_{sat\,I}\frac{K_o\,P}{(K_o\,P + w_I^2)} + q_{sat\,L}\frac{K_L\,P}{(1 + K_L\,P)} \tag{10}$$

With

$$w_I = \frac{1}{2}\left(1 - K_I\,P + \sqrt{(1 - K_I\,P)^2 + 4K_o\,P}\right) \tag{11}$$

$$K_I = K_{\infty,I}e^{\left(\frac{-\Delta H_I}{RT}\right)} \tag{12}$$

$$K_o = K_{\infty,o}e^{\left(\frac{-\Delta H_o}{RT}\right)} \tag{13}$$

$$K_L = K_{\infty,L}e^{\left(\frac{-\Delta H_L}{RT}\right)} \tag{14}$$

Where q is the total adsorbed amount, $q_{sat\,I}$ is the specific saturation adsorption capacity in Ising isotherm, $q_{sat\,L}$ is the specific saturation adsorption capacity in Langmuir isotherm, and $K_{\infty,I}$, $K_{\infty,o}$ and $K_{\infty,L}$ are the equilibrium constants of Ising-Langmuir isotherm, R is the ideal gas constant and the temperature dependence is given by the van't Hoff law.

The parameters for the isotherm equation were calculated using the solver from Excel to minimize the absolute error between the estimated adsorbed amount and the corresponding value from the dataset for a specific pressure value.

For the water adsorption isotherm in MIL-100 (Fe), the model used was the Dual-Ising Single-Langmuir (DISL) model, presented in Equation 15 [8].

$$q = \sum_{i=A,B}\left(q_{sat\,I}\frac{K_{o,i}\,P}{(K_{o,i}\,P + w_{I,i}^2)}\right) + q_{sat\,L}\frac{K_L\,P}{(1 + K_L\,P)} \tag{15}$$

Where A and B represent each one of the MIL-100 (Fe) cages, and the parameters are calculated by Equations 11-14.

With the adjusted equations for the isotherms, the isosteric heat of adsorption ($-\Delta H_{ads}$) was then calculated through the Clausius-Clapeyron equation (Equation 16).

$$(-\Delta H_{ads}) = RT^2 \left(\frac{\delta \ln P}{\delta T}\right)\Big|_{q=const} \tag{16}$$

Considering that ($-\Delta H_{ads}$) is independent of the temperature, then its value can be obtained through a linear adjustment for each q, according to Equation 17.

$$\ln P = -\frac{(-\Delta H_{ads})}{R}\frac{1}{T} + G \tag{17}$$

Where G is the integration constant.

According to the values obtained for each adsorbed amount, the isosteric heat was adjusted to one or more branches of polynomial equations of nth order.

More information on the adsorbents used can be found in Appendix A.

The integration of Equations 1-6 was solved by resorting to Simpson's 3/8 rule.

3.2 Optimization problem

3.2.1 Optimization goals

The Coefficient of Performance (COP) was used to evaluate the performance of the adsorbent-water working pair. The heating mode of operation was the focus of this work since it is the predominant cause of energy consumption.[2,3] For the heating mode, this coefficient is defined as the amount of heat released from the system divided by the amount of heat provided to the system, as presented in Equation 18[4].

$$COP_{heat} = \frac{Q_{cond} + Q_{ads} + Q_{cool}}{Q_{des} + Q_{heat}} \tag{18}$$

The higher the COP_{heat} value is, the more efficient the adsorption heat pump will be since more heat will be produced by unit of heat provided to the system. Therefore, the first objective of the optimization problem will be to maximize this function.

From the possible sources of heat, natural gas is the most common and available, with the downside of releasing carbon dioxide upon burning. Despite that disadvantage, it was considered the heat source during the simulations, to represent a trade-off between energy consumption and productivity.

Therefore, a second objective function was considered to minimize natural gas consumption. The said function relies on the cost of natural gas consumed during a cycle of operation.

Because no dynamic interactions were considered in the model, the calculations were based on the heat required by the operation, as presented in Equation 19.

$$Cost = Cost_{GN}(Q_{des} + Q_{heat})(1 + LF) \quad (19)$$

The cost of natural gas, $Cost_{GN}$, was considered as 20.53 € GJ^{-1}, the highest price practiced during the second semester of 2021 in Portugal (corresponding to the price of the lowest consumption band for domestic use)[49]. The Loss Factor, LF, corresponded to the loss of heat during the process and was admitted as 0.1.

The cost presented a reduced value when compared to the COP_{heat} value. To ensure that both objective functions were treated with similar ponderation during the optimization problem, the cost function was multiplied by an Impact Factor, $IF = 20$. This factor guarantees that both objective functions are in a similar order of magnitude. The adapted objective function is presented in Equation 20.

$$Cost_{IF} = IF \times Cost \quad (20)$$

It was performed a single optimization of COP_{heat}, as well as a single-objective approximation of the simultaneous optimization of COP_{heat} and $Cost_{IF}$, followed by a multi-objective optimization of both functions. This last objective function was not evaluated individually since it was predictable that the minimum value of the cost would result in the non-operability of the adsorption heat pump.

It is important to mention that since no dynamic behavior was evaluated, both functions will be evaluated per cycle of operation, which may vary from material to material.

3.2.2 Design of the objective function

The decision variables play an essential role in designing an objective function (OF). As the goal of this work is the simultaneous optimization of the process operating variables and material used, the decision variables chosen were T_{evap}, T_{cond}, T_{des}, and the adsorbent material.

A second step in the OF design is the definition of the constraints. For the temperatures, the side constraints were based on a review article that summarized the most commonly used temperatures for each type of adsorbent-adsorbate working pair [4].

The material is an integer variable introduced in the optimization problem. The continuous/discrete nature of this problem was solved by an approximation. A continuous variable was attributed to the material ranging from 0.51 to 10.49. Then it was internally converted to an integer number by rounding it, guaranteeing its discrete behavior. The material order was randomized, as presented in Table 1.

Table 1. Discrete variable values attributed to each material.

Adsorbent	Material value
Zeolite 5A	1
Zeolite 3A	2
MIL-100 (Fe)	3
Al-FUM	4
AQSOA FAM-Z02 (SAPO-34)	5
MIL-160 (Al)	6
Zeolite 4A	7
MIL-125_NH_2 (Ti)	8
Zeolite 13X	9
CAU-10	10

The side constraints of each decision variable are presented in Table 2.

Table 2. Side constraints of the decision variables.

Variable	Lower bound	Upper bound
T_{evap} /K	280	303
T_{cond} /K	309	365
T_{des} /K	345	473
Adsorbent material	0.51	10.49

However, not all the combinations contemplated by these ranges lead to a feasible solution. To avoid the consideration of such points, constraints were defined. In the optimization strategy, the constraints were assured by penalties. The penalization was marked by attributing the constant value of 100 to the objective function(s) when the decision variables did not respect the constraints.

At last, the optimization problem can be summarized as:

Single-optimization:

$$\text{Case 1: OF} = \max_{T_{evap}, T_{cond}, T_{des}, Material} COP_{heat}$$

$$\text{or Case 2: OF} = \min_{T_{evap}, T_{cond}, T_{des}, Material} (Cost_{IF} - COP_{heat} \times EF)$$

with EF being the equalization factor for the objective functions to present the same units. In this case, EF acquires the value of 1 €.

Multi-optimization:

$$\text{Case 3: OF} = \begin{cases} \min\limits_{T_{evap}, T_{cond}, T_{des}, Material} & Cost_{IF} \\ \max\limits_{T_{evap}, T_{cond}, T_{des}, Material} & COP_{heat} \end{cases}$$

Subject to:

$$q_{min} < q_{max}$$

$$T_{cond} + 5 < T_{des}$$

$$T_4 \; and \; T_2 < T_{des}$$

$$T_4 \; and \; T_2 > T_{cond}$$

3.3 PSO optimization

The previously presented optimization problem was solved using a Particle Swarm Optimization algorithm. The PSO is a meta-heuristic technique from the Artificial Intelligence field. It can be pictured as a group of individuals (particles) searching randomly in a certain space for the optimum solution to a proposed goal. Each particle evaluates its current position based on the value of the objective function and determines its next step by analyzing its own history of those values as well as the history of the values for other particles. Iteration after iteration, the particles will get closer to the desired point of the objective function. This process is accelerated through the combined information collected by different particles, allowing a faster exploration of the problem's landscape [50,51].

The algorithm used was based on the Multi-objective Feasibility Enhanced Particle Swarm Optimization (MOFEPSO) developed by Hasanoglu et al.[52] and the CSPSO developed by Rebello et al.[38,40], although the restrictions were not applied as external conditions.

Before the implementation of the PSO, the number of particles ($\mathrm{N_{part\_max}}$), number of iterations ($\mathrm{N_{it\_max}}$), the number of decision variables ($\mathrm{N_{DV}}$), and respective decision variables side constraints ($x_{n,lower}$ and $x_{n,upper}$) should be defined in the system.

The Initialization step is the first stage of this optimization strategy, where the positions (x) of the particles are randomly initialized through the Latin Hypercube Sampling with Multi-dimensional Uniformity (LHS_MDU) to ensure a good distribution of the initial particles in the problem field.[53] The velocity (v) for each particle (i) for each decision variable (n) is initialized with Equation 21. The initialization procedure is pictured in Figure 3.

$$v_{i,n} = a^v(2r-1)(x_{n,lower} - x_{n,upper}) \quad (21)$$

In this equation, $a^v = 0.3$ and corresponds to the initialization factor of velocity, and r is a random number between 0 and 1.

The values of the position and velocity of the particles are stored on the matrix X and V of dimensions $[N_{DV}, N_{part\_max}]$. The matrixes P_{best} and G_{best} are also created to save the best positions and the correspondent values of the objective function(s) ($y(x) = OF(x)$) of each particle and the global swarm, respectively. The actualization of these matrixes is performed by the assessment of the dominance, where the values calculated in each step of the algorithm are compared to the points stored in P_{best} and G_{best}. The best values are saved in the matrix (both x and $y(x)$) and the values that are no longer "dominant" are eliminated from that dataset.

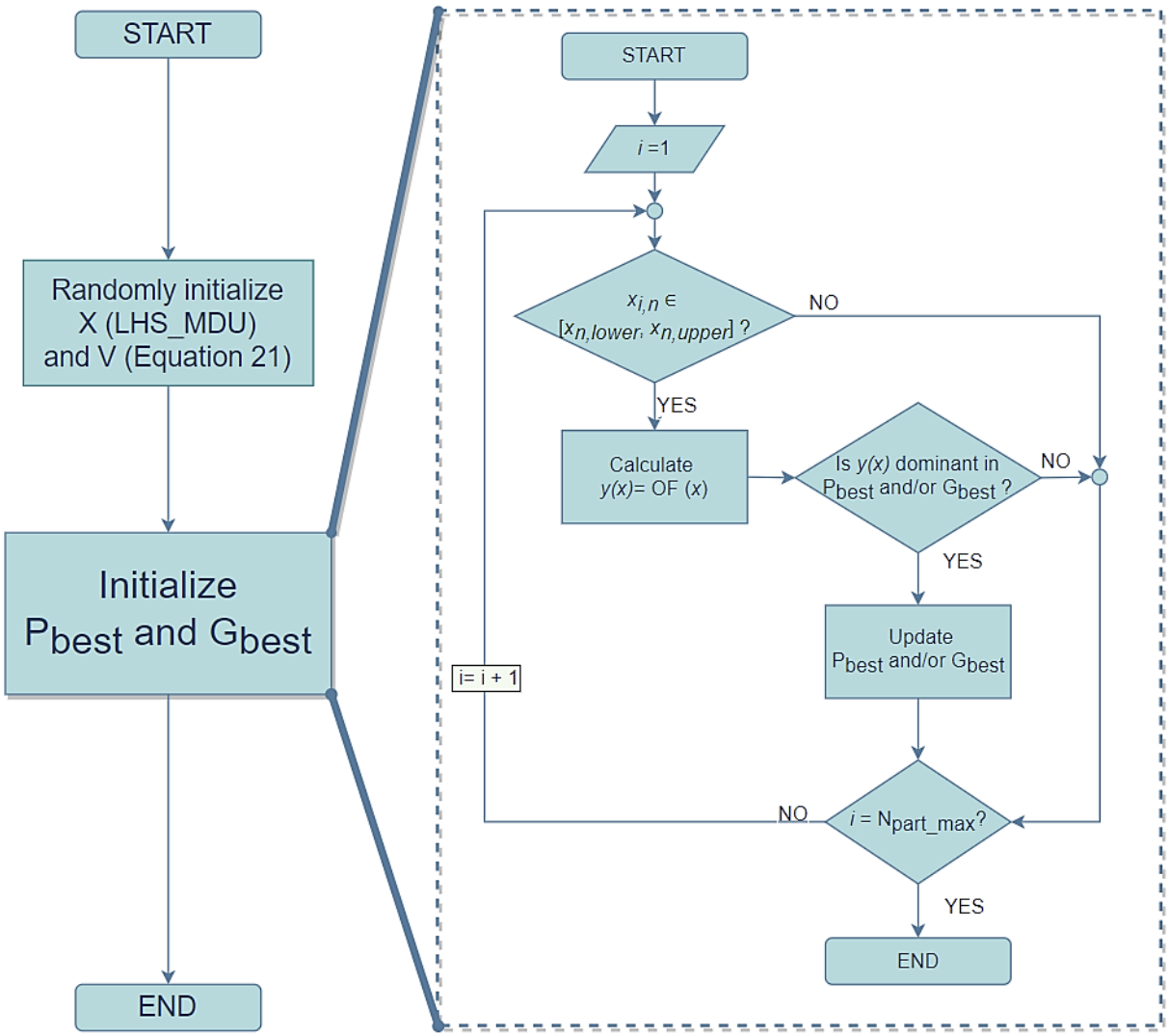

Figure 3. Initialization algorithm.

After the Initialization Algorithm, the optimization step begins. A new velocity ($v_{i,n,k}$) is calculated for each particle by Equation 22 where a position from G_{best} and another from P_{best} are randomly chosen to be the guide positions ($x_n^{G_{best}}$ and $x_n^{P_{best}}$), r_1 and r_2 are two random numbers between 0 and 1, C_o, C_1 and C_2 are acceleration coefficients, and k is the current iteration.

$$v_{i,n,k} = C_o v_{i,n,k-1} + C_1 r_1 \left(x_n^{G_{best}} - x_{i,n,k-1}\right) + C_2 r_2 (x_n^{P_{best}} - x_{i,n,k-1}) \tag{22}$$

As the iteration number increases, the particles will get closer to the optimal point(s), so the velocities should decrease. To ensure that happens and to ease the system's convergency, C_o is recalculated at each iteration with Equation 23. The remaining coefficients are constant throughout the optimization process.

$$C_o = C_{0,i} + \frac{k-1}{\mathrm{N_{it\_max}} - 1} (C_{o,f} - C_{0,i}) \tag{23}$$

With $C_{o,f}$ and $C_{0,i}$ being the final and initial values of C_o ($C_{o,f} < C_{0,i}$).

The particle position is then updated, resorting to Equation 24.

$$x_{i,n,k}^* = v_{i,n,k} + x_{i,n,k-1} \tag{24}$$

This new position should obey the upper and lower bounds defined for each variable. If this situation is verified, $x_{i,n}^* = x_{i,n,k}$. If not, the velocity of the particle is annulled ($v_{i,n,k} = 0$) and a new position is calculated. First, violation rates (w_L and w_U) are calculated to evaluate the maximum limit trespassing between all the decision variables as shown in Equations 25 and 26. Then, the maximum violation rate ($w = \max(w_L, w_U)$) is used to find the new particle position according to Equation 27.

$$w_L = \max_n \left(\frac{x_{n,lower} - x_{i,n,k}^*}{x_{i,n,k-1} - x_{n,lower}} \right) \tag{25}$$

$$w_U = \max_n \left(\frac{x_{i,n,k}^* - x_{n,upper}}{x_{n,upper} - x_{i,n,k-1}} \right) \tag{26}$$

$$x_{i,n,k} = x_{i,n,k-1} + \frac{x_{i,n,k}^* - x_{i,n,k-1}}{1 + w} \tag{27}$$

The complete PSO algorithm is depicted in Figure 4.

At the end of the algorithm, the matrix G_{best} contains the optimal point (in single-objective problems) or the optimal Pareto Front (in multi-objective problems) and the decision variables that lead to those solutions.

However, there might be close-to-optima solutions that are not contemplated in the optimal point/curve generated by the values in G_{best}. Therefore, the values of the particles generated

during the implementation of the algorithm were stored to determine the feasible operating regions.

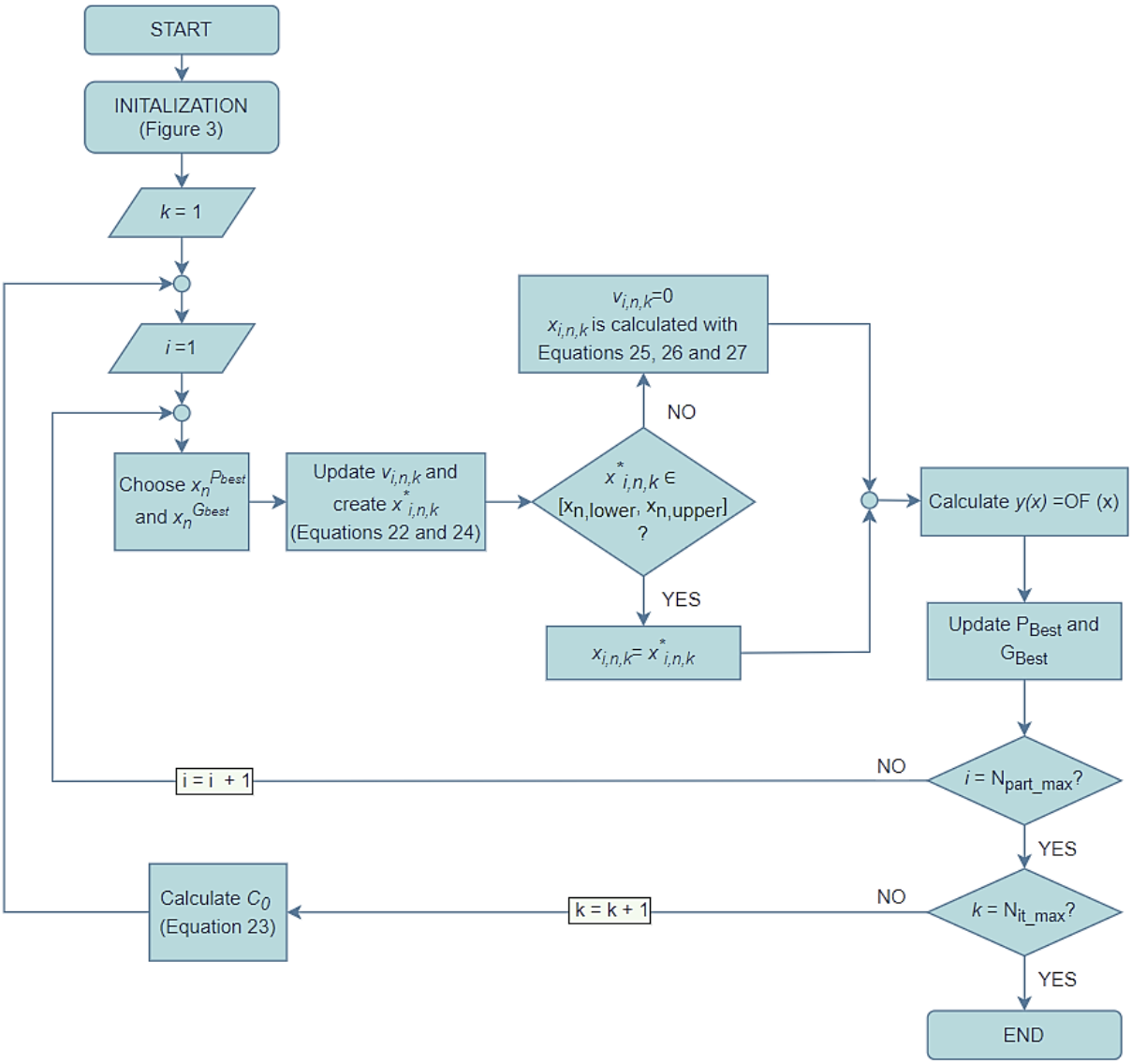

Figure 4. PSO algorithm.

3.4 Uncertainty assessment of the optimization problem

With the particles generated during the PSO implementation, it was possible to build a Feasible Operating Region (FOR) to contain the close-to-optimal points. The evaluation performed was based on a Fisher-Snedecor test, whose deduction was previously presented in the literature[38,40,41]. Given a certain particle i with the corresponding calculated value of the objective function(s), y_i, and the y_{best} obtained in the optimization, the particle i will be part of the FOR if the condition in Equation 28 is followed.

$$y_i \leq y_{best} + \frac{N_{exp}\, N_{DV}}{N_{exp} - N_{DV} + 1} F_\alpha(N_{DV}, N_{exp} - N_{DV} + 1) \quad (28)$$

With $\mathrm{N_{exp}}$ being the number of experiments considered and α the confidence interval.

The matrix y has the dimensions of $[\mathrm{N_{it\_max}} \times \mathrm{N_{part\_max}},\ \text{number of OFs}]$ while y_{best} has the dimensions of $[\text{number of particles in } \mathrm{G_{best}},\ \text{number of OFs}]$. The methodology presented in Figure 5 was followed to examine the particles.

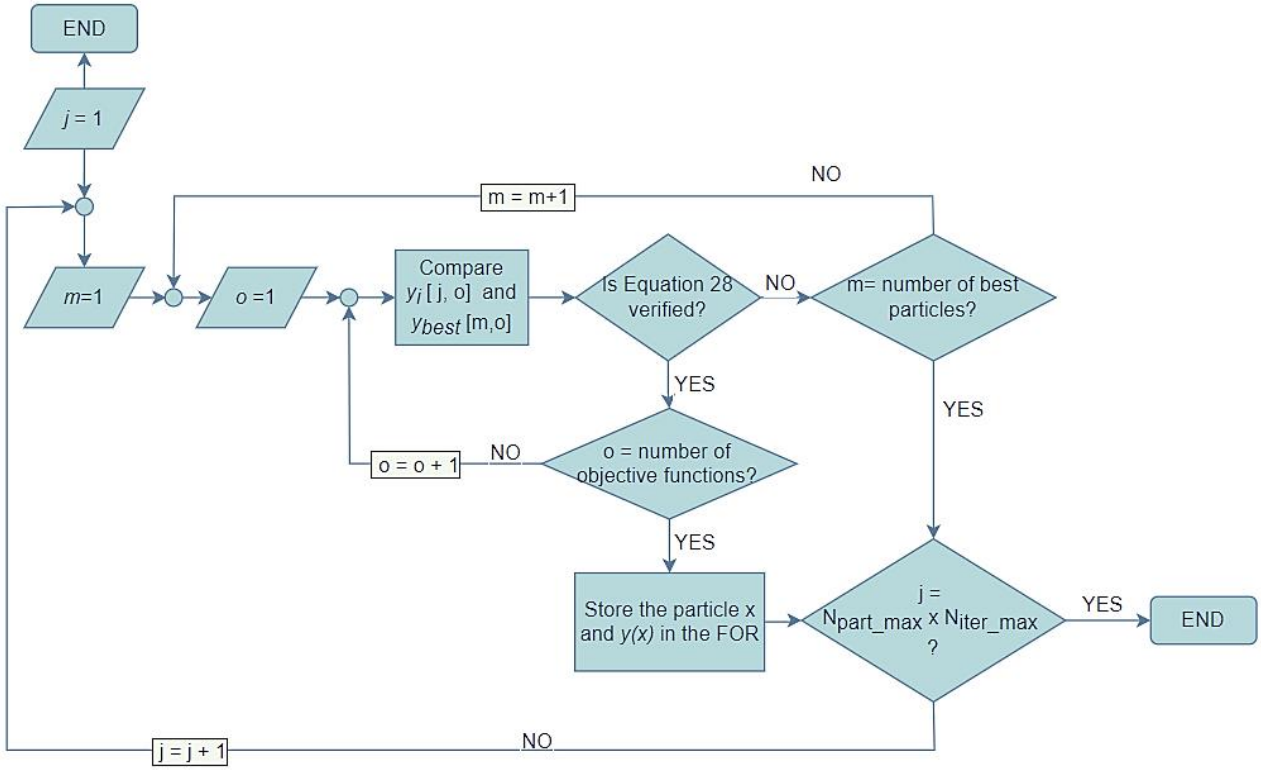

Figure 5. Construction of the Feasible Operating Region.

At the end of the evaluation, the stored points constitute the Feasible Operating Region . With the values in this region, it is possible to evaluate the uncertainty of the variable values that lead to the optimal solution. This assessment was made based on Type A Uncertainty, where the most probable value (MPV) for the decision variables (x_i) and their confidence intervals (CI) were obtained based on Equations 29, 30, and 31 [54].

$$\mathrm{MPV} = \frac{1}{N}\sum_{i=1}^{N} x_i \tag{29}$$

$$U = CF\sqrt{\frac{1}{N-1}\sum_{i=1}^{N}(x_i - \mathrm{MPV})^2} \tag{30}$$

$$\mathrm{CI} = [\mathrm{MPV} - U; \mathrm{MPV} + U] \tag{31}$$

Where N is the number of points, U is the uncertainty, and CF is the coverage factor (considered equal to 1.96, associated with a level of confidence of 95%).

In multi-objective optimization, the FOR was divided into 3 clusters to evaluate which conditions lead to the prevalence of one of the objectives or the compromise between them. This clusterization action was performed with the clusterdata function from MATLAB, applying the Linkage based on the "weighted" criterium [55]. This clusterization method is based on the mean distance between two clusters or a cluster and a point [56]. At last, the uncertainty assessment was also performed in the cluster evaluation.

3.5 Simulation scenarios and computational resources

The simulation and application of the PSO algorithm were implemented in a portable computer with 16 GB of RAM and a processor Intel(R) Core (TM) i7-10750H CPU @ 2.60GHz 2.59 GHz, using the Spider 5.1.5. associated with Python 3.9.7 64-bit. The clusterization was performed with MATLAB version R2021a 64-bit in a server with 64 GB of RAM and two processors Intel(R) Xeon(R) CPU E5-2650 v2 @ 2.60GHz 2.60 GHz .

The parameters applied in each study case, and the resulting runtimes are resumed in Table 3.

Table 3. Parameters used during PSO optimization.

Parameter	Case 1	Case 2	Case 3
N_{part_max}	3 000	4 000	500
N_{it_max}	200	400	200
$C_{o,i}$	0.9	0.9	0.9
$C_{0,f}$	0.4	0.4	0.4
C_1	2	2	2
C_2	2	2	2
α	0.9995	0.9995	0.9999
N_{exp}	3 000 000	3 000 000	1 000 000
Run time/s	3 480	12 858	368

The higher number of particles in single-objective optimization is justified by the need to have a larger number of particles in the convergency zone to ensure a good design of the confidence region. In the multi-objective problem, the number of particles had to be reduced; otherwise, the clusterization process would be compromised due to a lack of memory.

4 Results and discussion

4.1 Particle distribution evaluation

Before analyzing each optimization result, a good practice is to verify the particles' uniform distribution throughout the entire problem field. This is done to confirm the expected behavior of the algorithm, verifying if the particles traveled the whole landscape.

With that in mind, the objective function values for all the particle position history during the optimization were plotted in function of the material and the three different temperatures. The resulting plots can be seen in Figure B.1 in Appendix B for all the cases defined in the optimization problem.

The overall results reveal a good evaluation of the objective function landscape.

The only material that did not present a large volume of feasible particles was zeolite 13X (material 9). When looking at the particle distribution during the PSO procedure shown in Figure B.1, it was possible to see that most of the particles that evaluated that material returned the penalization value.

Considering a temperature set previously used in the literature [6], it was verified that it returned a q_{min} value higher than q_{max}. This indicates that there might be a problem with the isotherm fitting. However, the difference between the points collected from the literature and the value from the fitting was less than 10 %, despite the isotherm presenting a sharp rise of the adsorbed amounts at low pressures. A deeper analysis would be required to better understand the problem. Nevertheless, this issue was considered related to the adsorption equilibrium data and not the optimization procedure.

The T_{cond} did also present many unviable particles, which can be explained by the constraint that forces this variable to be 5 K lower than the desorption temperature and the fact that lower T_{des} was associated with better system performance, as will be discussed in the next sections.

Despite the strategy adopted for the penalization, it did not seem to be a trouble for the optimization procedure. The problem was therefore considered well evaluated, aside from the revealed issues with the material 9.

Furthermore, as demonstrated by Figure B.2 in Appendix B, the need to use a lower number of iterations did not prejudice the convergency of the particles towards the Pareto curve.

4.2 Single-objective optimization

4.2.1 Maximization of COP_{heat}

The optimization problem proposed in Case 1 was solved following the previously described methods. A most probable value of COP_{heat} equal to 1.86 was found. The best-suited material for the maximum performance was material 3 (MIL-100 (Fe)).

With the application of the Fisher-Snedecor test, it was possible to build the FOR with a confidence level of 0.9995. The uncertainty was computed based on the most probable value for each decision variable and the corresponding confidence interval. These results are displayed in Table 4.

Table 4. Most probable values for the decision variables and respective confidence intervals for maximization of COP_{heat}.

Decision variable	MPV	CI
T_{evap} /K	303	[301.4, 303]
T_{cond} /K	309	[309, 309.7]
T_{des} /K	345	[345, 354.7]
Material	3	[3]; [8]

As it is possible to see, T_{evap} optimum was at the value of the upper bound while T_{cond} and T_{des} converged to the lower bound. However, there is another suitable material that did not appear in the initial optimization result. The confidence interval is quite restricted for T_{evap} and T_{cond}, but the values for T_{des} presents a broader range. This is likely due to no consideration of the cost of the desorption process, allowing the use of a greater temperature despite the MPV being at the lower bound.

For reference, the $Cost_{IF}$ for the optimal point obtained was 0.72 €.

The feasible operating regions were plotted to better understand the different application zones for both materials, as shown in Figure 6. The value of Δq was also added to the analysis because a higher Δq leads to a higher amount of water condensed during the cycle, increasing the amount of heat released.

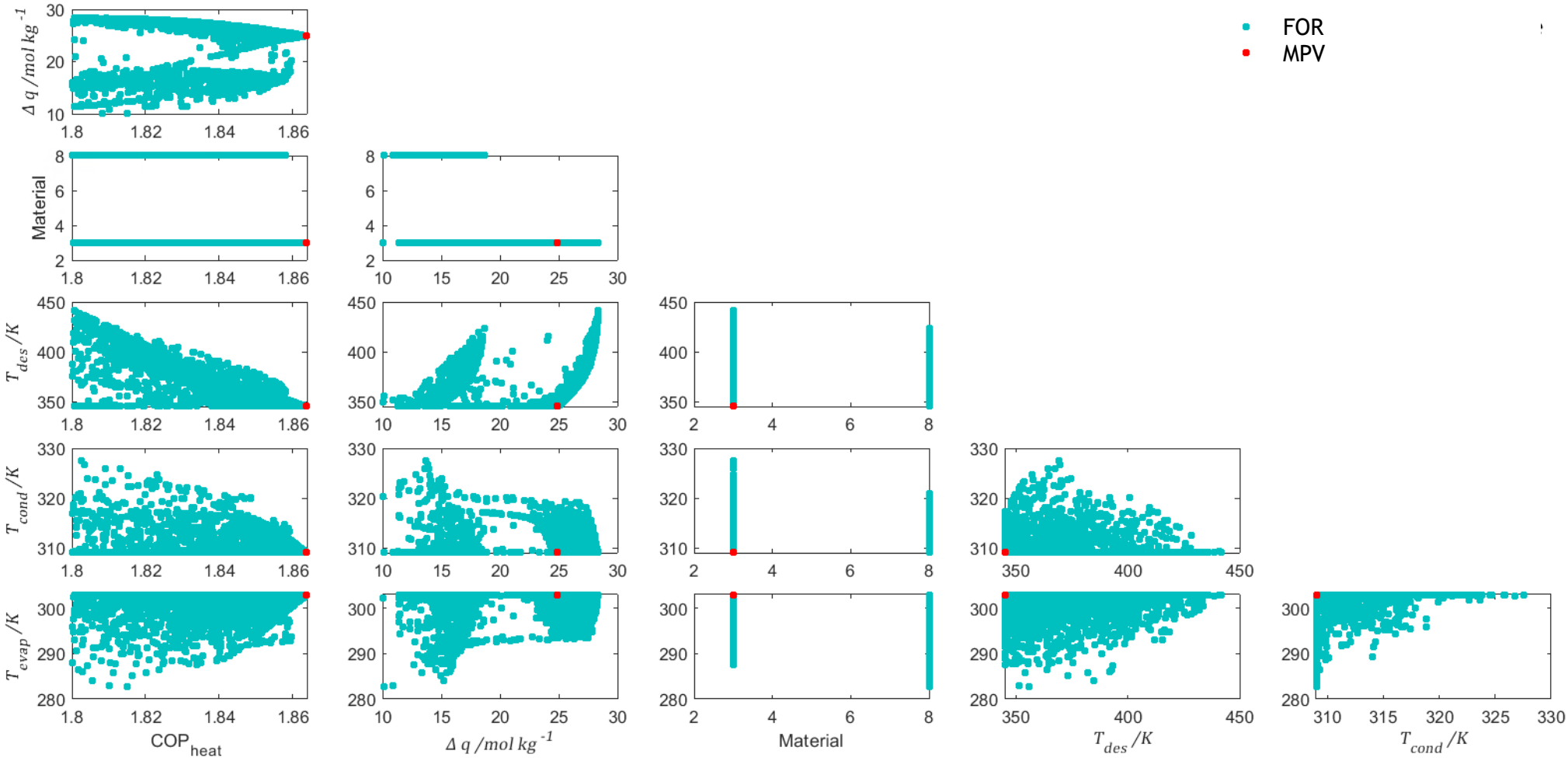

Figure 6. Feasible Operating Regions obtained by the Fisher-Snedecor test for T_{evap}, T_{cond}, T_{des} , Material, Δq and COP_{heat}.

The plot of the material vs. COP_{heat} shows that material 8 (MIL-125_NH_2) presents a slightly lower performance than material 3 (MIL-100 (Fe)), even though both materials show the MPV of temperatures within their operation region defined by the optimal region of operation. This is due to the higher water adsorption capacity presented by MIL-100 (Fe).

An interesting fact about the Δq is that it was not the highest value of this parameter to lead to the highest performance. This can be explained by the required temperature level to reach the maximum Δq being quite high (near 450 K), requiring more heat supplying and diminishing the COP_{heat}. Furthermore, the maximum performance of MIL-125_NH_2 is quite similar to the one presented by MIL-100 (Fe), despite the lower Δq. This is probably due to the lower isosteric adsorption heat of the MIL-125_NH_2, leading to a lower need for heating during the desorption phase.

The plots of temperature for this optimization basis do not show any correlation, aside for the tendency for lower values of T_{des} and T_{cond} and higher values of T_{evap}.

4.2.2 Minimization of $(\boldsymbol{Cost_{IF} - COP_{heat} \times EF})$

The single-objective approach of the multi-objective optimization led to an optimal value of 1.6 €. This corresponds to optimal values for $Cost_{IF}$ and for COP_{heat} of 0.15 € and 1.75, respectively. Now that a trade-off is considered, it is possible to see that both COP_{heat} and $Cost_{IF}$ tend to a lower value than the one found in the last section. The results of the uncertainty assessment are presented in Table 5, based on the FOR. In Figure 7, the feasible operating regions are depicted.

Table 5. Most probable values for the decision variables and respective confidence intervals for minimization of $(Cost_{IF} - COP_{heat} \times EF)$.

Decision variable	MPV	CI
T_{evap} /K	292.3	[290, 294.6]
T_{cond} /K	315.3	[313.3, 317.4]
T_{des} /K	345	[345, 347.6]
Material	3	[3]; [8]

The materials that best suited the problem remained the same as when the primary objective was to obtain the maximum COP_{heat}. The CI for T_{des} is more restricted now that cost is a factor in the optimization process and the MPV for the other two temperatures no longer corresponds to the lower bound of the previously defined range.

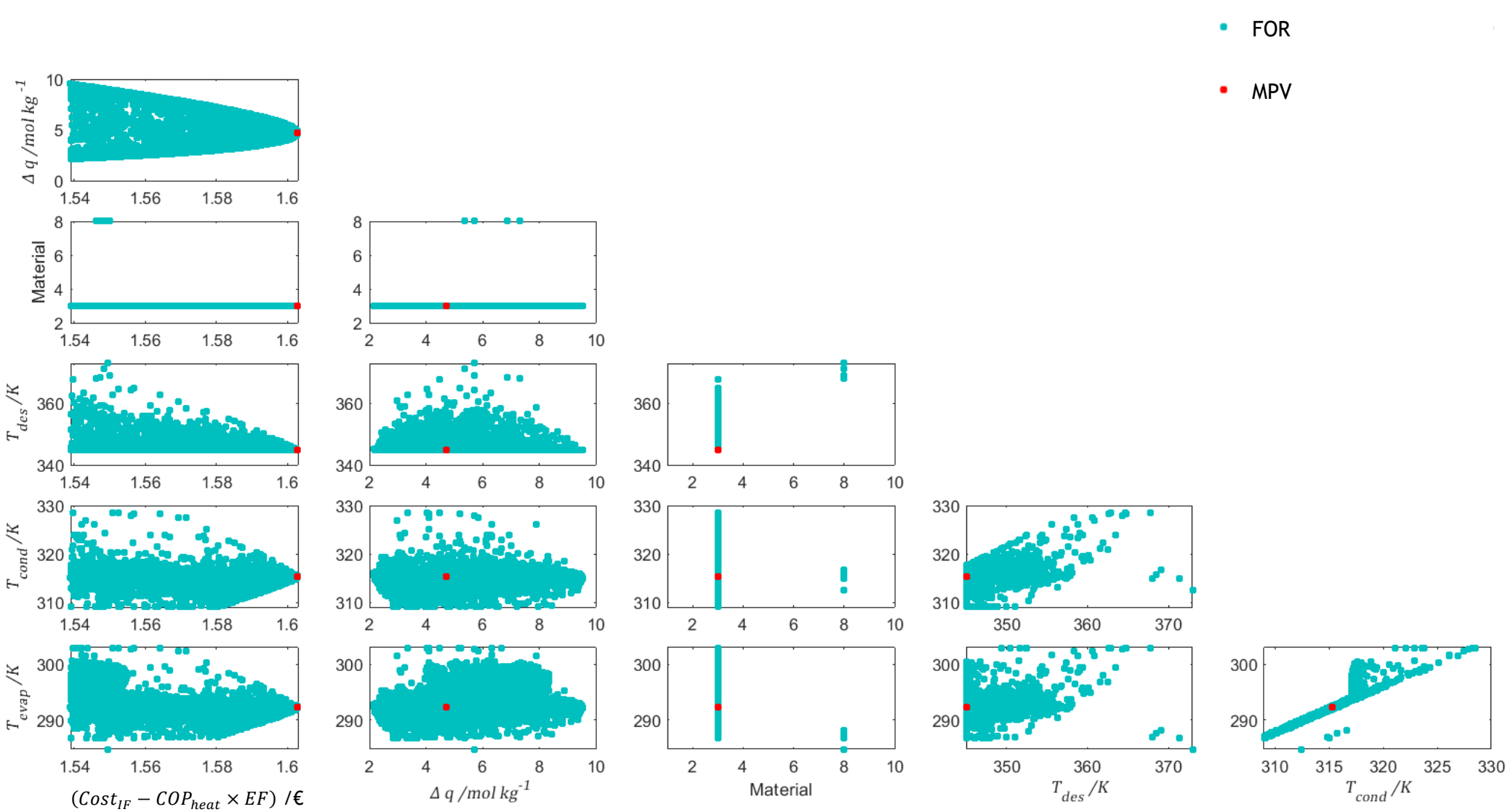

Figure 7. Feasible Operating Regions obtained by the Fisher-Snedecor test for T_{evap}, T_{cond}, T_{des} , Material, Δq and $(Cost_{IF} - COP_{heat} \times EF)$.

Based on the conclusion drawn when analyzing the previous case, the points with a Δq lower than 4.7 are the ones with a lower COP_{heat}. The data in the FOR for material 8 is above that value, prioritizing the performance of the adsorption-heat pump. The predominance of material 3 is evident, whereas it seemed to be a balance in the last case. Therefore, material 3 has been indicted as adequate for multiple regions of operation, while material 8 has a more restricted activity.

When looking at the variation of the adsorbed amount and the objective function with the temperatures, the data is dispersed over the high and low-performance zones. This dispersion was also present in Figure 6. It is then possible to conclude that no single temperature has a predominant influence on the operation of the heat pumps. Instead, the different combination of those three factors is the key to switch between a higher performance or a lower cost function.

This is reinforced by analyzing the plots that relate the three temperatures. T_{cond} and T_{evap} show an almost-linear dependency, probably due to the relation of these two temperatures with the pressure limits and the enthalpy of vaporization in the condenser. The higher T_{cond} is, the lower q_{max} is going to be, unless T_{evap} rises (to rise the pressure at which the adsorption takes place and therefore rising q_{max}). With the higher T_{cond}, the enthalpy of vaporization in the condenser becomes lower and less energy is produced by the heat pump.

T_{des} seems to be a conflicting temperature. On the one hand, the lower difference between the T_{des} and T_{cond} allows for a lower heat supply requirement for the heat pump. On the other hand, this lower difference causes an inefficient desorption process, especially taking into consideration that it occurs at a higher pressure than adsorption and that pressure is defined precisely by T_{cond}. This relation is evident in the plots, where the higher values of the desorption temperature only appear for higher values of the adsorption and evaporator temperatures.

In addition, the intertwining between the temperatures also depends on the shape of the isotherms for each material, so the variation in the adsorbed amount can be evaluated for each case. The isosteric heat of adsorption is also an important parameter that influences the energetic cost of desorption.

With the points in the confidence region, it is possible to calculate the individual values of the objective functions and draw an approximation of a limited Pareto Region, as pictured in Figure 8.

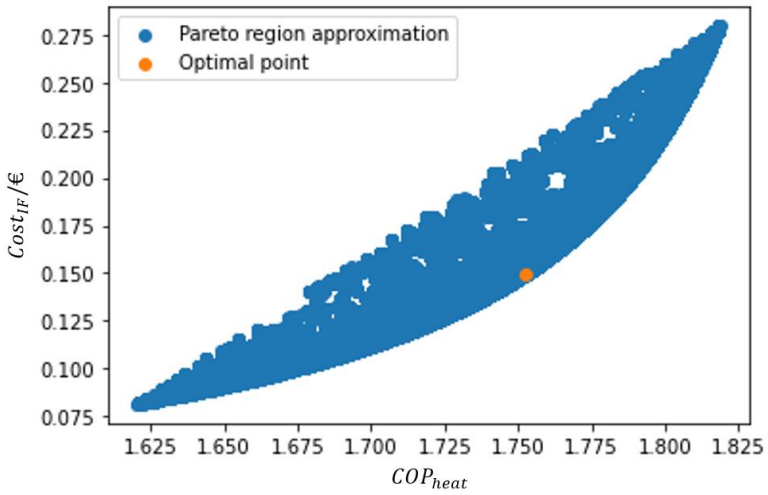

Figure 8. Pareto Region approximation.

The optimal points calculated range between 1.62 and 1.82 for COP_{heat} while the values for the $Cost_{IF}$ went from 0.08 € to 0.28 € approximately. It is possible to confirm that the objectives are evaluated based on a trade-off deal: to increase the heat pump performance, it is required to increase the cost of the process, while a low cost implies a close-to-zero heat production.

Although this rough design of the Pareto Region is not able to predict the complete evolution of the system within the ranges defined (for example, the point for the maximization of COP_{heat} does not belong in the presented intervals), it seems like a fair estimation for an intermediate behavior zone.

4.3 Multi-objective optimization

The previous section dealt with the single-objective optimization and an approximation to a Pareto Front. In this section, an actual Pareto Front will be computed by multi-objective optimization. Hence, it was possible to build a trustworthy Pareto Front, as presented in Figure 9.

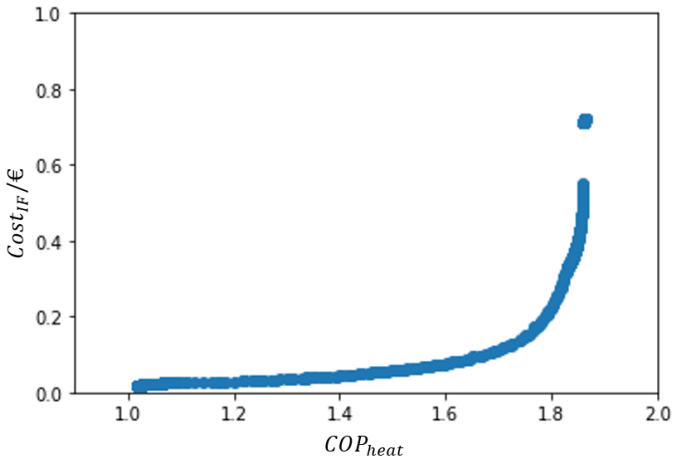

Figure 9. Pareto Front.

It can be observed that the $Cost_{IF}$ values vary between 0.02 and 0.72 €, while the COP_{heat} presented a variation between 1.02 and 1.86.

In addition, it is possible to see a gap within the points of the Pareto Front. A probable cause for this may be the almost vertical development of the front in that area, with no significant increase in the COP_{heat} but with a jump of almost 0.1 in terms of $Cost_{IF}$ which might have led to the non-dominance of such points. The upper branch of the curve presented a slight increase in the performance and was therefore considered dominant. Another possibility is that there were no feasible points in that region.

The first hypothesis was confirmed by drawing the Pareto Region according to the Fisher-Snedecor test, which is the orange curve shown in Figure 10. The test was performed with an $\alpha = 0.9999$, resulting in the inclusion of the y_i values that differed less than 0.03 (absolute value) from the y_{best} points presented in the Pareto curve.

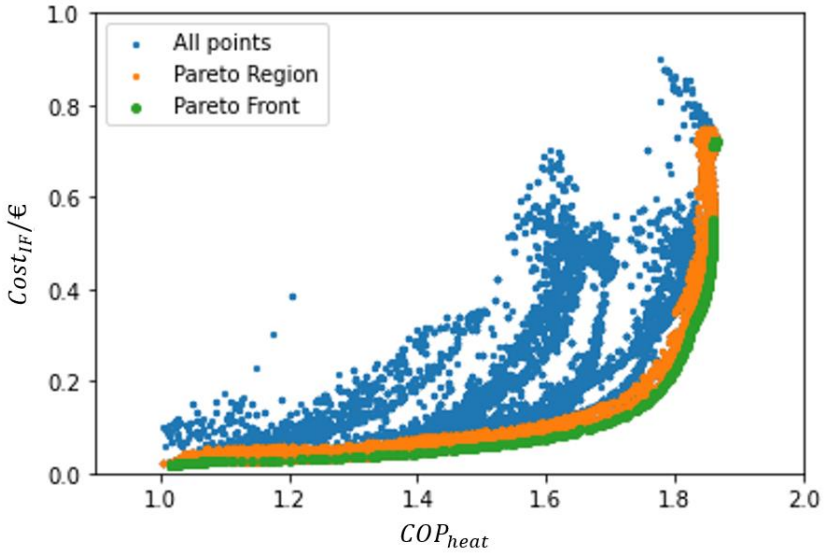

Figure 10. Comparison between all valid data produced by the PSO algorithm, the Pareto Region, and the Pareto Front.

This certifies the importance of drawing the FOR because possible solutions would not be detected otherwise. Furthermore, it can be seen in the figure that the test resulted in a good screening of the overall data available. Therefore, all the points in the new Pareto Region, the orange area, can be statistically considered as optimal as those in the Pareto Front.

In resemblance, the Pareto Front and Pareto Region can be plotted to see the difference in the optimal feasible region for each decision variable, as illustrated in Figure 11.

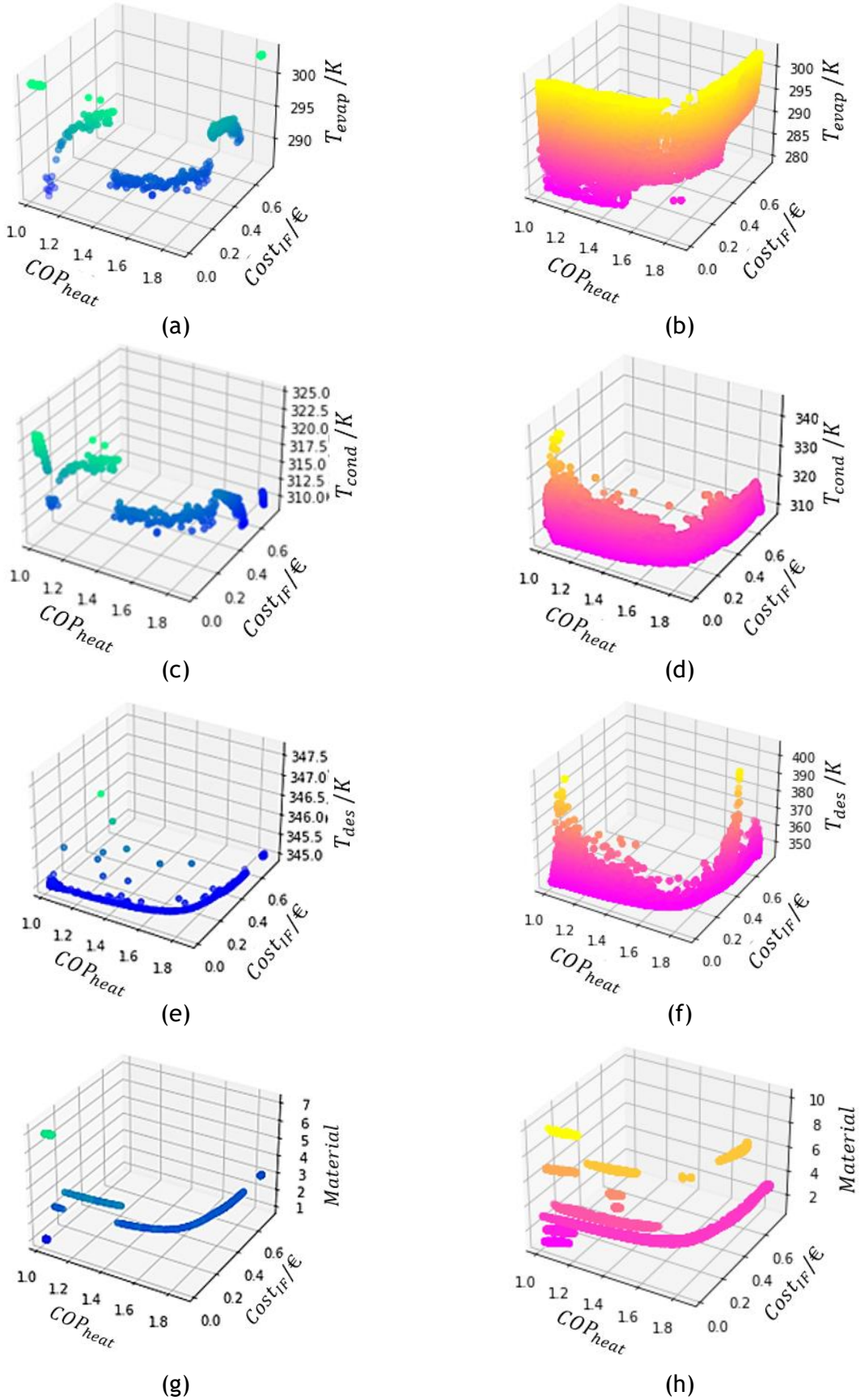

Figure 11. Pareto Fronts (a, c, e, h) and Pareto Regions (b, d, f, h) in function T_{evap} (a, b), T_{cond} (c, d), T_{des} (e, f) and the adsorbent material (g, h).

As it can be seen from the comparison of the two Pareto for each variable, the ranges admissible for each variable are largely expanded with a considerably small variation of the objective functions.

The T_{evap} shows a significant difference between the two zones. A curious fact is that for lower performances, the full range of the variable can be employed but as the values of COP_{heat} increase, the range becomes smaller, tendentiously to higher values of T_{evap}.

Similar behavior can be observed for $T_{cond} = T_{ads}$, where the lower temperatures lead to higher performance.

The variable T_{des}, that in the Pareto Front was mostly constant at 345 K, shows two peaks in temperature achieving almost the 400 K value in the Pareto Region. This is an odd event as for higher T_{des} the expected result would be a higher cost since more heat would be spent heating the adsorbent bed. This might be connected to the adsorbent materials since the expansion of the admissible results for the objective functions resulted in the opportunity to apply different materials that did not show as suitable before.

To find an explanation for the value of 400 K in the zone of low cost, the Δq obtained with the particles within the FOR was plotted against the cost, the COP_{heat} and $Cost_{IF}$ as visualized in Figure 12.

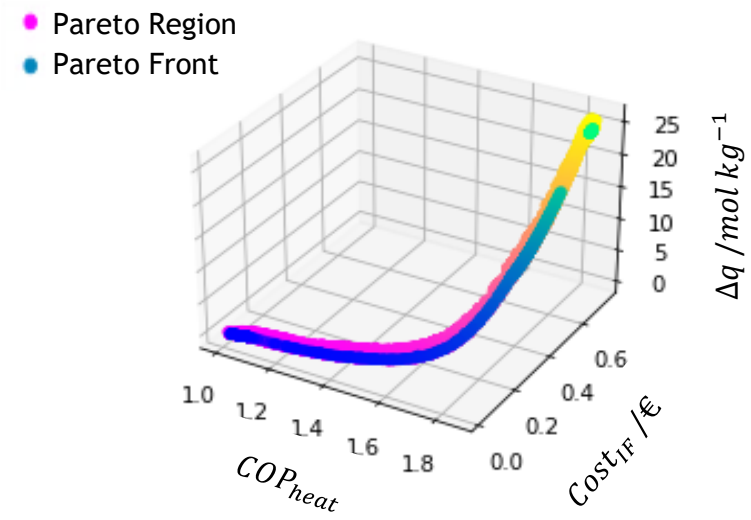

Figure 12. Relation between Δq with the Pareto Front and Pareto Region.

For the zone of worst performance and lower cost, the Δq is nearly 0, and as the difference between the maximum and the minimum adsorbed amounts rises, both cost and the coefficient of performance increase.

The variation of COP_{heat} can be explained by considering that the main contribution to this value is made by the heat released during the water condensation, as described in the literature

since $Q_{heat}+Q_{des}$ very often acquires a value similar to $Q_{cool} + Q_{ads}$ [4]. If $\Delta q = 0$, no water will be condensed, explaining the COP_{heat} value near to 1.

When it comes to cost, and analyzing the equations used for the heat calculations, it is possible to verify that the second term from Equation 2 is 0 when $\Delta q = 0$, meaning that the heat required is practically the heat for increasing the adsorbent and adsorbate temperatures. As predicted previously, the heat produced is equal to the provided, and there is no point in using the adsorption heat pump.

The Pareto Region data was grouped into clusters to better understand each objective function's predominance. The limits of the objective functions in each cluster and the number of points in each region are presented in Table 6. In Figure 13, the representation of the Pareto Front and the different feasible operating regions are presented. The distribution of the decision variables in each cluster is pictured in Figure 14. The Δq was also plotted to provide a better idea of the values of COP_{heat} and $Cost_{IF}$ resulting from the different combinations of the decision variables.

Table 6. Variation of COP_{heat} and $Cost_{IF}$ and number of points within each region.

Region	COP_{heat}	$Cost_{IF}$	Number of points
1	[1.02, 1.39]	[0.02, 0.07]	22046
2	[1.39, 1.82]	[0.07, 0.27]	14025
3	[1.82, 1.86]	[0.27, 0.75]	42578

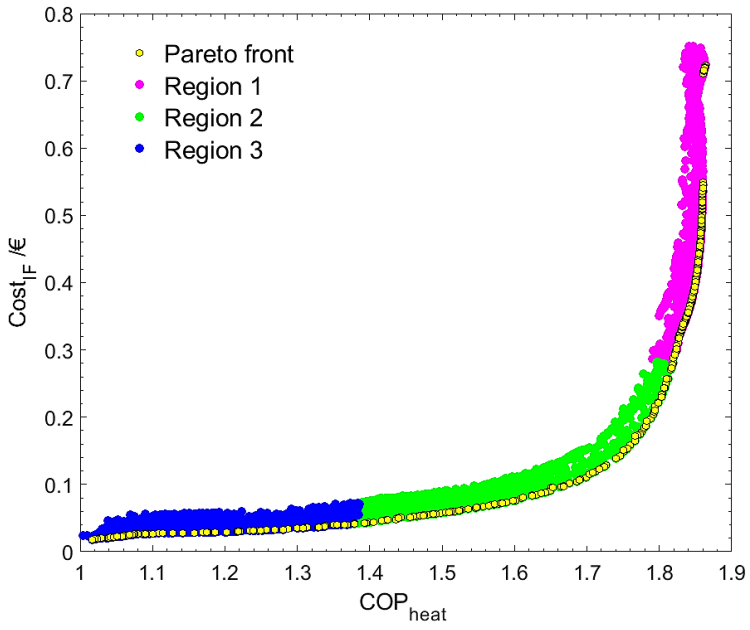

Figure 13. Clusterization of the data within the Pareto Region.

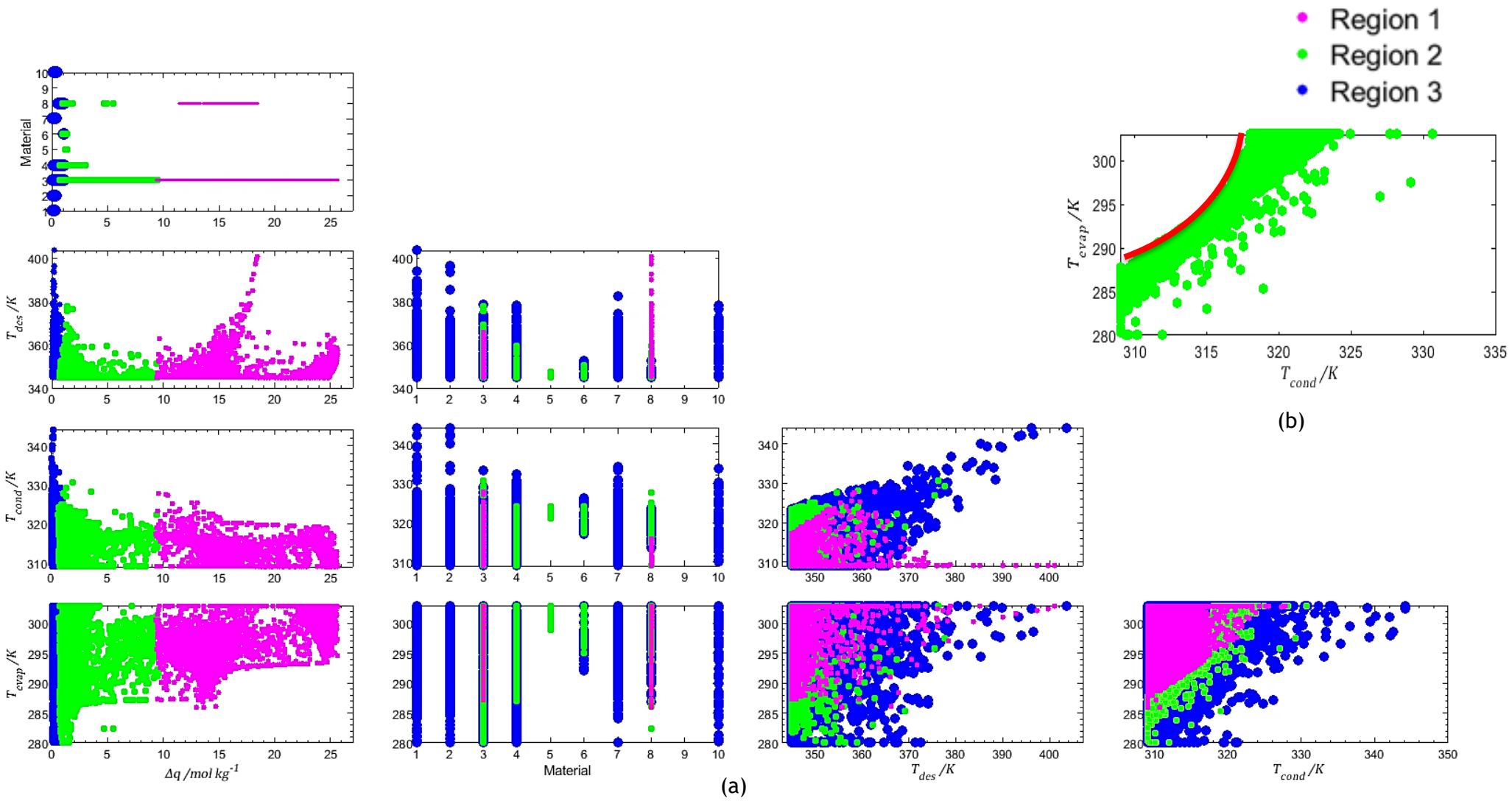

Figure 14. Feasible Operating Regions obtained by the Fisher-Snedecor test for T_{evap}, T_{cond}, T_{des} , Material and Δq (a) and the detail of T_{evap} vs T_{cond} for the Region 2 (b).

Regions 1 and 3 present more points than region 2, meaning the convergency was easier in zones where one of the objective functions was dominant, opposing the optimal calculation during the single optimization.

It can be seen by the plots that temperatures generally overlapped and tendentiously T_{cond} and T_{des} lean to lower values while T_{evap} rises.

The relation between T_{cond} and T_{evap} for Region 2 is presented in detail in Figure 14 (b). The temperature of the evaporator is always about 20 K lower than the temperature of the condenser, resembling the tendency observed before.

This limitation does not extend to the other two zones. In zone 3, the Δq is low, so the temperatures can range freely. In zone 1, the adsorbed amount is significantly higher, ranging from 10 to 27 mol kg^{-1}, despite the absence of the temperature limitation. In fact, the plot of T_{cond} vs T_{evap} for zone 3 is almost complementary to the one of zone 2, indicating that above the limit drawn for zone 2, the value of COP_{heat} and $Cost_{IF}$ reach their maximum values.

The main factor seems to be the different materials at play.

Both MIL-100 (Fe) (material 3) and MIL-125_NH_2 (Ti) (material 8) showed high capacities of adsorption at low pressures and relatively low isosteric heats of adsorption, leading to a greater performance under the most variable conditions. These two materials are present in Regions 1, 2 and 3, so they would be a good option for applications where the conditions could be regulated to choose a greater amount of heat produced or a lower-cost operation.

Nevertheless, MIL-100 (Fe) was the material with the most consistent performance, as seen by the continuous evolution of Δq across the three different zones. Furthermore, the high variation in the adsorbed amount can contribute to the integration of the adsorption based-heat pumps into water recovery systems[8], but further studies would be required to confirm this hypothesis.

MIL-160 (Al) (material 6), Al-FUM (material 4), and AQSOA FAM-Z02 (material 5) were also favorable materials for a midterm operation of the heat pumps. The MOFs can perform in a larger range of temperatures. However, the AQSOA FAM-Z02 was the only material to be exclusively considered for the intermediate region. This is probably due to the sharp isotherm, which makes desorption harder, and the high $(-\Delta H_{ads})$ value that this material presents, increasing the cost of the desorption operation. In fact, the range for the desorption temperature is the narrowest of all the evaluated materials.

The other materials showed low performance and poor adsorption/desorption capacity under the conditions studied. Most of them also possess a high isosteric heat of vaporization, which might contribute to the lower performance displayed during the optimization.

The uncertainty assessment results for each region are displayed in Table 7.

Table 7. Most probable values and confidence intervals for the decision variables in each region.

Decision variable	Region 1		Region 2		Region 3	
	MPV	CI	MPV	CI	MPV	CI
T_{evap} /K	297.5	[290.0, 303.0]	297.2	[286.0, 303.0]	298.4	[288.1, 303.0]
T_{cond} /K	313.0	[309.0, 318.8]	317.8	[310.3, 325.1]	317.1	[309.4, 324.7]
T_{des} /K	346.6	[345.0, 355.6]	345.9	[345.0, 350.95]	346.6	[345.0, 355.2]
Material	3	[3]; [8]	3	[3,6]; [8]	7	[1,4]; [6,8]; [10]

The T_{evap} and T_{des} values are very similar between regions, even though the confidence interval for T_{des} in Region 2 is slightly more restricted than in the other regions. The most notorious difference appears to be the adsorption temperature which is higher in the zones of lower cost. These values reflect the overlapping in the plots in Figure 14.

The MPVs were used to calculate the corresponding values of COP_{heat} and $Cost_{IF}$ that can be consulted in Table 8. Despite the small difference in temperatures between Region 1 and Region 2, it translates into a significant variation in cost and performance for the same material while agreeing to each cluster's framing values.

Table 8. Values of COP_{heat} and $Cost_{IF}$ obtained with the MPVs for each region.

Objective Function	Region 1	Region 2	Region 3
COP_{heat}	1.85	1.79	1.08
$Cost_{IF}$	0.69	0.26	0.03

The fact that a slight variation in the temperature values leads to such a difference in the adsorption-heat pump performance emphasizes the importance of mapping the performance regions for each material.

A form of doing this is through the analysis of Figure 14, following the paths demonstrated in Figures C.1 and C.2 in Appendix C. With that line of thinking, it is possible to evaluate the odd point that appeared during the analysis of Figure 11. The point that presents a 410 K for desorption temperature in zone 3 corresponds to the material 1, T_{cond}= 344 K and T_{evap}=303 K, leading to a COP_{heat} of 1.12 and a $Cost_{IF}$ of 0.06 €, with a Δq of 0.33 mol kg^{-1}. The point with the same desorption temperature for region 1 is obtained by using material 8, T_{cond}=309 K and T_{evap}=303 K, leading to a COP_{heat} of 1.83 and a $Cost_{IF}$ of 0.57 €, with a Δq of 18.5 mol kg^{-1}. The low Δq for the point in region 1 justifies the low COP_{heat} and the low cost, as mentioned before.

However, this logic is difficult to apply when the temperature plots are overlayed. An alternative is to plot a 3D graph correlating the three temperatures and the objective functions with the particles belonging to the Pareto Region for each material individually, as illustrated for MIL-100 (Fe) and MIL-125_NH_2 (Ti) in Figure 15.

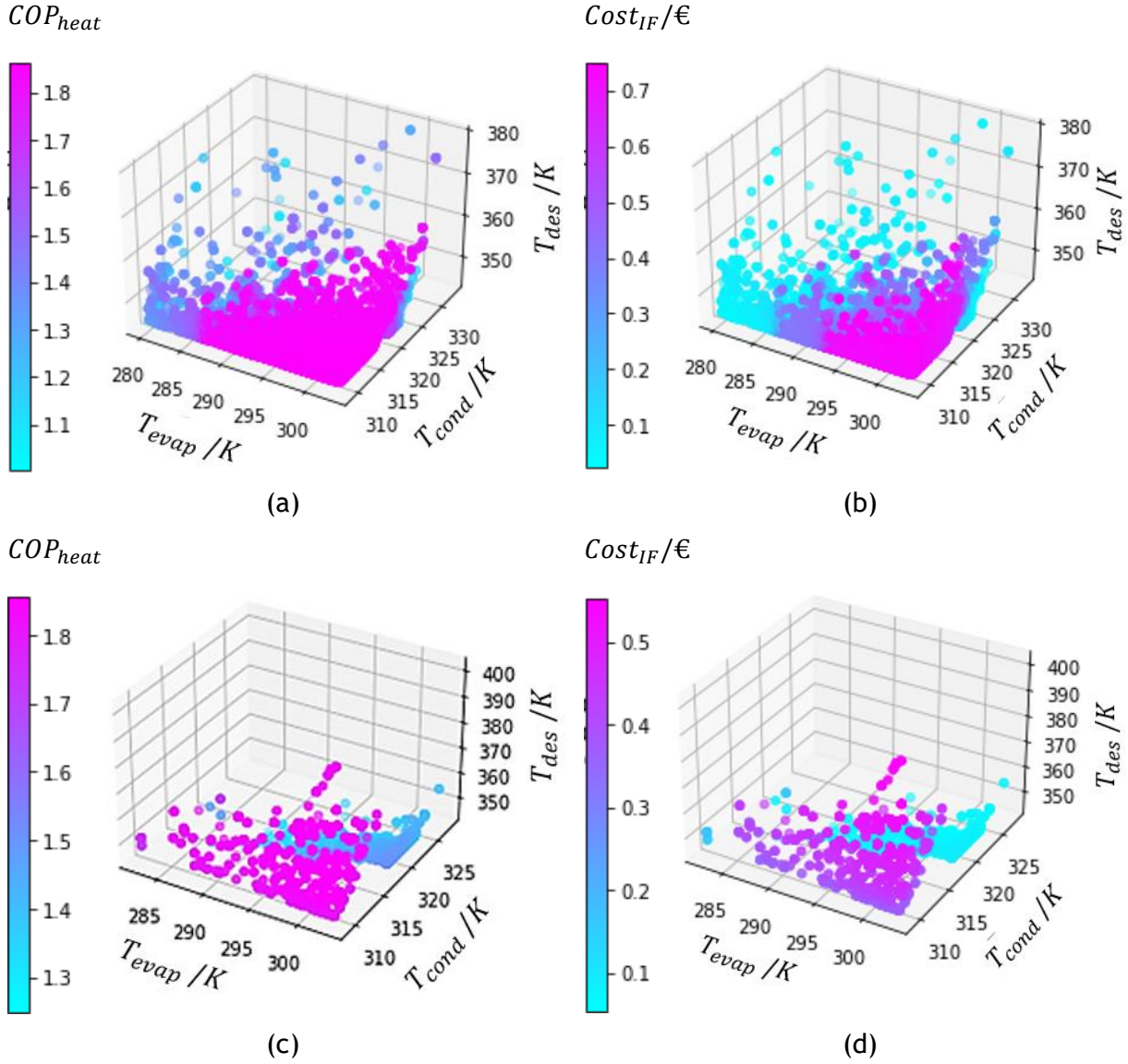

Figure 15. Temperature maps for materials 3 (MIL-100 (Fe)) (a, b) and 8 (MIL-125_NH_2 (Ti)) (c, d) for COP_{heat} (a, c) and the $Cost_{IF}$ (b, d).

The difference in the number of points for each material is notorious since only the optimal points were used. MIL-100 (Fe) allows for a larger temperature variability, which can be useful to control the heat transfer phenomenon when using the power supplied by the heat pump. Namely, operating at higher temperatures of the condenser can be more effective in heating since there will be a bigger gradient of temperatures.

However, the optimal performance point for the MIL-125_NH_2 (Ti) leads to a lower cost when compared to MIL-100 (Fe). Furthermore, MIL-125_NH_2 (Ti) seems to perform better even with

lower T_{evap}. Therefore, these plots confirm the importance of evaluating multiple temperature combinations because different materials can be suited for different zones of operation. These plots are also of great value for control operations since they map the temperature ranges in which the performance and the cost remain similar to the one intended.

4.4 Comparison between the single and multi-objective optimization

It is interesting to compare the results of the optimization. Both values obtained in cluster Regions 1 and 2 are very similar to those obtained when maximizing COP_{heat} or having a single-objective approach to the multi-optimization problem. Nevertheless, the analysis of optimal points provided by the single-objective method is limited.

Regarding the MPV and the IC, the multi-objective approach led to wider intervals than the single-objective one. One of the main differences was the MPV values for Region 1 in multi-optimization (corresponding to maximum values of COP_{heat}), which did not hit the side constraint values as in the single-objective, most likely due to the cost limitation. In addition, the MPV for Region 2 leads to a higher cost and performance than in the single objective. Hence, most points in that area lean towards the greatest performance over cost.

This provides evidence that the multi-optimization is capable of a more consistent evaluation of the multi-objective problem compared with the single-optimization. This conclusion is in line with the knowledge of optimization theory.

This can be perceived more easily when comparing the approximated Pareto Region obtained for the single-objective optimization of $(Cost_{IF} - COP_{heat} \times EF)$ with the Pareto Region obtained for the multi-objective optimization, as pictured in Figure 16.

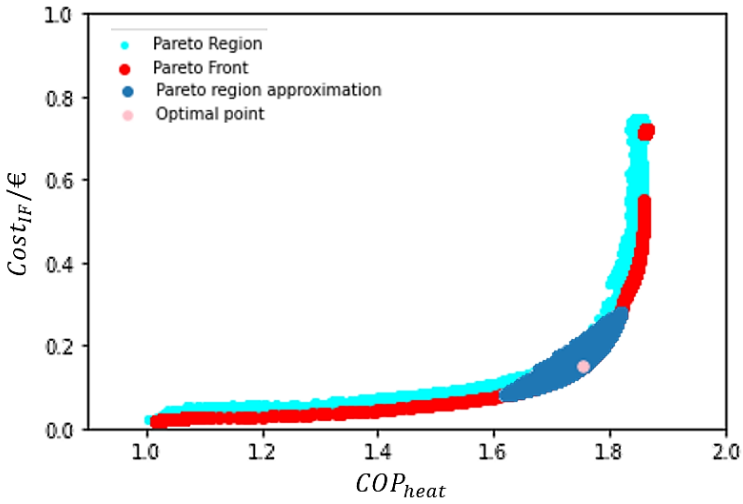

Figure 16. Comparison of optimal regions for the single objective approach and the multi-objective optimization.

The Pareto curve gives a broader perspective of the overall problem, whereas the approximation achieved with the single-objective approximation is restricted to the area of compromise between the two regions. As a matter of fact, the single-objective approach does not identify MIL-160 (Al), Al-FUM, or AQSOA FAM-Z02 as possible solutions for the mid-cost operation.

Furthermore, the approximated Pareto Region will consider all the points that achieve a difference within the given confidence level in the Fisher-Snedecor test. Some points of that region might not deliver a good performance or a lower cost and still have a difference between those values that makes them belong to the Feasible Operating Region.

Therefore, a single-objective is an excellent tool for finding higher-performance zones without limitations. When the objective is to find a compromise to different objectives, multi-objective optimization is the more indicated tool for the general overview of the problem.

5 Conclusion

The main objective of this work was to create a new framework that could simultaneously optimize the unit operation and the material screening process for adsorption heat pumps. The material screening introduced in the unit operation was effectively achieved within an optimization context.

Fisher-Snedecor test has proven to be a valuable tool, allowing for the expansion of the optimal point to an optimal region, and statistically detecting alternative optimal points that would otherwise be disregarded.

During the single-objective optimization, MIL-100 (Fe) and MIL-125_NH_2 (Ti) were the materials signaled as the most probable to lead to the best performance or reach a compromise between heat production and cost.

The multi-objective optimization corroborated with the single-objective results. However, in the first case, the MIL-160 (Al), Al-FUM, and AQSOA FAM-Z02 appeared as a possible alternative within the mid-cost operation zone. This demonstrates that multi-objective approaches allow for a better exploration of the problem's optimal solutions.

There were no viable points within the constraints considered for the zeolite 13X, but it might be linked with the data applied in the model construction and not with the optimization performance.

At last, the points in the optimal region were used for mapping the Feasible Operating Regions of the decision variables. The PSO allowed for the mapping of the regions that led to equivalent optimal values of COP_{heat} and $Cost_{IF}$, helping in the control of operations.

To conclude, the proposed framework provided a reliable tool for heat pumps optimization, material screening, and identifying all possible operating regions. Furthermore, it provides important insights regarding the system's behavior. For these reasons, the proposed approach to material screening has the potential to contribute significantly to the heat pump design and optimization literature.

6 Assessment of the work done

6.1 Objectives Achieved

The objective of implementing the PSO algorithm in material screening for adsorption heat pumps was completed successfully, with the evaluation of materials and subsequent mapping of the optimal points and performances.

6.2 Final Assessment

There is room for improvements in the work developed. A deeper study and reevaluation of the data collected for Zeolite 13X should be performed to confirm the reasons leading to the particles' penalization in the PSO optimization. Besides that, the possibility of performing the clusterization operation with a larger number of particles would be important to capture a more significant number of points in the optimal zone.

However, the procedure proposed in this work was applied successfully to the remaining materials. As such, a useful tool for simultaneous process optimization and material screening is available.

A suggestion for future work developments is evaluating the cooling potential to verify if the materials are fitted for both operating modes. It is also interesting to introduce different adsorbates as decision variables, increasing the complexity of the optimization problem. Furthermore, more complex models could potentially be applied, introducing a dynamic component in the evaluation, and bringing it closer to reality.

7 References

(1) de Lange, M. F.; Verouden, K. J. F. M.; Vlugt, T. J. H.; Gascon, J.; Kapteijn, F. Adsorption-Driven Heat Pumps: The Potential of Metal–Organic Frameworks. *Chemical Reviews* **2015**, *115* (22), 12205–12250. https://doi.org/10.1021/acs.chemrev.5b00059.

(2) eurostat. *Energy consumption in households*. https://ec.europa.eu/eurostat/statistics-explained/index.php?title=Energy_consumption_in_households&oldid=567183 (accessed 2022-06-20).

(3) eurostat. *Electricity production, consumption and market overview*. https://ec.europa.eu/eurostat/statistics-explained/index.php?title=Electricity_production,_consumption_and_market_overview#Electricity_generation (accessed 2022-06-20).

(4) Pinheiro, J. M.; Salústio, S.; Rocha, J.; Valente, A. A.; Silva, C. M. Adsorption Heat Pumps for Heating Applications. *Renewable and Sustainable Energy Reviews* **2020**, *119*, 109528. https://doi.org/10.1016/j.rser.2019.109528.

(5) Dias, J. M. S.; Costa, V. A. F. Adsorption Heat Pumps for Heating Applications: A Review of Current State, Literature Gaps and Development Challenges. *Renewable and Sustainable Energy Reviews* **2018**, *98*, 317–327. https://doi.org/10.1016/j.rser.2018.09.026.

(6) Liu, Z.; Li, W.; Cai, S.; Tu, Z.; Luo, X.; Li, S. Screening Versatile Water/Adsorbent Working Pairs for Wide Operating Conditions of Adsorption Heat Pumps. *Sustainable Energy Fuels* **2022**, *6* (2), 309–319. https://doi.org/10.1039/D1SE01819A.

(7) Boman, D. B.; Hoysall, D. C.; Pahinkar, D. G.; Ponkala, M. J.; Garimella, S. Screening of Working Pairs for Adsorption Heat Pumps Based on Thermodynamic and Transport Characteristics. *Applied Thermal Engineering* **2017**, *123*, 422–434. https://doi.org/10.1016/j.applthermaleng.2017.04.153.

(8) Silva, M. Water Harvesting by Adsorption Based Processes on MOFs. Ph.D. Thesis, Universidade do Porto, 2021.

(9) Zogg, M. *History of Heat Pumps - Swiss Contributions and International Milestones*; Switzerland, 2008.

(10) Sanner, B. B. Ground Source Heat Pumps – History, Development, Current Status, and Future Prospects; 2017.

(11) Kiss, A.; Ferreira, C. *Heat Pumps in Chemical Process Industry*; 2016. https://doi.org/10.1201/9781315371030.

(12) Zhang, J.; Zhang, H.-H.; He, Y.-L.; Tao, W.-Q. A Comprehensive Review on Advances and Applications of Industrial Heat Pumps Based on the Practices in China. *Applied Energy* **2016**, *178*, 800–825. https://doi.org/10.1016/j.apenergy.2016.06.049.

(13) Boman, D.; Raymond, A.; Garimella, S. *Adsorption Heat Pumps: Fundamentals and Applications*; 2021. https://doi.org/10.1007/978-3-030-72180-0.

(14) Ülkü, S. Adsorption Heat Pumps. *Journal of Heat Recovery Systems* **1986**, *6* (4), 277–284. https://doi.org/10.1016/0198-7593(86)90113-X.

(15) Demir, H.; Mobedi, M.; Ülkü, S. A Review on Adsorption Heat Pump: Problems and Solutions. *Renewable and Sustainable Energy Reviews* **2008**, *12* (9), 2381–2403. https://doi.org/10.1016/j.rser.2007.06.005.

(16) Steven Brown, J.; Domanski, P. A. Review of Alternative Cooling Technologies. *Applied Thermal Engineering* **2014**, *64* (1), 252–262. https://doi.org/10.1016/j.applthermaleng.2013.12.014.

(17) Bolaji, B. O.; Huan, Z. Ozone Depletion and Global Warming: Case for the Use of Natural Refrigerant – a Review. *Renewable and Sustainable Energy Reviews* **2013**, *18*, 49–54. https://doi.org/10.1016/j.rser.2012.10.008.

(18) Corberán, J. M.; Segurado, J.; Colbourne, D.; Gonzálvez, J. Review of Standards for the Use of Hydrocarbon Refrigerants in A/C, Heat Pump and Refrigeration Equipment. *International Journal of Refrigeration* **2008**, *31* (4), 748–756. https://doi.org/10.1016/j.ijrefrig.2007.12.007.

(19) Wu, D.; Hu, B.; Wang, R. Z. Vapor Compression Heat Pumps with Pure Low-GWP Refrigerants. *Renewable and Sustainable Energy Reviews* **2021**, *138*, 110571. https://doi.org/10.1016/j.rser.2020.110571.

(20) Tu, Y.; Wang, R.; Zhang, Y.; Wang, J. Progress and Expectation of Atmospheric Water Harvesting. *Joule* **2018**, *2* (8), 1452–1475. https://doi.org/10.1016/j.joule.2018.07.015.

(21) Freni, A.; Maggio, G.; Sapienza, A.; Frazzica, A.; Restuccia, G.; Vasta, S. Comparative Analysis of Promising Adsorbent/Adsorbate Pairs for Adsorptive Heat Pumping, Air Conditioning and Refrigeration. *Applied Thermal Engineering* **2016**, *104*, 85–95. https://doi.org/10.1016/j.applthermaleng.2016.05.036.

(22) Srivastava, N. C.; Eames, I. W. A Review of Adsorbents and Adsorbates in Solid–Vapour Adsorption Heat Pump Systems. *Applied Thermal Engineering* **1998**, *18* (9), 707–714. https://doi.org/10.1016/S1359-4311(97)00106-3.

(23) Caprì, A.; Frazzica, A.; Calabrese, L. Recent Developments in Coating Technologies for Adsorption Heat Pumps: A Review. *Coatings* **2020**, *10* (9). https://doi.org/10.3390/coatings10090855.

(24) Pesaran, A.; Lee, H.; Hwang, Y.; Radermacher, R.; Chun, H.-H. Review Article: Numerical Simulation of Adsorption Heat Pumps. *Energy* **2016**, *100*, 310–320. https://doi.org/10.1016/j.energy.2016.01.103.

(25) Gräber, M.; Kirches, C.; Bock, H. G.; Schlöder, J. P.; Tegethoff, W.; Köhler, J. Determining the Optimum Cyclic Operation of Adsorption Chillers by a Direct Method for Periodic Optimal Control. *International Journal of Refrigeration* **2011**, *34* (4), 902–913. https://doi.org/https://doi.org/10.1016/j.ijrefrig.2010.12.021.

(26) Lanzerath, F.; Bau, U.; Seiler, J.; Bardow, A. Optimal Design of Adsorption Chillers Based on a Validated Dynamic Object-Oriented Model. *Science and Technology for the Built Environment* **2015**, *21* (3), 248–257. https://doi.org/10.1080/10789669.2014.990337.

(27) Venter, G. Review of Optimization Techniques. In *Encyclopedia of Aerospace Engineering*; John Wiley & Sons, Ltd, 2010. https://doi.org/10.1002/9780470686652.eae495.

(28) Cavazzuti, M. Introduction. In *Optimization Methods: From Theory to Design Scientific and Technological Aspects in Mechanics*; Cavazzuti, M., Ed.; Springer Berlin Heidelberg: Berlin, Heidelberg, 2013; pp 1–10. https://doi.org/10.1007/978-3-642-31187-1_1.

(29) Rangaiah, G. P.; Feng, Z.; Hoadley, A. F. Multi-Objective Optimization Applications in Chemical Process Engineering: Tutorial and Review. *Processes* **2020**, *8* (5). https://doi.org/10.3390/pr8050508.

(30) Madoumier, M.; Trystram, G.; Sébastian, P.; Collignan, A. Towards a Holistic Approach for Multi-Objective Optimization of Food Processes: A Critical Review. *Trends in Food Science & Technology* **2019**, *86*, 1–15. https://doi.org/10.1016/j.tifs.2019.02.002.

(31) Cui, Y.; Geng, Z.; Zhu, Q.; Han, Y. Review: Multi-Objective Optimization Methods and Application in Energy Saving. *Energy* **2017**, *125*, 681–704. https://doi.org/10.1016/j.energy.2017.02.174.

(32) Estupiñan Perez, L.; Sarkar, P.; Rajendran, A. Experimental Validation of Multi-Objective Optimization Techniques for Design of Vacuum Swing Adsorption Processes. *Separation and Purification Technology* **2019**, *224*, 553–563. https://doi.org/10.1016/j.seppur.2019.05.039.

(33) Lee, W.-S.; Kung, C.-K. Optimization of Heat Pump System in Indoor Swimming Pool Using Particle Swarm Algorithm. *Applied Thermal Engineering* **2008**, *28* (13), 1647–1653. https://doi.org/10.1016/j.applthermaleng.2007.11.003.

(34) Rahman, A. F. M. M.; Miyazaki, T.; Ueda, Y.; Saha, B. B.; Akisawa, A. Performance Comparison of Three-Bed Adsorption Cooling System With Optimal Cycle Time Setting. *Heat Transfer Engineering* **2013**, *34* (11–12), 938–947. https://doi.org/10.1080/01457632.2012.753571.

(35) Li, R.; Dai, Y.; Cui, G. Multi-Objective Optimization of Solar Powered Adsorption Chiller Combined with River Water Heat Pump System for Air Conditioning and Space Heating Application. *Energy* **2019**, *189*, 116141. https://doi.org/10.1016/j.energy.2019.116141.

(36) Rajagopalan, A. K.; Avila, A. M.; Rajendran, A. Do Adsorbent Screening Metrics Predict Process Performance? A Process Optimisation Based Study for Post-Combustion Capture of CO2. *International Journal of Greenhouse Gas Control* **2016**, *46*, 76–85. https://doi.org/10.1016/j.ijggc.2015.12.033.

(37) Nogueira, I. B. R.; Dias, R. O. M.; Rebello, C. M.; Costa, E. A.; Santana, V. v; Rodrigues, A. E.; Ferreira, A.; Ribeiro, A. M. A Novel Nested Loop Optimization Problem Based on Deep Neural Networks and Feasible Operation Regions Definition for Simultaneous Material Screening and Process Optimization. *Chemical Engineering Research and Design* **2022**, *180*, 243–253. https://doi.org/10.1016/j.cherd.2022.02.013.

(38) Rebello, C. M.; Martins, M. A. F.; Loureiro, J. M.; Rodrigues, A. E.; Ribeiro, A. M.; Nogueira, I. B. R. From an Optimal Point to an Optimal Region: A Novel Methodology for Optimization of Multimodal Constrained Problems and a Novel Constrained Sliding Particle Swarm Optimization Strategy. *Mathematics* **2021**, *9* (15). https://doi.org/10.3390/math9151808.

(39) Nogueira, I. B. R.; Martins, M. A. F.; Requião, R.; Oliveira, A. R.; Viena, V.; Koivisto, H.; Rodrigues, A. E.; Loureiro, J. M.; Ribeiro, A. M. Optimization of a True Moving Bed Unit and Determination of Its Feasible Operating Region Using a Novel Sliding Particle Swarm Optimization. *Computers & Industrial Engineering* **2019**, *135*, 368–381. https://doi.org/10.1016/j.cie.2019.06.020.

(40) Rebello, C. M.; Martins, M. A. F.; Santana, D. D.; Rodrigues, A. E.; Loureiro, J. M.; Ribeiro, A. M.; Nogueira, I. B. R. From a Pareto Front to Pareto Regions: A Novel Standpoint for Multiobjective Optimization. *Mathematics* **2021**, *9* (24). https://doi.org/10.3390/math9243152.

(41) Rebello, C. M.; Martins, M. A. F.; Rodrigues, A. E.; Loureiro, J. M.; Ribeiro, A. M.; Nogueira, I. B. R. A Novel Standpoint of Pressure Swing Adsorption Processes Multi-

Objective Optimization: An Approach Based on Feasible Operation Region Mapping. *Chemical Engineering Research and Design* **2022**, *178*, 590–601. https://doi.org/10.1016/j.cherd.2021.12.047.

(42) Critoph, R. E. Performance Limitations of Adsorption Cycles for Solar Cooling. *Solar Energy* **1988**, *41* (1), 21–31. https://doi.org/10.1016/0038-092X(88)90111-9.

(43) Aristov, Yu. I.; Tokarev, M. M.; Sharonov, V. E. Universal Relation between the Boundary Temperatures of a Basic Cycle of Sorption Heat Machines. *Chemical Engineering Science* **2008**, *63* (11), 2907–2912. https://doi.org/10.1016/j.ces.2008.03.011.

(44) NIST. *Liquid Phase Heat Capacity (Shomate Equation) for water*. https://webbook.nist.gov/cgi/cbook.cgi?ID=C7732185&Mask=2#Thermo-Condensed (accessed 2022-04-15).

(45) NIST. *Antoine Equation Parameters for water*. https://webbook.nist.gov/cgi/cbook.cgi?ID=C7732185&Mask=4#Thermo-Phase (accessed 2022-04-15).

(46) Silva, M. P.; Ribeiro, A. M.; Silva, C. G.; Narin, G.; Nogueira, I. B. R.; Lee, U.-H.; Faria, J. L.; Loureiro, J. M.; Chang, J.-S.; Rodrigues, A. E.; Ferreira, A. Water Vapor Harvesting by a (P)TSA Process with MIL-125(Ti)_NH2 as Adsorbent. *Separation and Purification Technology* **2020**, *237*, 116336. https://doi.org/10.1016/j.seppur.2019.116336.

(47) Silva, M. P.; Ribeiro, A. M.; Silva, C. G.; Ho Cho, K.; Lee, U.-H.; Faria, J. L.; Loureiro, J. M.; Chang, J.-S.; Rodrigues, A. E.; Ferreira, A. Atmospheric Water Harvesting on MIL-100(Fe) upon a Cyclic Adsorption Process. *Separation and Purification Technology* **2022**, *290*, 120803. https://doi.org/10.1016/j.seppur.2022.120803.

(48) Silva, M. P.; Ribeiro, A. M.; Silva, C. G.; Nogueira, I. B. R.; Cho, K.-H.; Lee, U.-H.; Faria, J. L.; Loureiro, J. L.; Chang, J.-S.; Rodrigues, A. E.; Ferreira, A. MIL-160(Al) MOF's Potential in Adsorptive Water Harvesting. *Adsorption* **2021**, *27* (2), 213–226. https://doi.org/10.1007/s10450-020-00286-5.

(49) Direção-Geral de Energia e Geologia. *Preços de eletricidade e gás natural*. https://www.dgeg.gov.pt/pt/estatistica/energia/precos-de-energia/precos-de-eletricidade-e-gas-natural/?fbclid=IwAR3xrZIAC4PHSMibxOe5ebr67h_V6_g1vhuj7keLsQyEXG5tlZLAeAVLqoM (accessed 2022-05-22).

(50) Banks, A.; Vincent, J.; Anyakoha, C. A Review of Particle Swarm Optimization. Part I: Background and Development. *Natural Computing* **2007**, *6* (4), 467–484. https://doi.org/10.1007/s11047-007-9049-5.

(51) Poli, R.; Kennedy, J.; Blackwell, T. Particle Swarm Optimization. *Swarm Intelligence* **2007**, *1* (1), 33–57. https://doi.org/10.1007/s11721-007-0002-0.

(52) Sinan Hasanoglu, M.; Dolen, M. Multi-Objective Feasibility Enhanced Particle Swarm Optimization. *Engineering Optimization* **2018**, *50* (12), 2013–2037. https://doi.org/10.1080/0305215X.2018.1431232.

(53) Deutsch, J. L.; Deutsch, C. v. Latin Hypercube Sampling with Multidimensional Uniformity. *Journal of Statistical Planning and Inference* **2012**, *142* (3), 763–772. https://doi.org/10.1016/j.jspi.2011.09.016.

(54) BIPM; IFCC; ILAC; ISO; IUPAC; IUPAP; OIML. *Guide to the Expression of Uncertainty in Measurement JCGM 100:2008, GUM 1995 with Minor Corrections,*; 2008.

(55) MathWorks. *clusterdata*. https://www.mathworks.com/help/stats/clusterdata.html#mw_04fa2b1a-9072-4203-baed-a90e72c8df34 (accessed 2022-06-01).

(56) MathWorks. *linkage*. https://www.mathworks.com/help/stats/linkage.html#mw_08b425f7-fc8c-480a-b618-f768817e8e11 (accessed 2022-06-01).

Appendix A. Adsorbents data

A. 1. Adsorption isotherms

For MIL-100 (Fe), MIL-125_NH_2 (Ti), MIL-160 (Al), CAU-10, and Al-FUM, the data of water adsorption and the isotherm model parameters were retrieved from previous works developed in LRSE-LCM[1-4], with the adsorbent being supplied by KRICT (Korea Research Institute of Chemical Technology). For the remaining materials, the data was collected from the identified sources in each subsection and later compared. The dataset with the larger range of temperatures and pressures was fitted by an adjustment with the chosen isotherm model presented before in Chapter 2.

A.1. 1. MIL-100 (Fe)

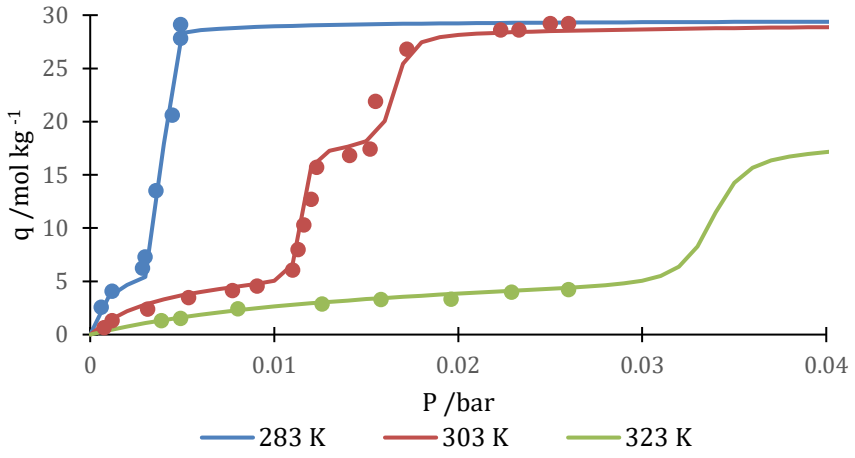

Figure A. 1. MIL-100 (Fe) dataset adjustment to the DISL isotherm.[1,4]

Table A. 1. DISL parameters for water adsorption in MIL-100 (Fe).[1,4]

Parameter	Value	Parameter	Value
$q_{sat\,L}$ /mol kg^{-1}	6.84	$K_{\infty,L}$ /bar^{-1}	1.15 × 10^{-7}
$q_{sat\,I,1}$ /mol kg^{-1}	12.3	$-\Delta H_{I,1}$ /kJ mol^{-1}	43.9
$q_{sat\,I,2}$ /mol kg^{-1}	10.4	$-\Delta H_{I,2}$ /kJ mol^{-1}	46.8
$K_{\infty,I,1}$ /bar^{-1}	2.35 × 10^{-6}	$-\Delta H_{o,1}$ /kJ mol^{-1}	20.5
$K_{\infty,I,2}$ /bar^{-1}	5.17 × 10^{-7}	$-\Delta H_{o,2}$ /kJ mol^{-1}	1.33
$K_{\infty,o,1}$ /bar^{-1}	1.04 × 10^{-5}	$-\Delta H_{L}$ /kJ mol^{-1}	54.0
$K_{\infty,o,2}$ /bar^{-1}	2.34 × 10^{-2}		

A.1. 2. MIL-125_NH_2 (Ti)

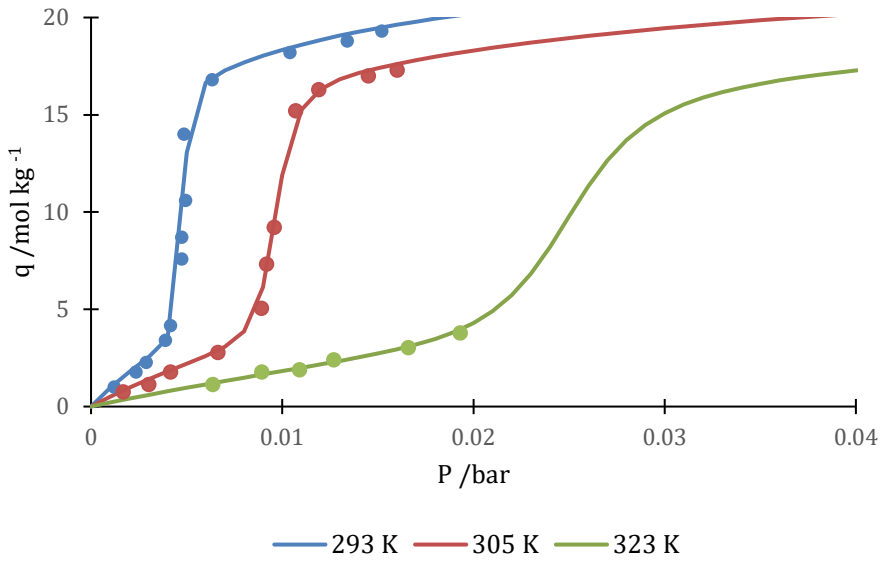

Figure A. 2. MIL-125_NH_2 (Ti) dataset adjustment to the Ising-Langmuir isotherm.[2,4]

Table A. 2. Ising-Langmuir isotherm parameters for water adsorption in MIL-125_NH_2 (Ti). [2,4]

Parameter	Value
$q_{sat\,I}$ /mol kg^{-1}	13.0
$q_{sat\,L}$ /mol kg^{-1}	11.0
$K_{\infty,I}$ /bar^{-1}	3.81 × 10^{-6}
$K_{\infty,o}$ /bar^{-1}	0.299
$K_{\infty,L}$ /bar^{-1}	2.14 × 10^{-6}
$-\Delta H_I$ /kJ mol^{-1}	43.4
$-\Delta H_0$ /kJ mol^{-1}	0.0
$-\Delta H_L$ /kJ mol^{-1}	42.9

A.1. 3. MIL-160 (Al)

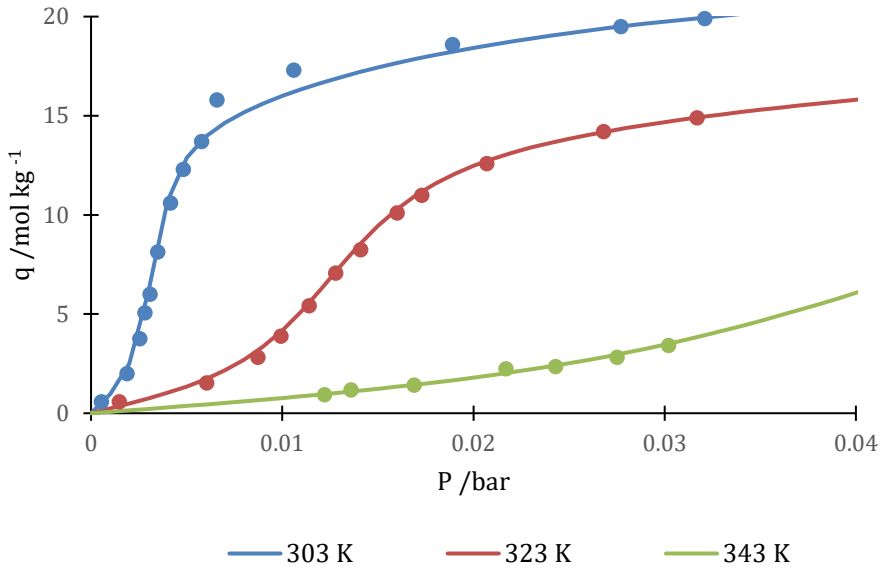

Figure A. 3. MIL-160 (Al) dataset adjustment to the Ising-Langmuir isotherm.[3,4]

Table A. 3. Ising-Langmuir isotherm parameters for water adsorption in MIL-160 (Al). [3,4]

Parameter	Value
$q_{sat\,I}$ /mol kg^{-1}	11.3
$q_{sat\,L}$ /mol kg^{-1}	13.2
$K_{\infty,I}$ /bar^{-1}	5.24×10^{-8}
$K_{\infty,o}$ /bar^{-1}	2.81×10^{-7}
$K_{\infty,L}$ /bar^{-1}	7.08×10^{-9}
$-\Delta H_I$ /kJ mol^{-1}	56.6
$-\Delta H_0$ /kJ mol^{-1}	43.9
$-\Delta H_L$ /kJ mol^{-1}	57.6

A.1. 4. CAU-10

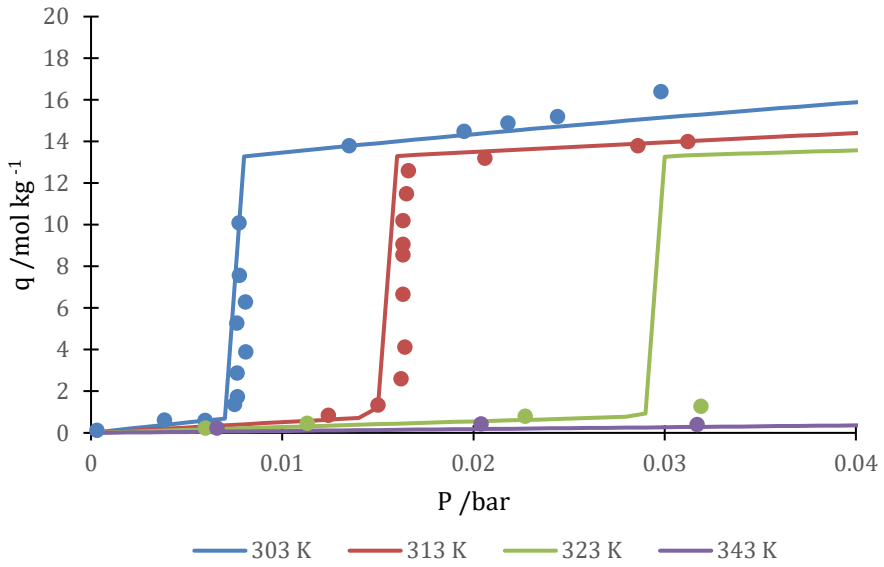

Figure A. 4. CAU-10 dataset adjustment to the Ising-Langmuir isotherm.[4]

Table A. 4. Ising-Langmuir isotherm parameters for water adsorption in CAU-10.[4]

Parameter	Value
$q_{sat\,I}$ /mol kg^{-1}	12.5
$q_{sat\,L}$ /mol kg^{-1}	20.2
$K_{\infty,I}$ /bar^{-1}	2.99×10^{-8}
$K_{\infty,o}$ /bar^{-1}	8.50×10^{-9}
$K_{\infty,L}$ /bar^{-1}	5.25×10^{-9}
$-\Delta H_I$ /kJ mol^{-1}	56.0
$-\Delta H_0$ /kJ mol^{-1}	24.0
$-\Delta H_L$ /kJ mol^{-1}	52.1

A.1. 5. Al-FUM

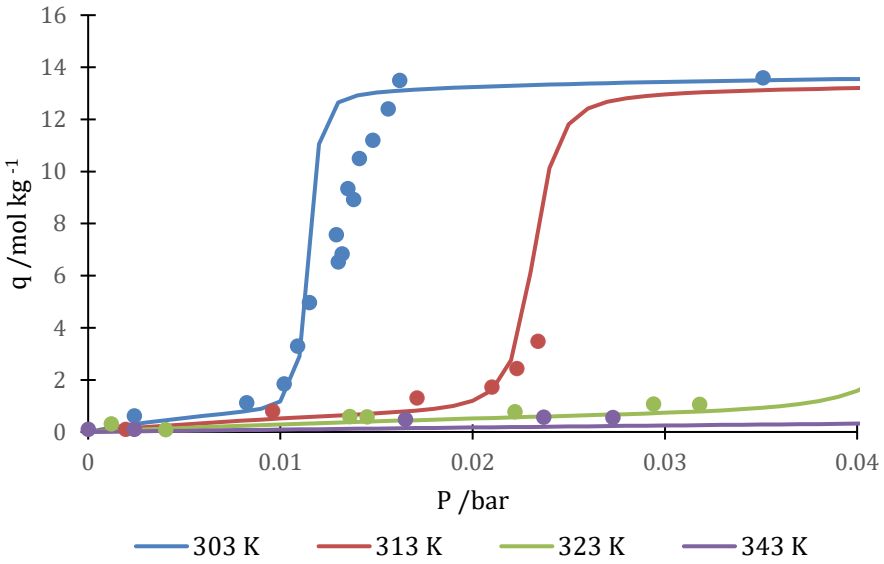

Figure A. 5. Al-FUM dataset adjustment to the Ising-Langmuir isotherm.[4]

Table A. 5. Ising-Langmuir isotherm parameters for water adsorption in Al-FUM.[4]

Parameter	Value
$q_{sat\ I}$ /mol kg^{-1}	1.95
$q_{sat\ L}$ /mol kg^{-1}	12.1
$K_{\infty,I}$ /bar^{-1}	2.45×10^{-8}
$K_{\infty,o}$ /bar^{-1}	1.54×10^{-7}
$K_{\infty,L}$ /bar^{-1}	3.92×10^{-9}
$-\Delta H_I$ /kJ mol^{-1}	55.4
$-\Delta H_0$ /kJ mol^{-1}	32.0
$-\Delta H_L$ /kJ mol^{-1}	59.1

A.1. 6. Zeolite 3A

Table A. 6. Zeolite 3A data source and suppliers.

Dataset	Supplier
1 [5]	UOP pellets
2 [6]	Alfa Aesar crystals
3 [7]	Grace Davidson silobead
4 [8]	UOP bead

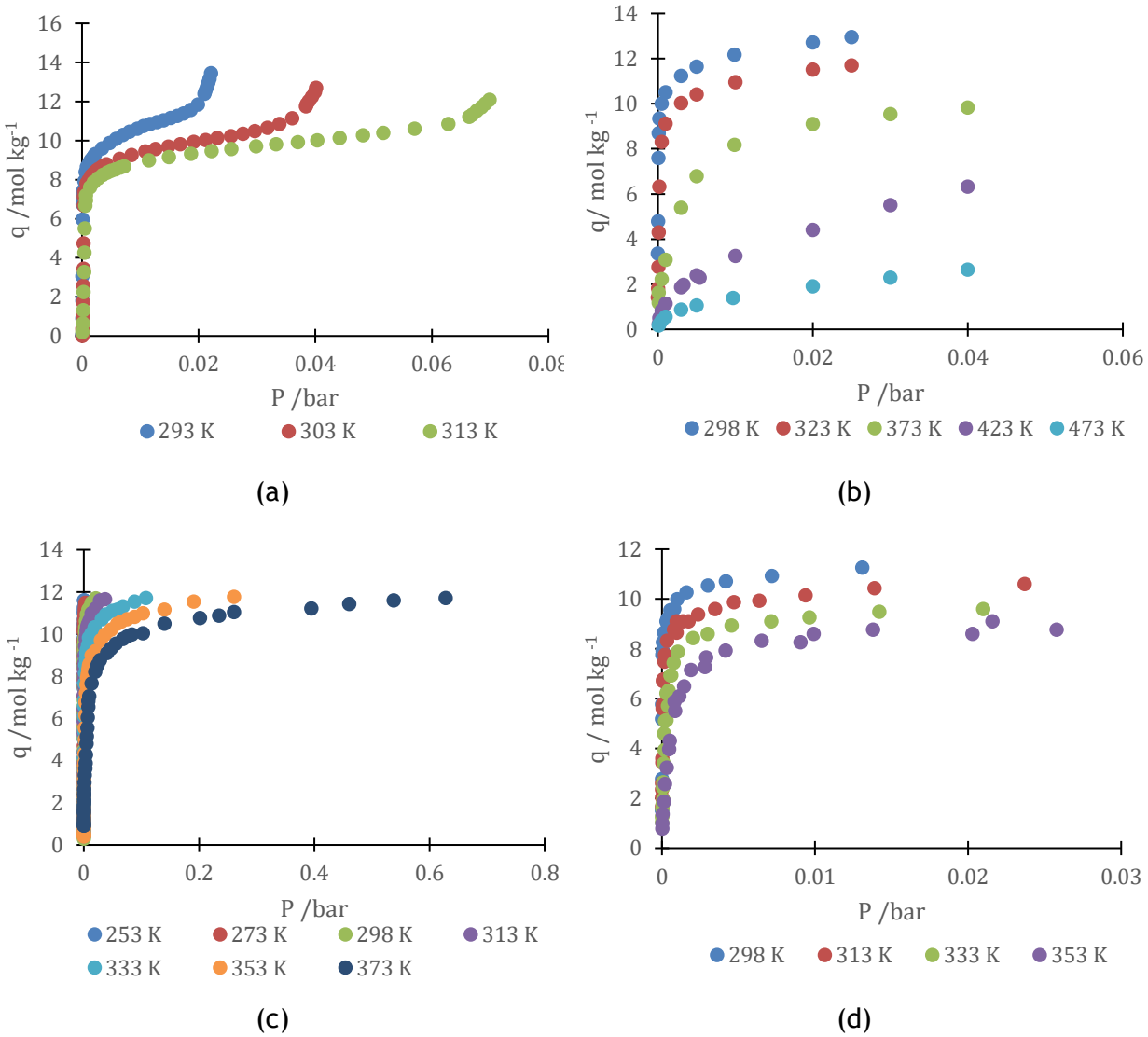

Figure A. 6. Water adsorption data for Zeolite 3A from data source 1 (a), 2 (b), 3 (c), 4 (d).

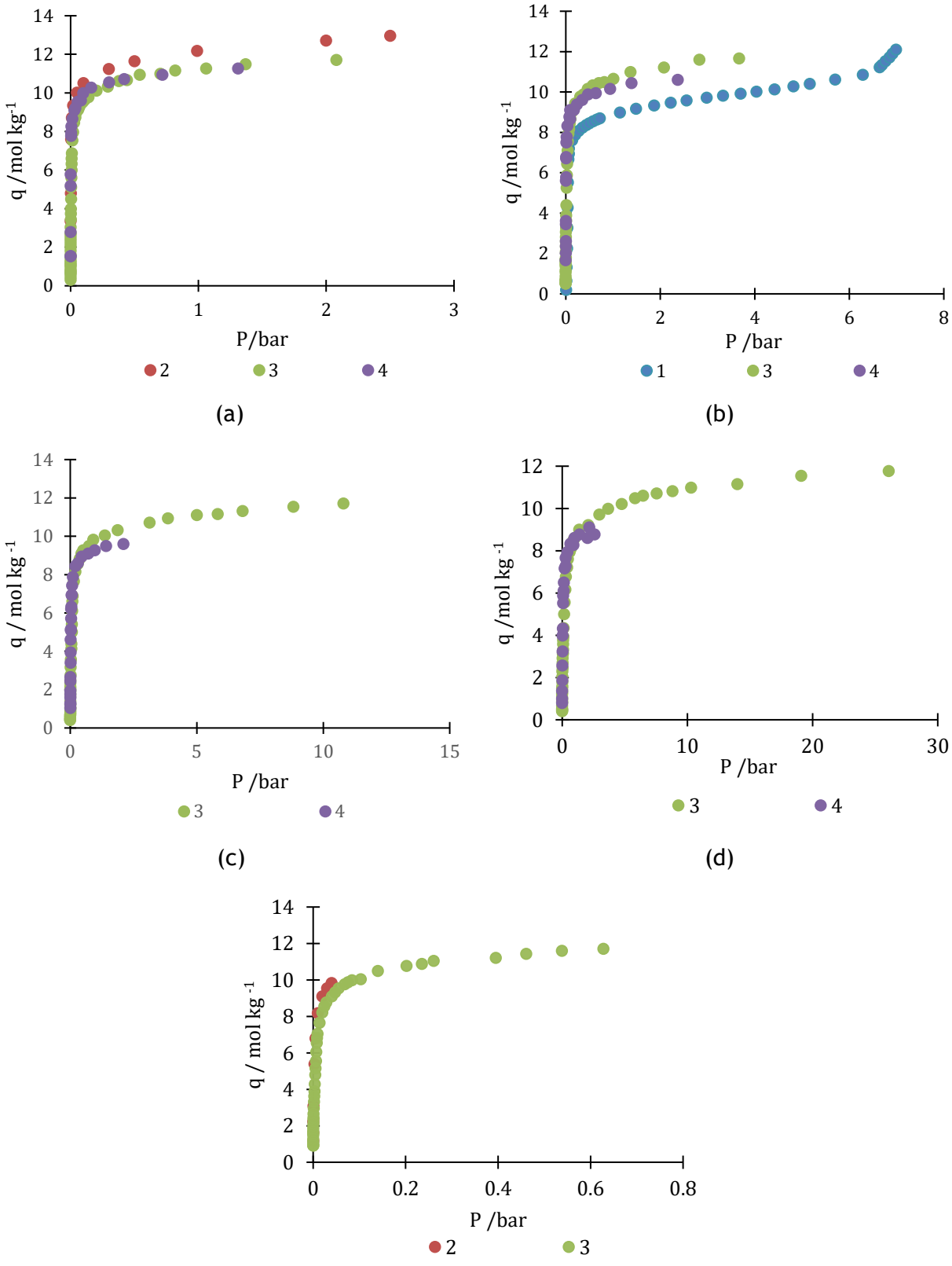

Figure A. 7. Water adsorption data comparison for Zeolite 3A at 298 K (a), 313 K (b), 333 K (c), 353 K (d), and 373 K (e).

As it can be observed from the comparison presented in Figure A.7, the data with the most agreement between the different isotherms and the points measured for a larger range of temperatures was dataset 3.

The fitting was then performed as can be seen in Figure A.8 and the resulting parameters are presented in Table A.7.

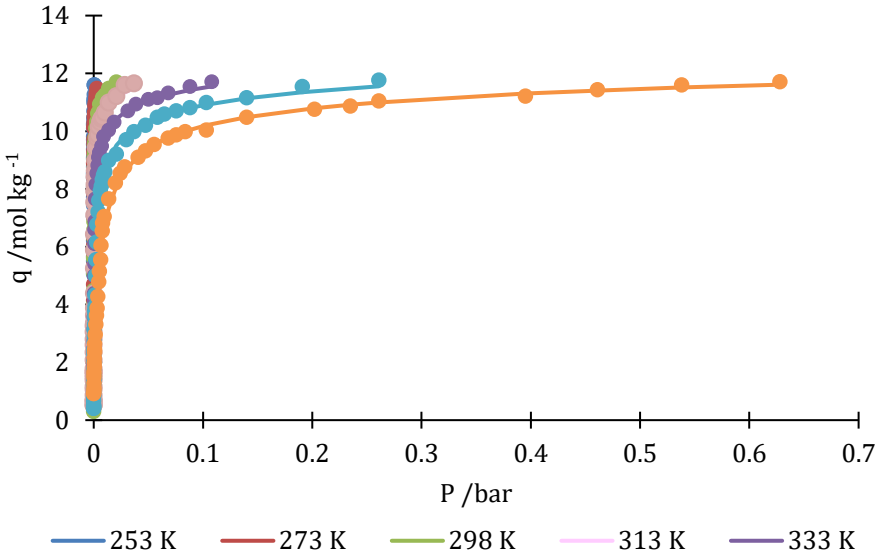

Figure A. 8. Dataset 3 adjustment to the Ising-Langmuir isotherm for Zeolite 3A.

Table A. 7. Ising-Langmuir parameters for water adsorption in Zeolite 3A.

Parameter	Value
$q_{sat\,I}$ /mol kg^{-1}	5.60
$q_{sat\,L}$ /mol kg^{-1}	7.08
$K_{\infty,I}$ /bar^{-1}	4.48 x 10^{-6}
$K_{\infty,o}$ /bar^{-1}	2.21 x 10^{-6}
$K_{\infty,L}$ /bar^{-1}	1.79 x 10^{-6}
$-\Delta H_I$ /kJ mol^{-1}	52.6
$-\Delta H_0$ /kJ mol^{-1}	64.3
$-\Delta H_L$ /kJ mol^{-1}	55.9

A.1. 7. Zeolite 4A

Table A. 8. Zeolite 4A data source and suppliers.

Dataset	Supplier
1 [6]	Sigma Aldrich crystals
2 [9]	Grace Davidson pellets
3 [10]	Linde Division of Union Carbide Corporation pellets
4 [11]	Grace Davidson silobead

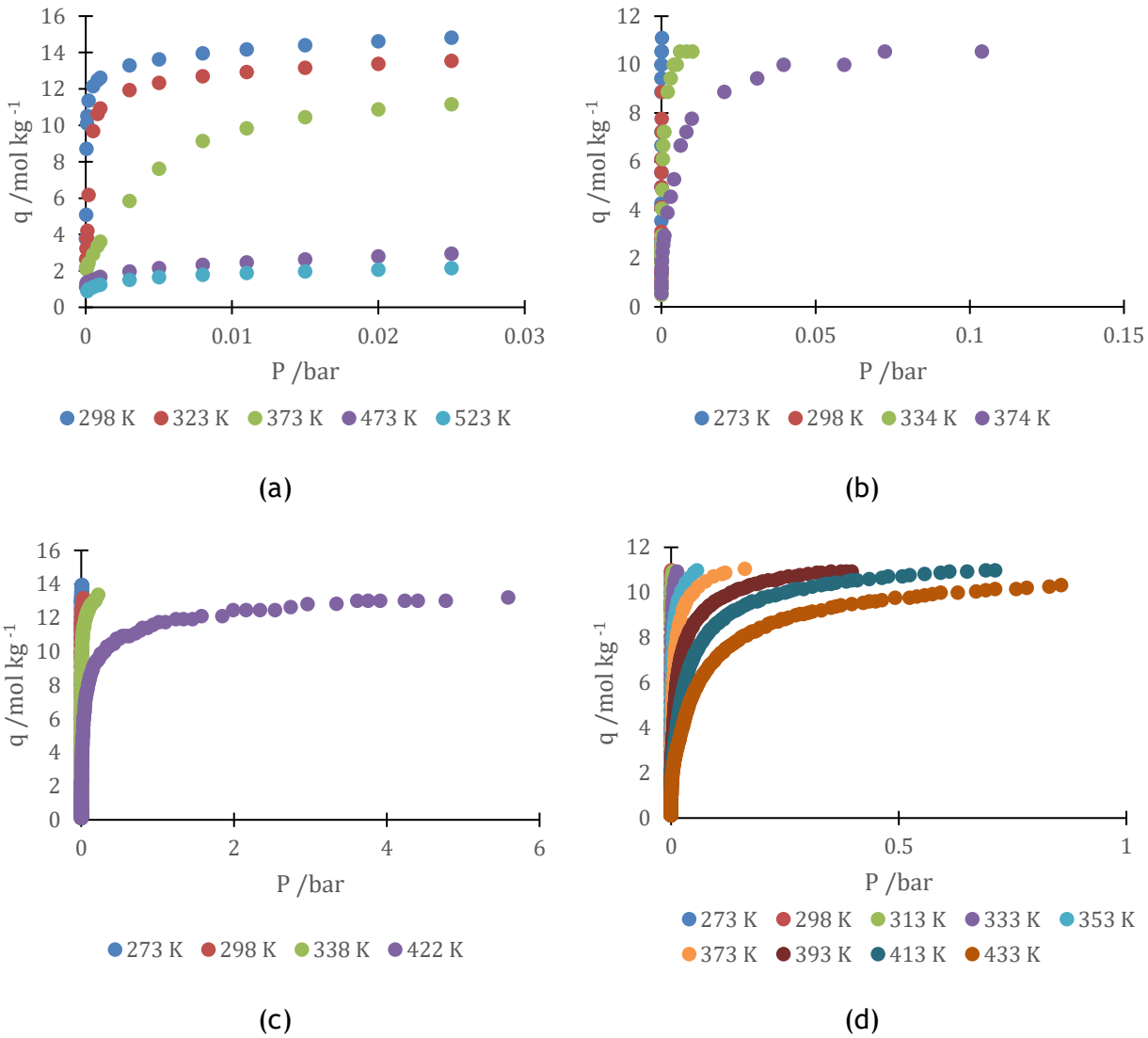

Figure A. 9. Water adsorption data for Zeolite 4A from data source 1 (a), 2 (b), 3 (c), 4 (d).

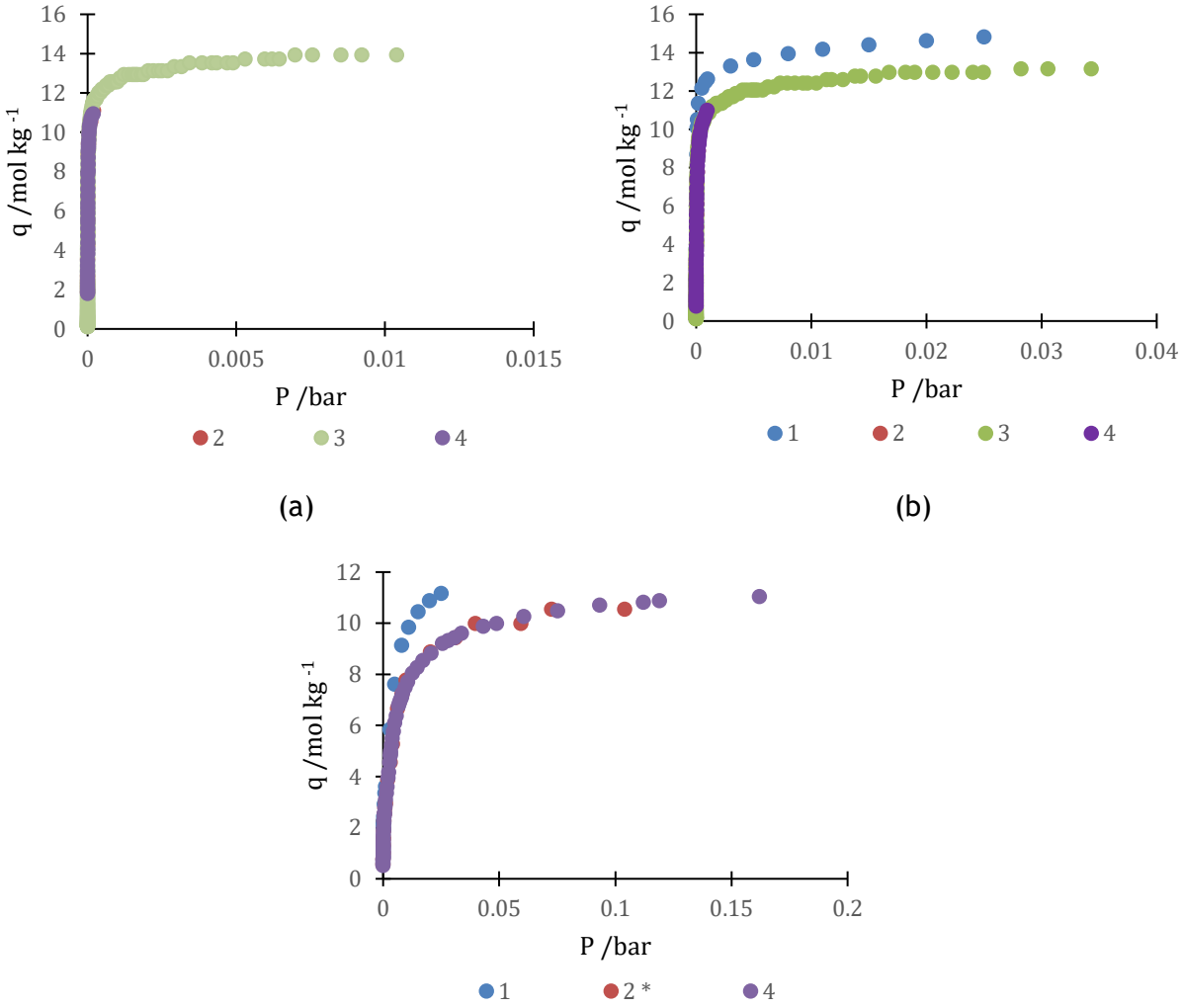

Figure A. 10. Water adsorption data comparison for Zeolite 4A at 273 K (a), 298 K (b), and 373 K (c).

*(*the dataset 2 temperature is 374 K but it was considered an approximation)*

The datasets 2, 3 and 4 presented very similar limits. The dataset 3 was the one who presented a larger pressure range and because of that was the one chosen to adjust the data. The fitting is pictured in Figure A.11. The adjustment parameters can be seen in Table A.9.

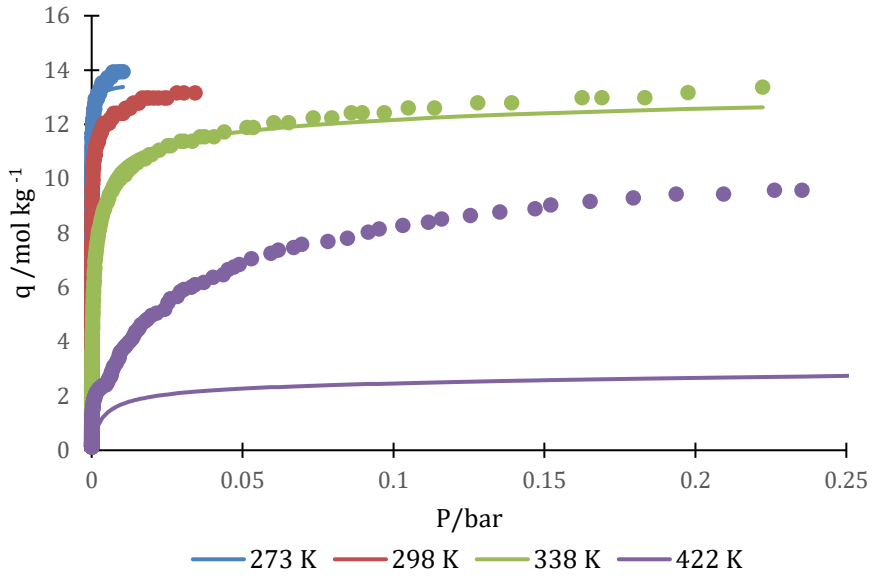

Figure A. 11. Dataset 3 adjustment to the Ising-Langmuir isotherm for Zeolite 4A.

Table A. 9. Ising-Langmuir parameters for water adsorption in Zeolite 4A.

Parameter	Value
$q_{sat\,I}$ /mol kg^{-1}	5.38
$q_{sat\,L}$ /mol kg^{-1}	8.15
$K_{\infty,I}$ /bar^{-1}	5.64 x 10^{-5}
$K_{\infty,o}$ /bar^{-1}	1.14
$K_{\infty,L}$ /bar^{-1}	3.55 x 10^{-7}
$-\Delta H_I$ /kJ mol^{-1}	48.2
$-\Delta H_0$ /kJ mol^{-1}	33.3
$-\Delta H_L$ /kJ mol^{-1}	60.8

As it can be seen, the adjustment failed to predict the data from the isotherm at 422 K. To ensure the adjustment could fit higher temperatures, the data from dataset 4 (which as shown a good concordance with the data used for the adjustment) was compared with the result of the adjusted isotherm equation.

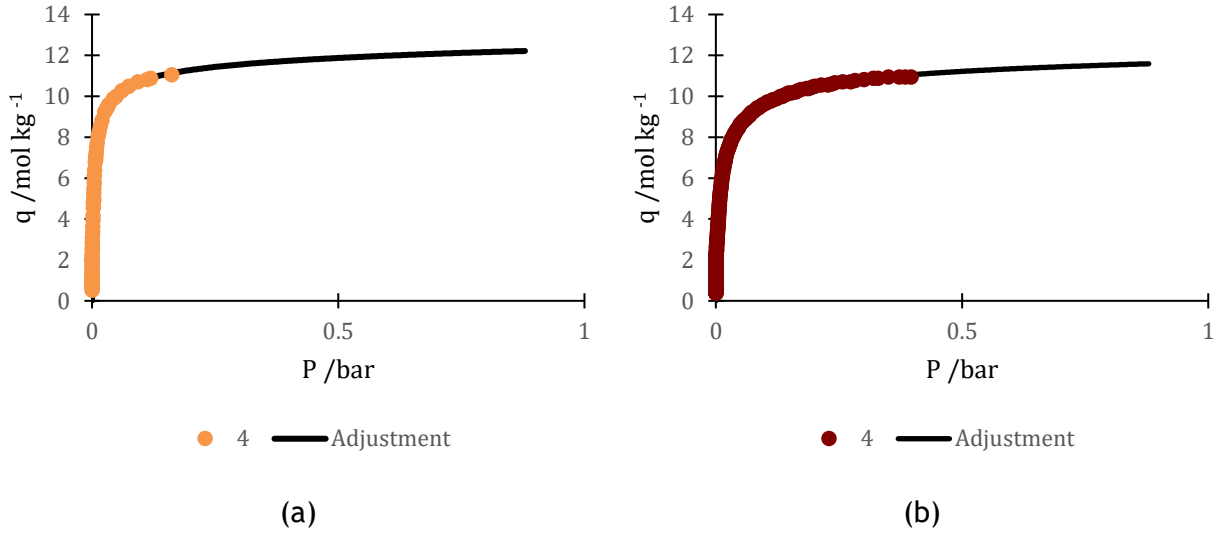

Figure A. 12. Comparison of the data in dataset 4 with the curve obtained for 373 K (a) and 393 K (b).

A.1. 8. Zeolite 5A

Table A. 10. Zeolite 5A data source and suppliers.

Dataset	Supplier
1 [12]	Grace Davidson beads
2 [11]	Linde Division of Union Carbide Corporation pellets

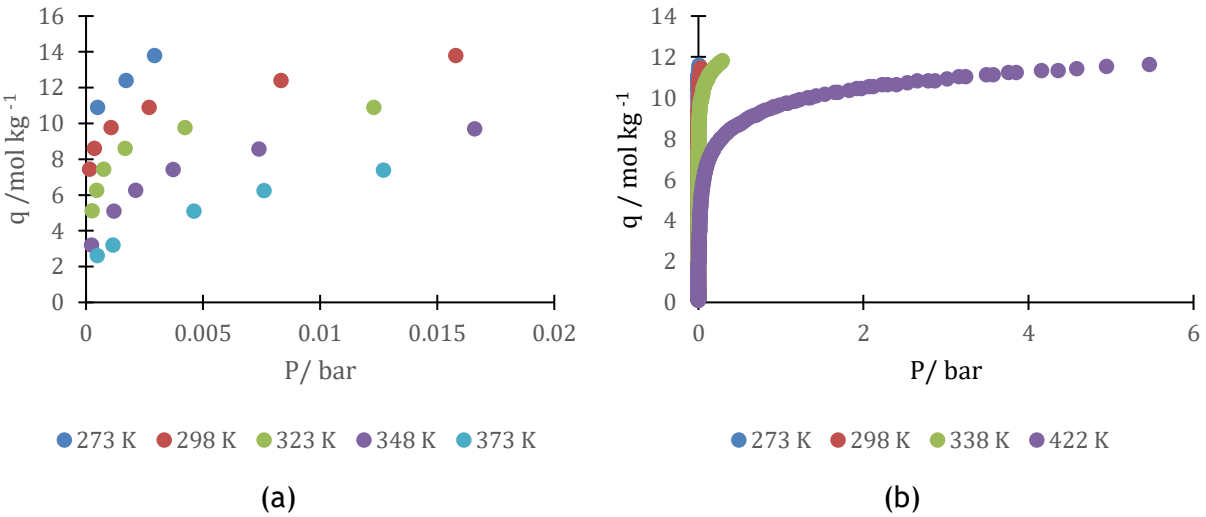

Figure A. 13. Water adsorption data for Zeolite 5A from data source 1 (a) and 2 (b).

The dataset 2 was the one that present the larger number of points withing the larger range of temperatures and pressures, so it was the one chosen to perform the adjustment. The fitting curves and parameters can be observed in Figure A.14 and Table A.11, respectively.

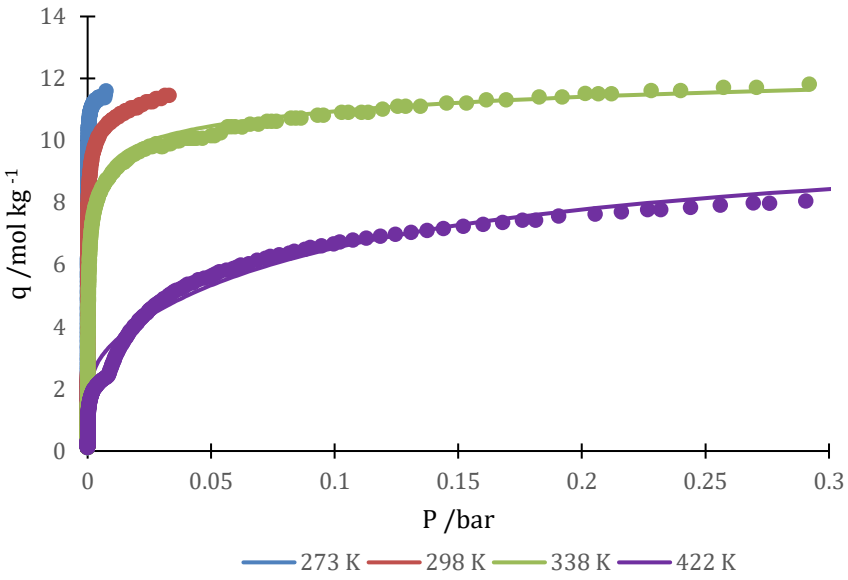

Figure A. 14. Dataset 3 adjustment to the Ising-Langmuir isotherm for Zeolite 5A.

Table A. 11. Ising-Langmuir parameters for water adsorption in Zeolite 5A.

Parameter	Value
$q_{sat\,I}$ /mol kg^{-1}	5.19
$q_{sat\,L}$ /mol kg^{-1}	6.22
$K_{\infty,I}$ /bar^{-1}	1.47 x 10^{-5}
$K_{\infty,o}$ /bar^{-1}	1.39 x 10^{-2}
$K_{\infty,L}$ /bar^{-1}	1.01 x 10^{-6}
$-\Delta H_I$ /kJ mol^{-1}	53.6
$-\Delta H_0$ /kJ mol^{-1}	47.0
$-\Delta H_L$ /kJ mol^{-1}	59.4

A.1. 9. Zeolite 13 X

Table A. 12. Zeolite 13X data source and suppliers.

Dataset	Supplier
1 [5]	UOP beads
2 [12]	Grace Davidson beads
3 [13]	Aldrich Co
4 [14]	Grace Davidson pellets

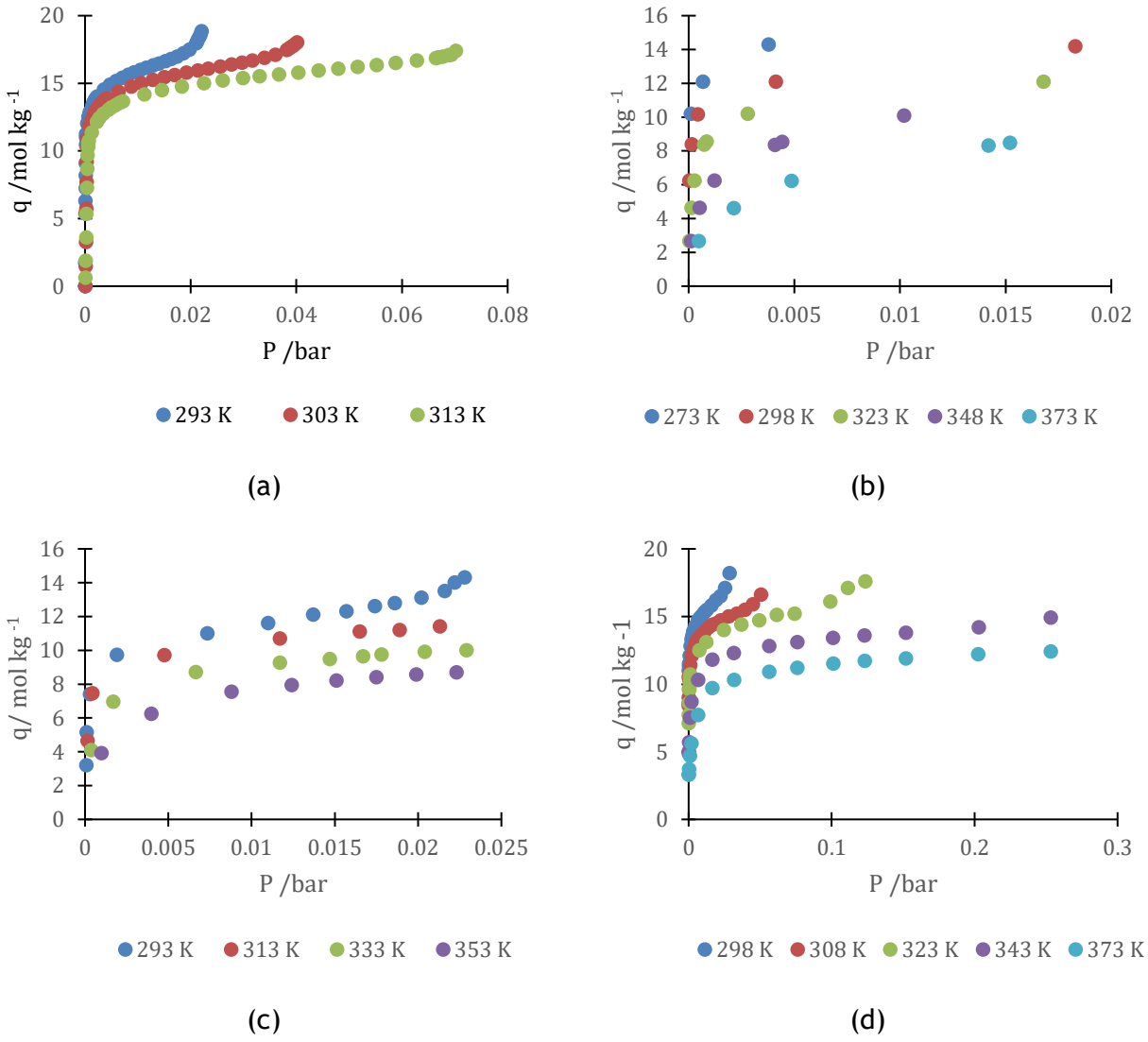

Figure A. 15. Water adsorption data for Zeolite 13X from data source 1 (a), 2 (b), 3 (c), 4 (d).

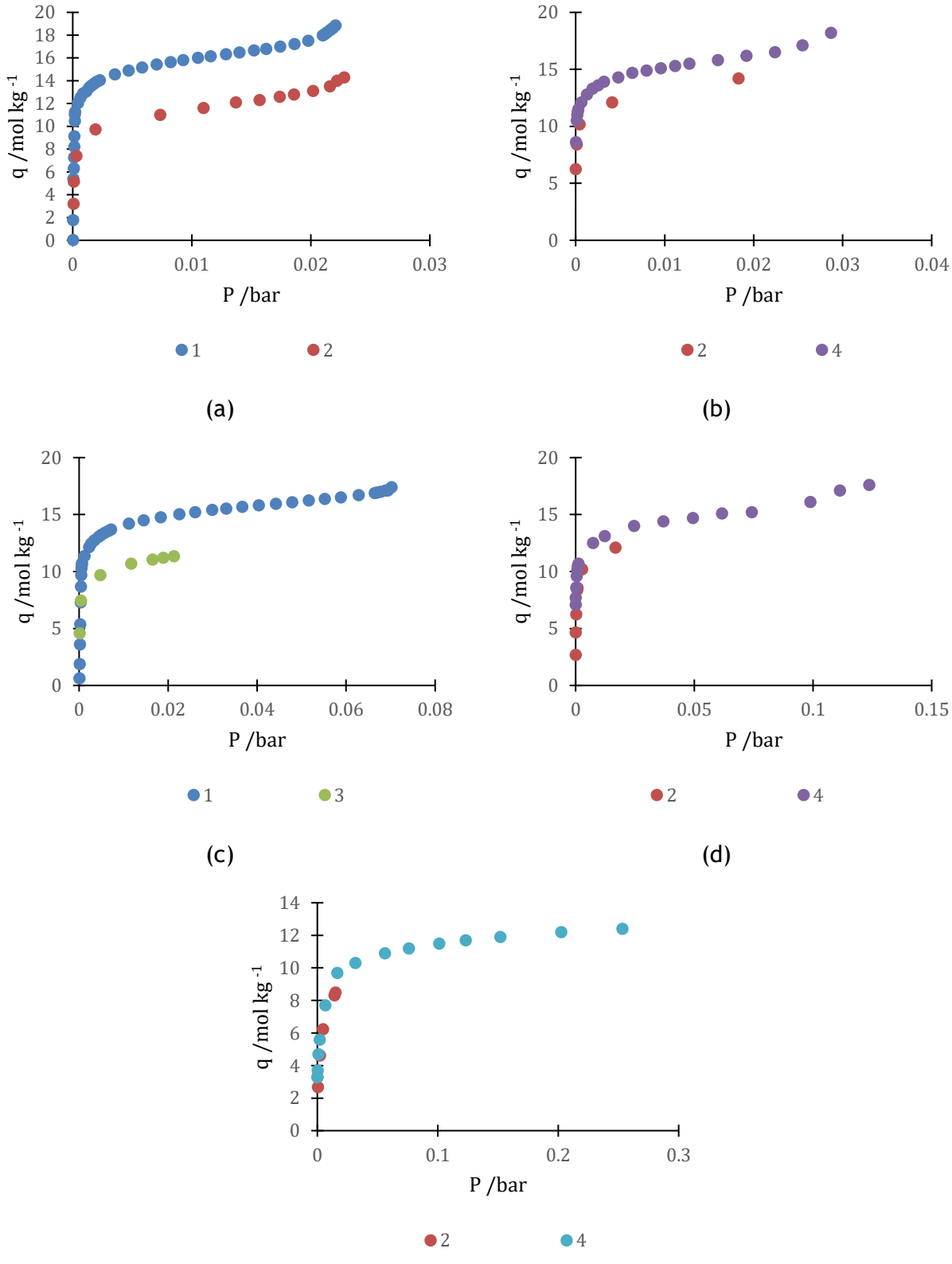

Figure A. 16. Water adsorption data comparison for Zeolite 13X at 293 K (a), 298 K (b), 313 K (c), 323 K (d) and 373 K (e).

The dataset chosen was the dataset 4 since it presented the points for the larger range of pressure and temperatures. The fitting is presented by the lines in Figure A.17. The fitting in

is also depicted with the pressures on the logarithmic scale so the quality of fitting can be perceived. Despite the optimization could not find any viable particle for Zeolite 13X, the fitting of the isotherms is quite accurate with the points presented in the literature. The fitting parameters are presented in Table A.13.

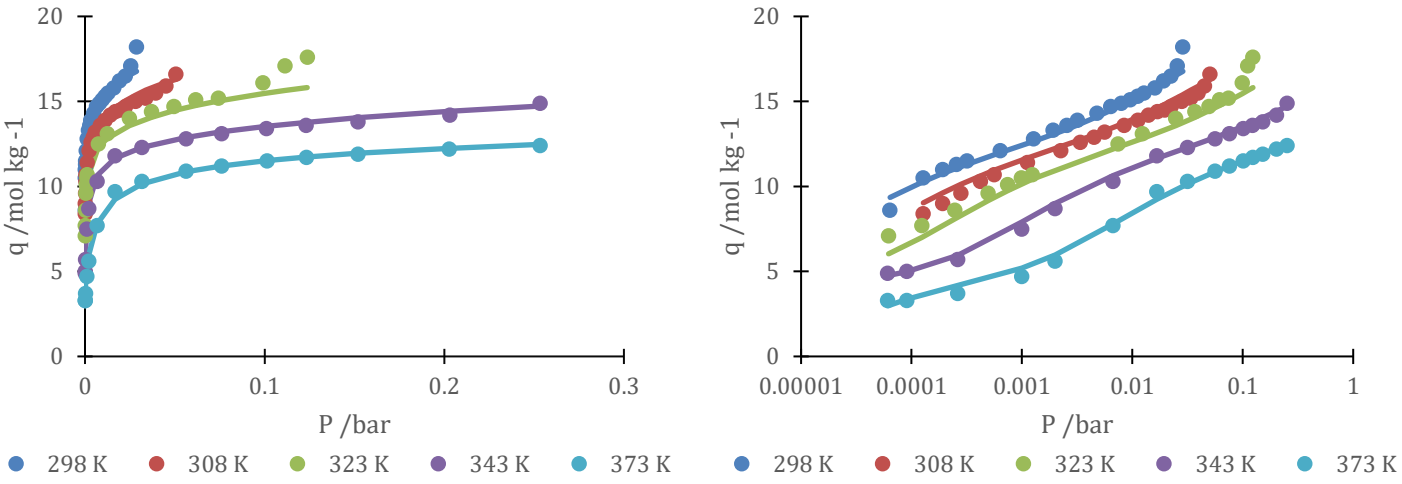

(a) (b)

Figure A. 17. Dataset 4 adjustment to the Ising-Langmuir isotherm in linear scale (a) and logarithmic scale (b) for Zeolite 13X.

Table A. 13. Ising-Langmuir parameters for water adsorption in Zeolite 13 X.

Parameter	Value
$q_{sat\ I}$ /mol kg^{-1}	15.65
$q_{sat\ L}$ /mol kg^{-1}	4.30
$K_{\infty,I}$ /bar^{-1}	1.81 x 10^{-9}
$K_{\infty,o}$ /bar^{-1}	1.38 x 10^{-8}
$K_{\infty,L}$ /bar^{-1}	8.14 x 10^{-16}
$-\Delta H_I$ /kJ mol^{-1}	67.7
$-\Delta H_0$ /kJ mol^{-1}	69.7
$-\Delta H_L$ /kJ mol^{-1}	140.0

A.1. 10. AQSOA FAM-Z02

Table A. 14. AQSOA FAM-Z02 data source and suppliers.

Dataset	Supplier
1 [15]	Not specified
2 [16]	Not specified
3 [17]	Manufactured during the research
4 [18]	Mitsubishi Plastic Inc.

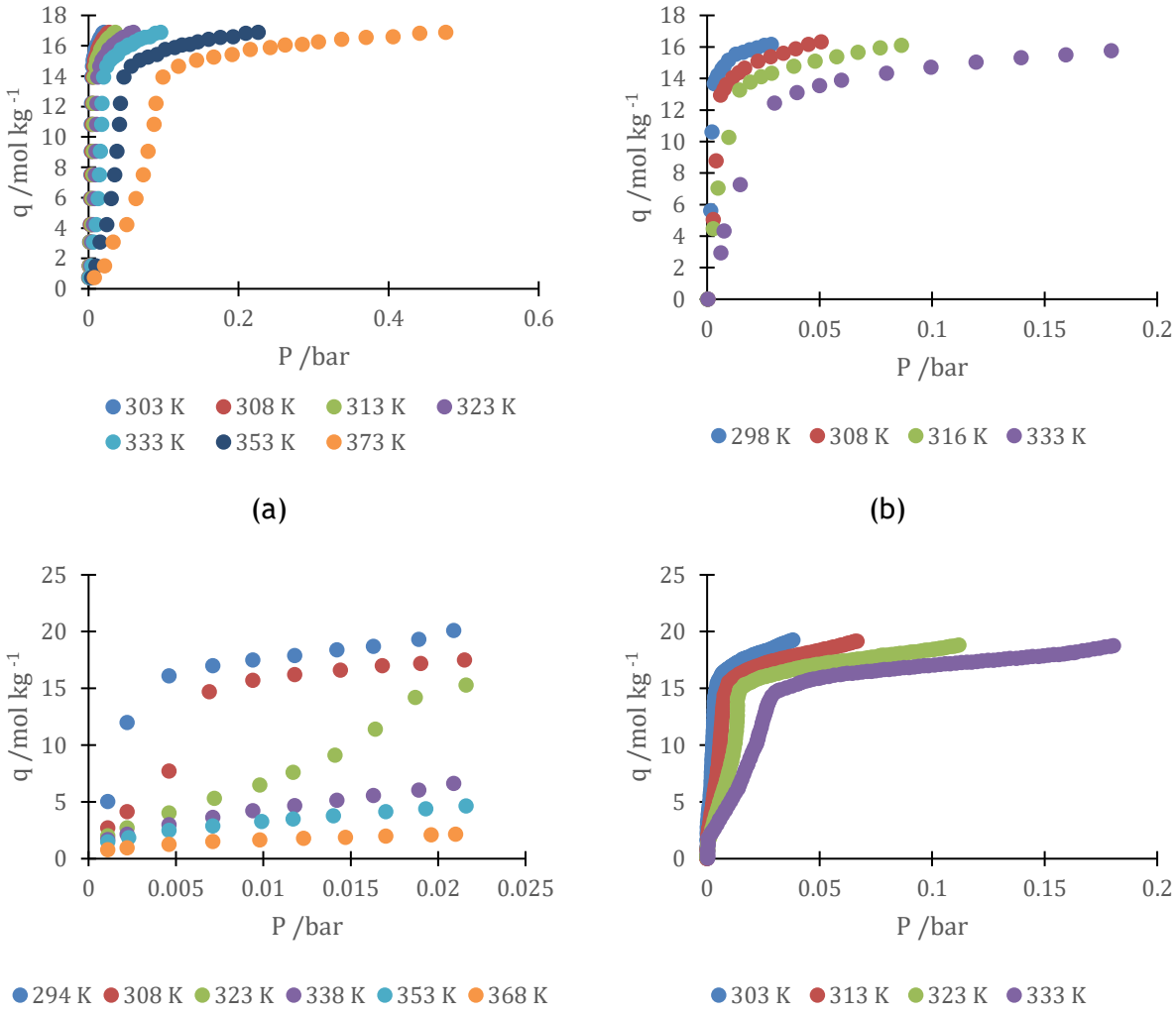

Figure A. 18. Water adsorption data for AQSOA FAM-Z02 from data source 1 (a), 2 (b), 3 (c), 4 (d).

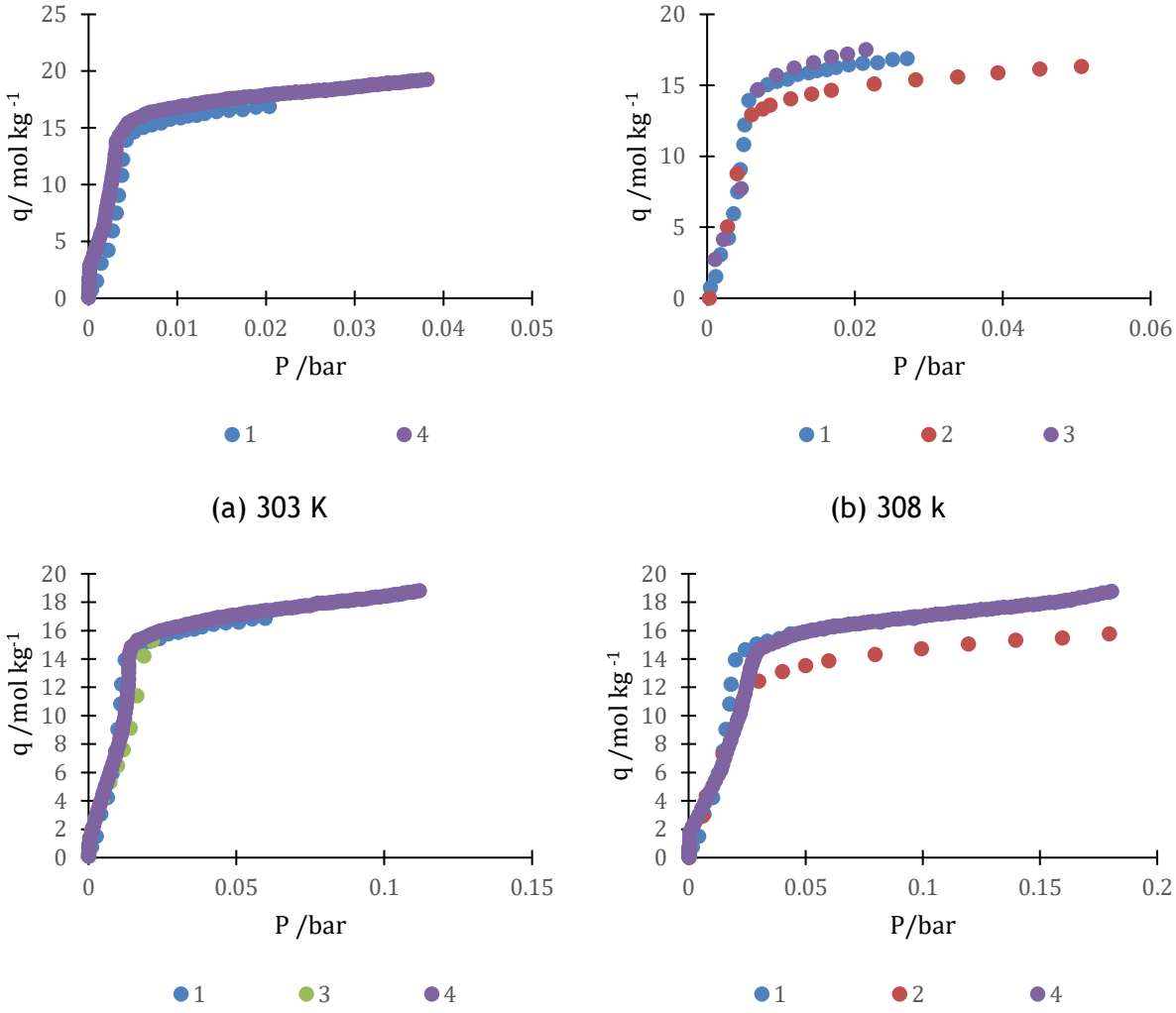

Figure A. 19. Water adsorption data comparison for AQSOA FAM-Z02 at 303 K (a), 308 K (b), 323 K (c), and 333 K (d).

Datasets 1, 3 and 4 are mostly overlapped in the above plots. The dataset chosen for the fitting was the dataset 4. The fitting is pictured in Figure A. 20 and the fitting parameters are presented in Table A. 15.

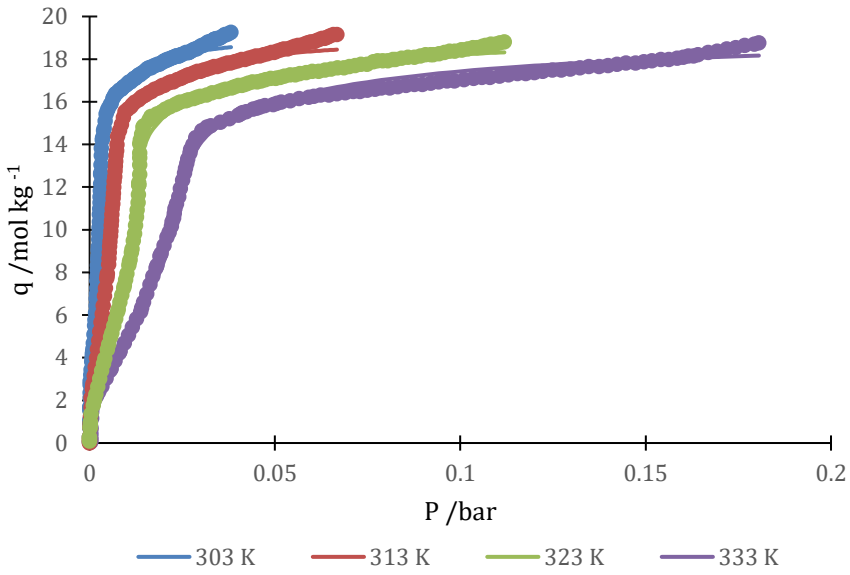

Figure A. 20. Dataset 4 adjustment to the Ising-Langmuir isotherm for AQSOA FAM-Z02.

Table A. 15. Ising-Langmuir parameters for water adsorption in AQSOA FAM-Z02.

Parameter	Value
$q_{sat\,I}$ /mol kg^{-1}	6.11
$q_{sat\,L}$ /mol kg^{-1}	13.11
$K_{\infty,I}$ /bar^{-1}	3.05 x 10^{-8}
$K_{\infty,o}$ /bar^{-1}	0.41
$K_{\infty,L}$ /bar^{-1}	6.92 x 10^{-8}
$-\Delta H_I$ /kJ mol^{-1}	58.3
$-\Delta H_0$ /kJ mol^{-1}	0
$-\Delta H_L$ /kJ mol^{-1}	57.2

A. 2. Isosteric heat of adsorption

The isosteric heat of adsorption was calculated for certain values of q according to the Clausius-Clapeyron equation.

After obtaining those points, a polynomial adjustment was made for one or more branches of the function that would describe the obtained values. Equation A.1 describes the polynomial adjustment made.

$$(-\Delta H_{ads}) = a_6\ q^6 + a_5\ q^5 + a_4\ q^4 + a_3\ q^3 + a_2\ q^2 + a_1\ q + a_0 \quad \text{(A.1)}$$

With $(-\Delta H_{ads})$ in J mol^{-1}, q in mol kg^{-1} and a_6, a_5,a_4, a_3, a_2, a_1 and a_0 being the polynomial coefficients in the corresponding units.

In the following subsections, the plots of the isosteric heat of adsorption vs. the amount of water adsorbed are presented, as well as the values of the coefficients for the polynomial adjustment in each branch. In the points where no data was collected, the value was considered constant and equal to the isosteric heat of adsorption of the nearest point collected.

A. 2.1.MIL-100 (Fe)

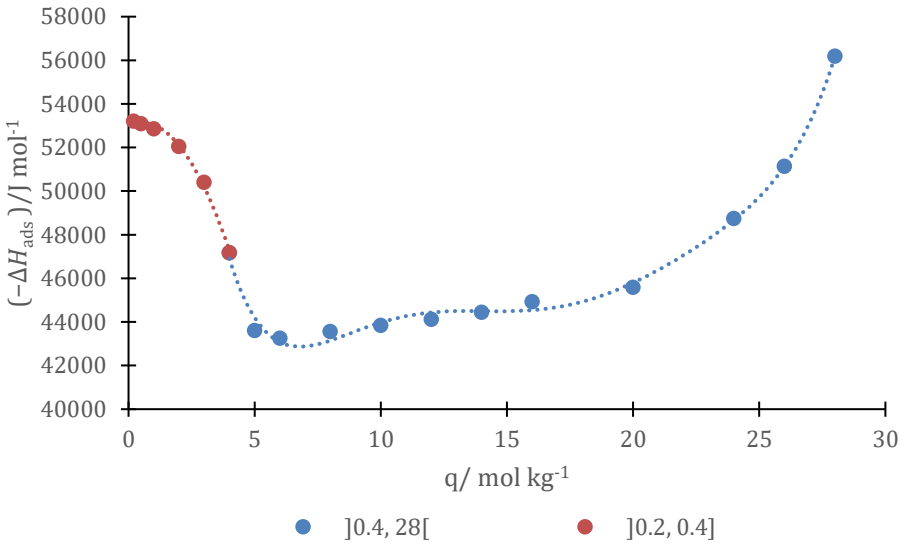

Figure A. 21. Adjustment of isosteric heat of adsorption in function of the adsorbed amount for MIL-100 (Fe).

Table A. 16. Parameters of the polynomial adjustment of isosteric heat of adsorption for MIL-100 (Fe).

q/mol kg^{-1}	a_6	a_5	a_4	a_3	a_2	a_1	a_0
[0,0.2]							53 202
]0.2,0.4]					-493.90	549.00	52 975
]0.4, 28[	5.02 x 10^{-3}	- 0.51	20.53	-423.36	4 635	-25 162	95 723
[28, ∞[							56 179

A. 2.2.MIL-125 _NH_2 (Ti)

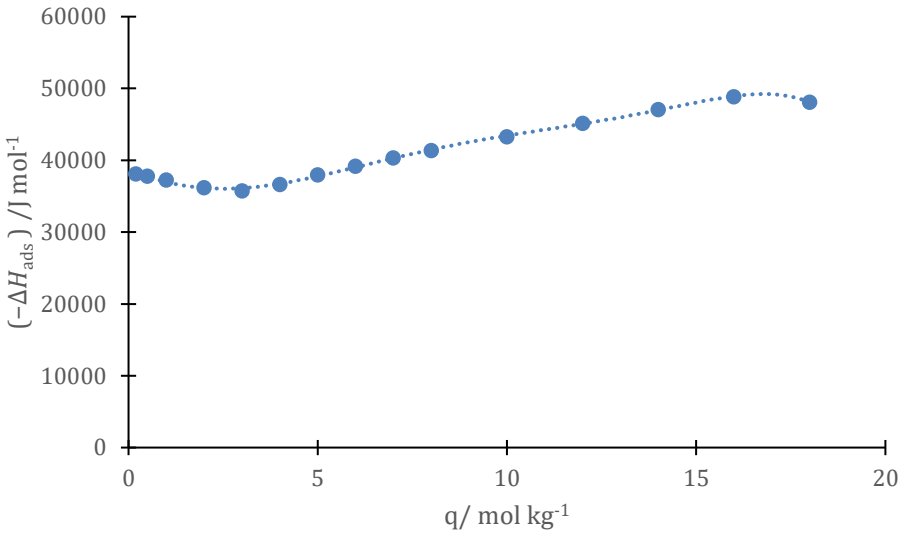

Figure A. 22. Adjustment of isosteric heat of adsorption in function of the adsorbed amount for MIL-125_NH_2 (Ti).

Table A. 17. Parameters of the polynomial adjustment of isosteric heat of adsorption for MIL-125_NH_2 (Ti).

q/mol kg^{-1}	a_6	a_5	a_4	a_3	a_2	a_1	a_0
[0,0.2]							38 114
]0.2,18[	-1.37 x10^{-2}	0.61	-8.40	18.24	459.72	-2 231	38 736
[18, ∞[							48 100

A. 2.3.MIL-160 (Al)

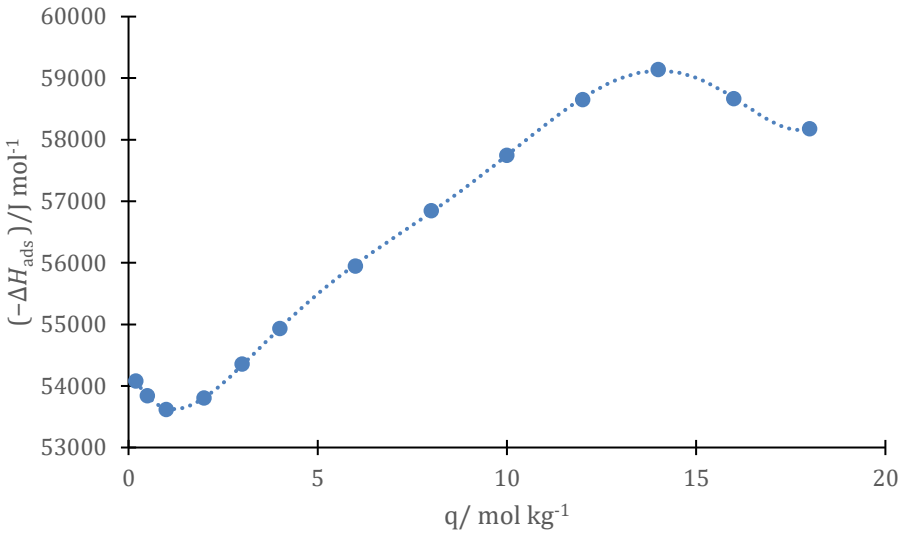

Figure A. 23. Adjustment of isosteric heat of adsorption in function of the adsorbed amount for MIL-160 (Al).

Table A. 18. Parameters of the polynomial adjustment of isosteric heat of adsorption for MIL-160 (Al).

q/mol kg^{-1}	a_6	a_5	a_4	a_3	a_2	a_1	a_0
[0,0.2]							54 083
]0.2,18[	1.31 x10^{-2}	-0.73	15.49	-158.46	803.58	-1 342	54 321
[18, ∞ [							58 183

A. 2.4.CAU-10

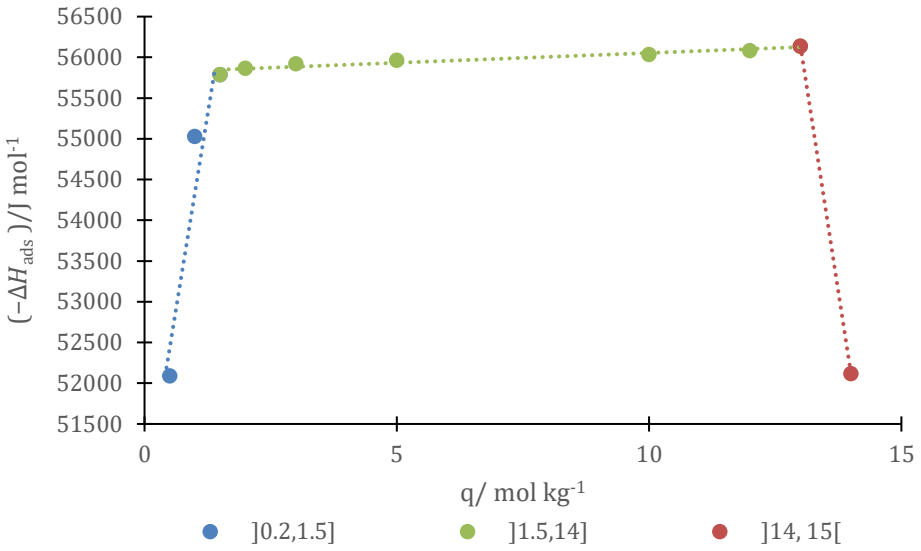

Figure A. 24. Adjustment of isosteric heat of adsorption in function of the adsorbed amount for CAU-10.

Table A. 19. Parameters of the polynomial adjustment of isosteric heat of adsorption for CAU-10.

q/mol kg^{-1}	a_6	a_5	a_4	a_3	a_2	a_1	a_0
[0,0.2]							52 096
]0.2,1.5]						3 698	50 606
]1.5,14]							55 972
]14, 15[						-4 021	108 421
[15, ∞ [							52 101

A. 2.5.Al-FUM

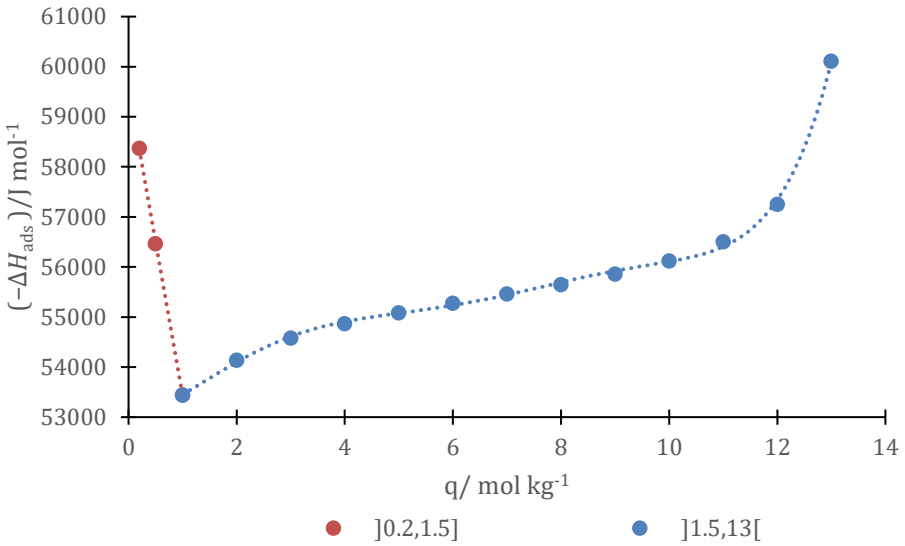

Figure A. 25. Adjustment of isosteric heat of adsorption in function of the adsorbed amount for Al-FUM.

Table A. 20. Parameters of the polynomial adjustment of isosteric heat of adsorption for Al-FUM.

q/mol kg^{-1}	a_6	a_5	a_4	a_3	a_2	a_1	a_0
[0,0.2]							58 375
]0.2,1.5]						-6 151	59 581
]1.5,13[	7.82 x 10^{-2}	-2.81	38.32	-242.85	665.21	-150.4	53 151
[13, ∞ [							60 114

A. 2.6.Zeolite 3A

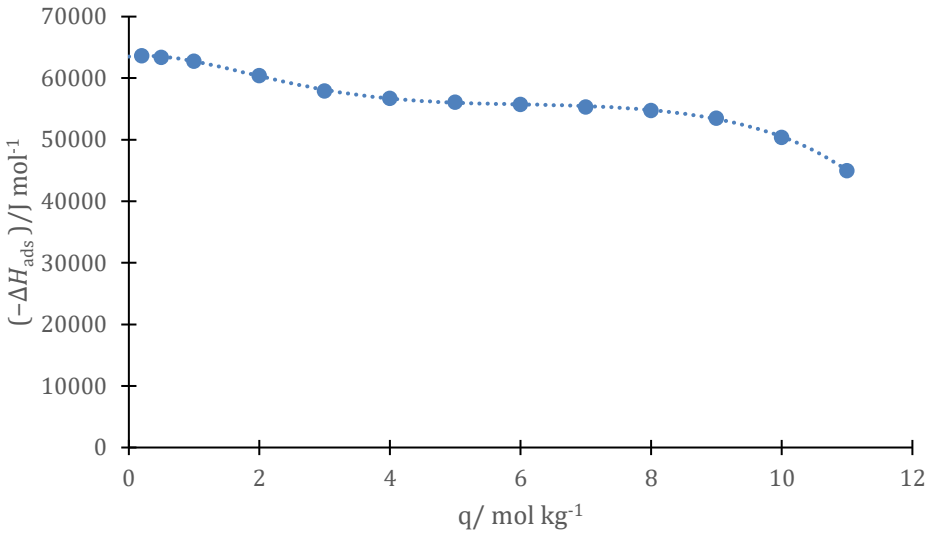

Figure A. 26. Adjustment of isosteric heat of adsorption in function of the adsorbed amount for Zeolite 3A.

Table A. 21. Parameters of the polynomial adjustment of isosteric heat of adsorption for Zeolite 3A.

q/mol kg^{-1}	a_6	a_5	a_4	a_3	a_2	a_1	a_0
[0,0.2]							63 654
]0.2,11]	-0.20	7.33	-109.91	796.34	-2 543	1 093	63 493
[11, ∞ [							45 016

A. 2.7.Zeolite 4A

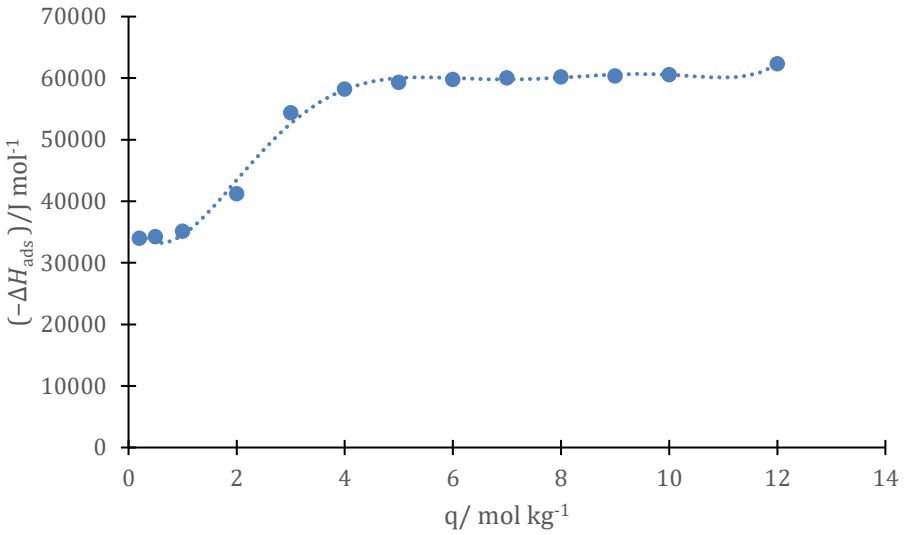

Figure A. 27. Adjustment of isosteric heat of adsorption in function of the adsorbed amount for Zeolite 4A.

Table A. 22. Parameters of the polynomial adjustment of isosteric heat of adsorption for Zeolite 4A.

q/mol kg^{-1}	a_6	a_5	a_4	a_3	a_2	a_1	a_0
[0,0.2]							34 006
]0.2,12]	1.04	-41.9	650.5	-4 806	16 178	-14 528	37 087
[12, ∞ [							62 372

A. 2.8.Zeolite 5A

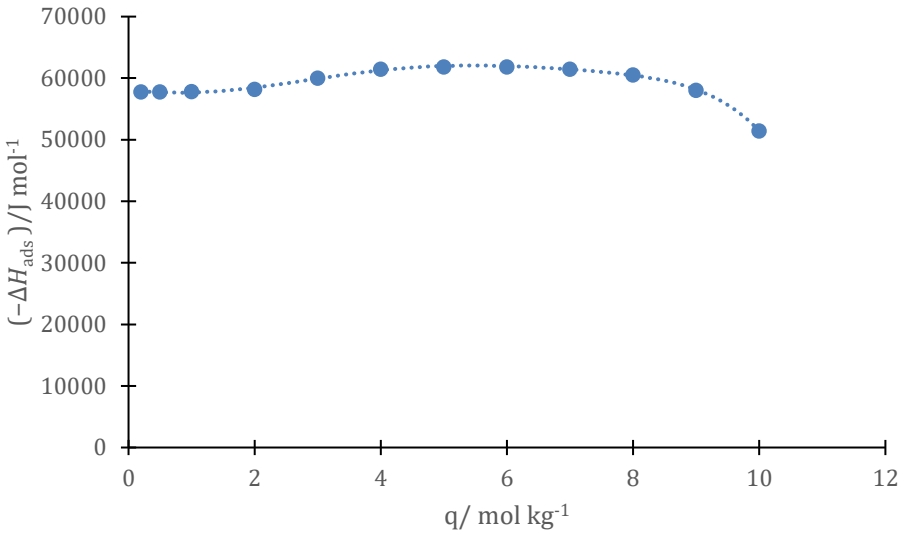

Figure A. 28. Adjustment of isosteric heat of adsorption in function of the adsorbed amount for Zeolite 5A.

Table A. 23. Parameters of the polynomial adjustment of isosteric heat of adsorption for Zeolite 5A.

q/mol kg^{-1}	a_6	a_5	a_4	a_3	a_2	a_1	a_0
[0,0.2]							57 779
]0.2,10]	-0.47	11.69	-99.27	269.51	289.87	-812.36	58 018
[10, ∞ [							51 465

A. 2.9.Zeolite 13 X

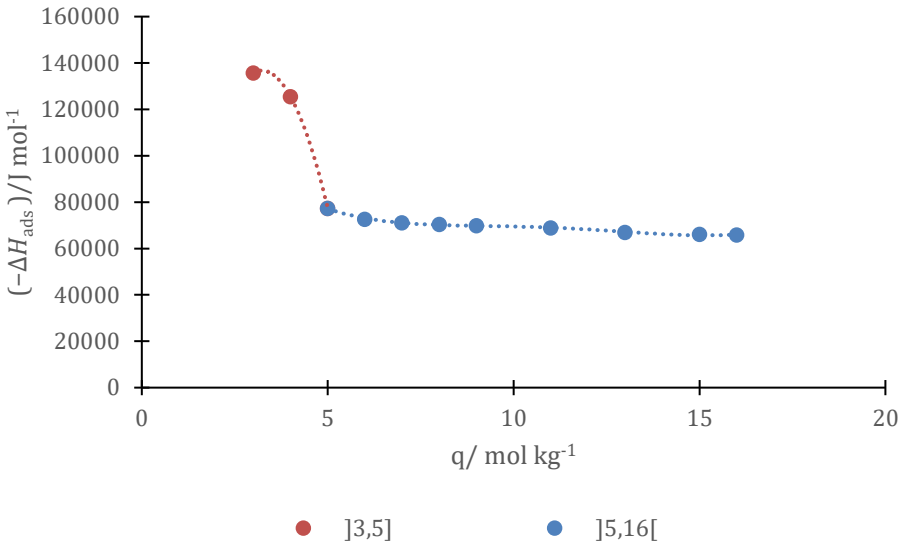

Figure A. 29.Adjustment of isosteric heat of adsorption in function of the adsorbed amount for Zeolite 13X.

Table A. 24. Parameters of the polynomial adjustment of isosteric heat of adsorption for Zeolite 13X.

q/mol kg^{-1}	a_6	a_5	a_4	a_3	a_2	a_1	a_0
[0,3]							135 715
]3,5]					-18 965	122 552	-61 251
]5,16[			7.21	-320.07	5 172	-36 622	166 438
[16, ∞ [							65 941

A. 2.10. AQSOA FAM-Z02

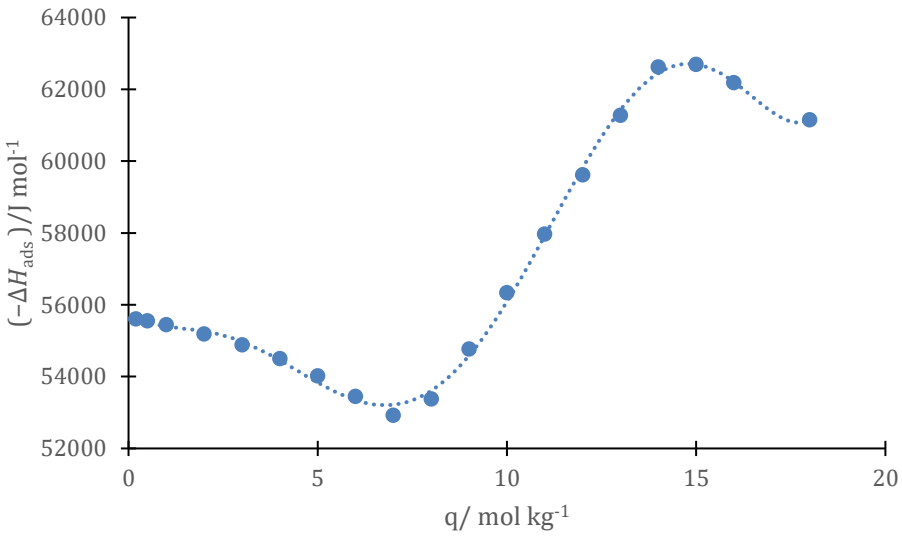

Figure A. 30. Adjustment of isosteric heat of adsorption in function of the adsorbed amount for AQSOA FAM-Z02.

Table A. 25. Parameters of the polynomial adjustment of isosteric heat of adsorption for AQSOA FAM-Z02.

q/mol kg^{-1}	a_6	a_5	a_4	a_3	a_2	a_1	a_0
[0,0.2]							55 612
]0.2,18]	3.2 x 10^{-2}	-1.59	27.88	-198.29	547.15	-757.52	55 778
[18, ∞ [							61 155

A. 3. Specific heat capacity of adsorbents

Table A. 26. Specific heat capacity of adsorbents.

Material	Value or function /J kg^{-1} K^{-1}	Temperature range /K
MIL-100(Fe) [19]	990	-
MIL-125_NH_2 (Ti) [20]	890	]0, 308]
	$4.46\,T - 484.15$	]308, 373[
	1 180	[373, ∞[
MIL-160(Al) [21]	1 117	]0, 297.8]
	$0.97\,T + 824.36$	]297.8, 343[
	1 160	[343, ∞[
CAU-10 [22]	1 300	]0, 298]
	$6.87\,T - 780.58$	]298, 352.9]
	$-10\,T + 5179$	]352.9, 362.9]
	$2.42\,T + 656.27$	]362.9, 423[
	1 700	[423, ∞[
Al-FUM [23]	1 050	]0, 323]
	$1\,262 + 3\,(T - 273) + \frac{17\,379}{(T - 273)^2}$	]323, 418[
	1 350	[418, ∞[
Zeolite 3A [24]	1045	-
Zeolite 4A [9]	920	-
Zeolite 5A [25]	921.1	-
Zeolite 13X [26]	1004.46	]0, 313.61]
	$1097.44 + 3.44\,(T - 373) - 0.0029\,(T^2 - 373^2)$	]313.61, 452.14[
	1185.55	[452.14, ∞]
AQSOA Z02-FAM [27]	822	]0, 303]
	$2\,T + 216$	]303, 363[
	942	[363, ∞[

Appendix B. Particle distribution evaluation

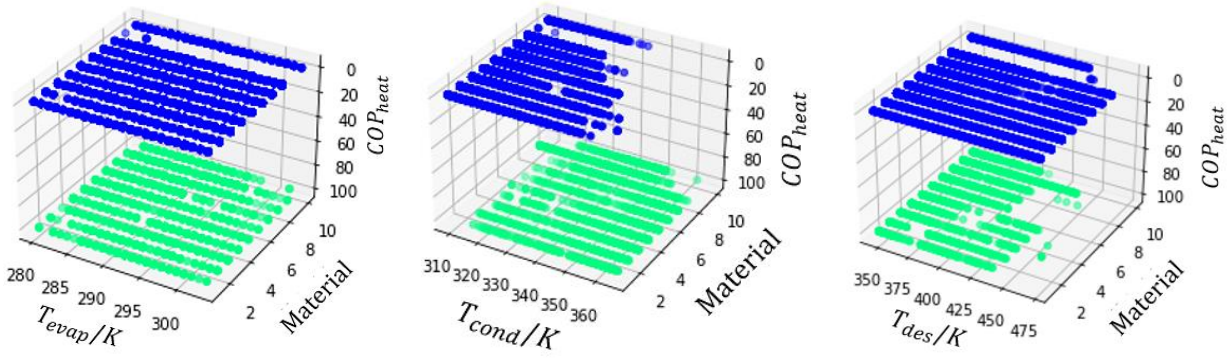

(a)

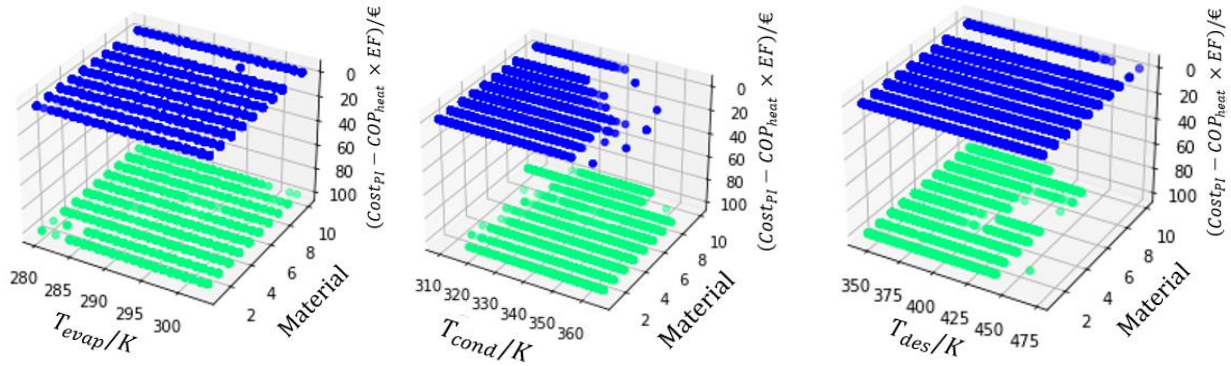

(b)

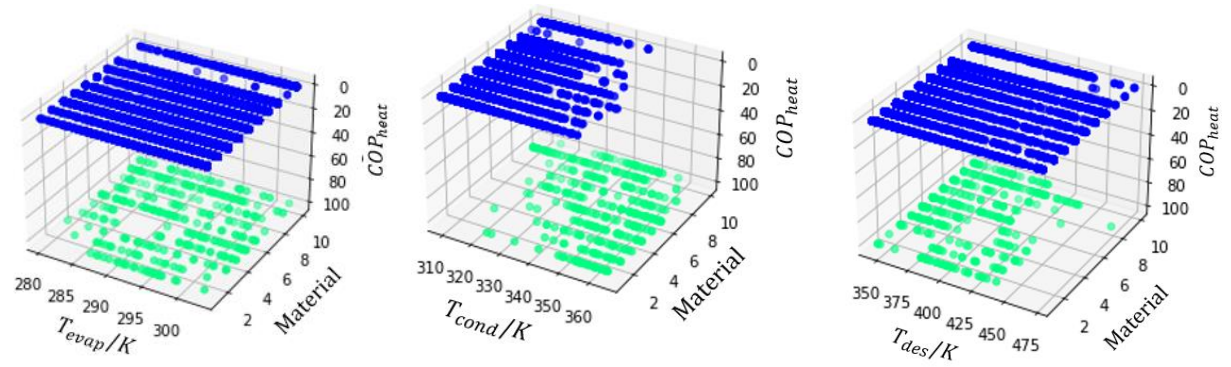

(c)

Figure B. 1. Particle distribution during the PSO implementation in maximization of COP_{heat} (a), minimization of $(Cost_{PI} - COP_{heat} \times EF)$ (b), and multi-objective problem (c).

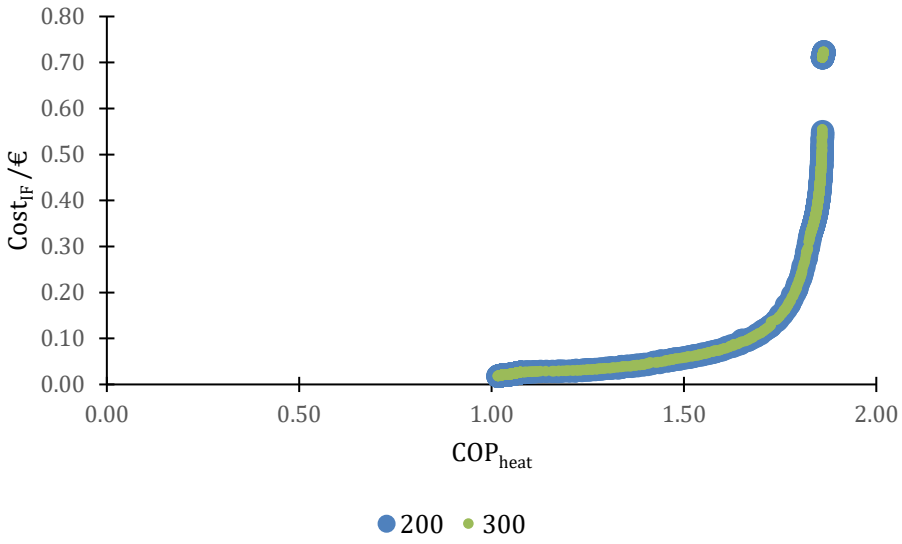

Figure B. 2. Pareto Front for different N_{it_max}.

Appendix C. Mapping the temperatures

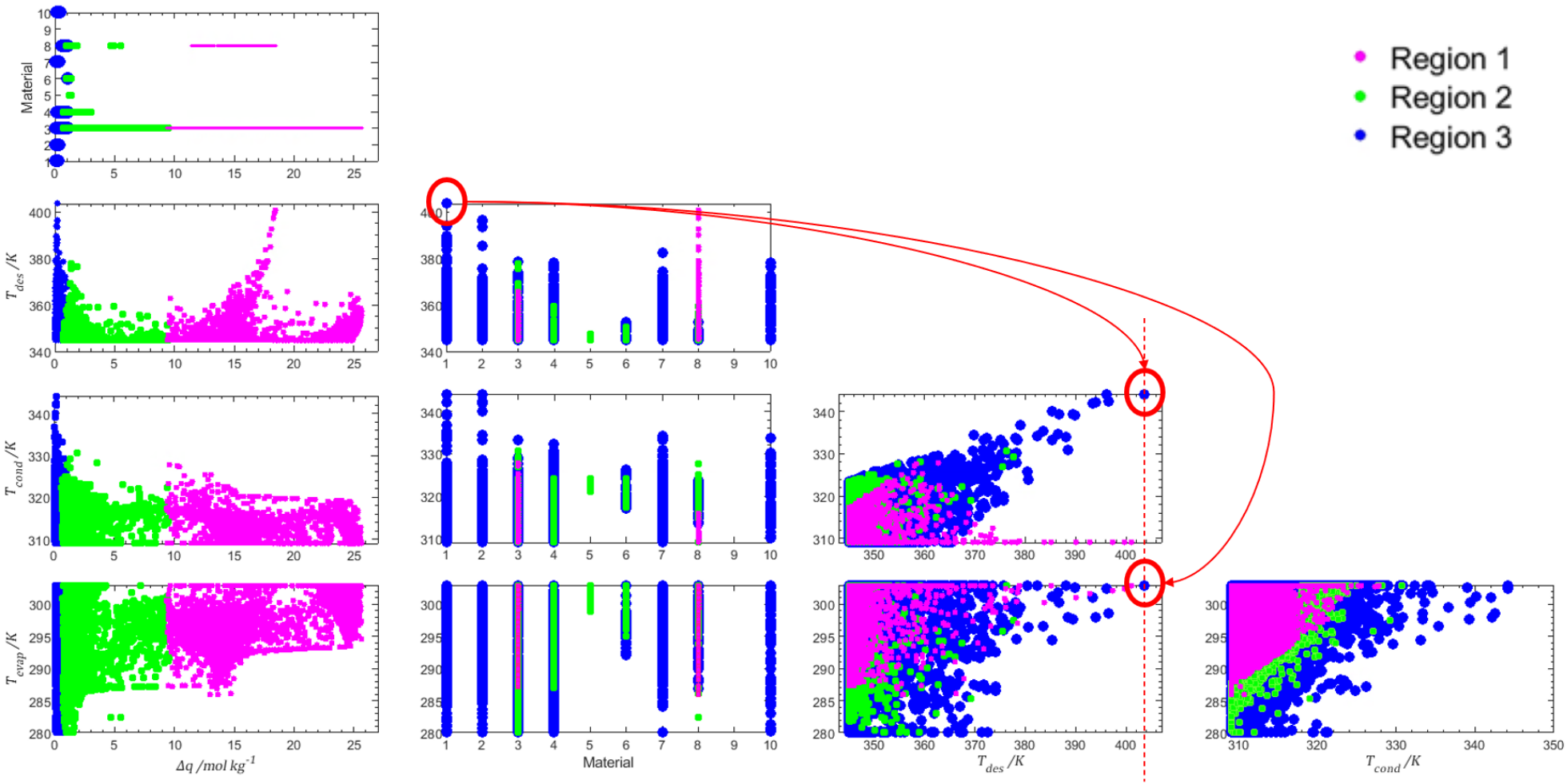

Figure C. 1. Mapping the temperature set and the material corresponding to T_{des} of ≈ 400 K for Region 3.

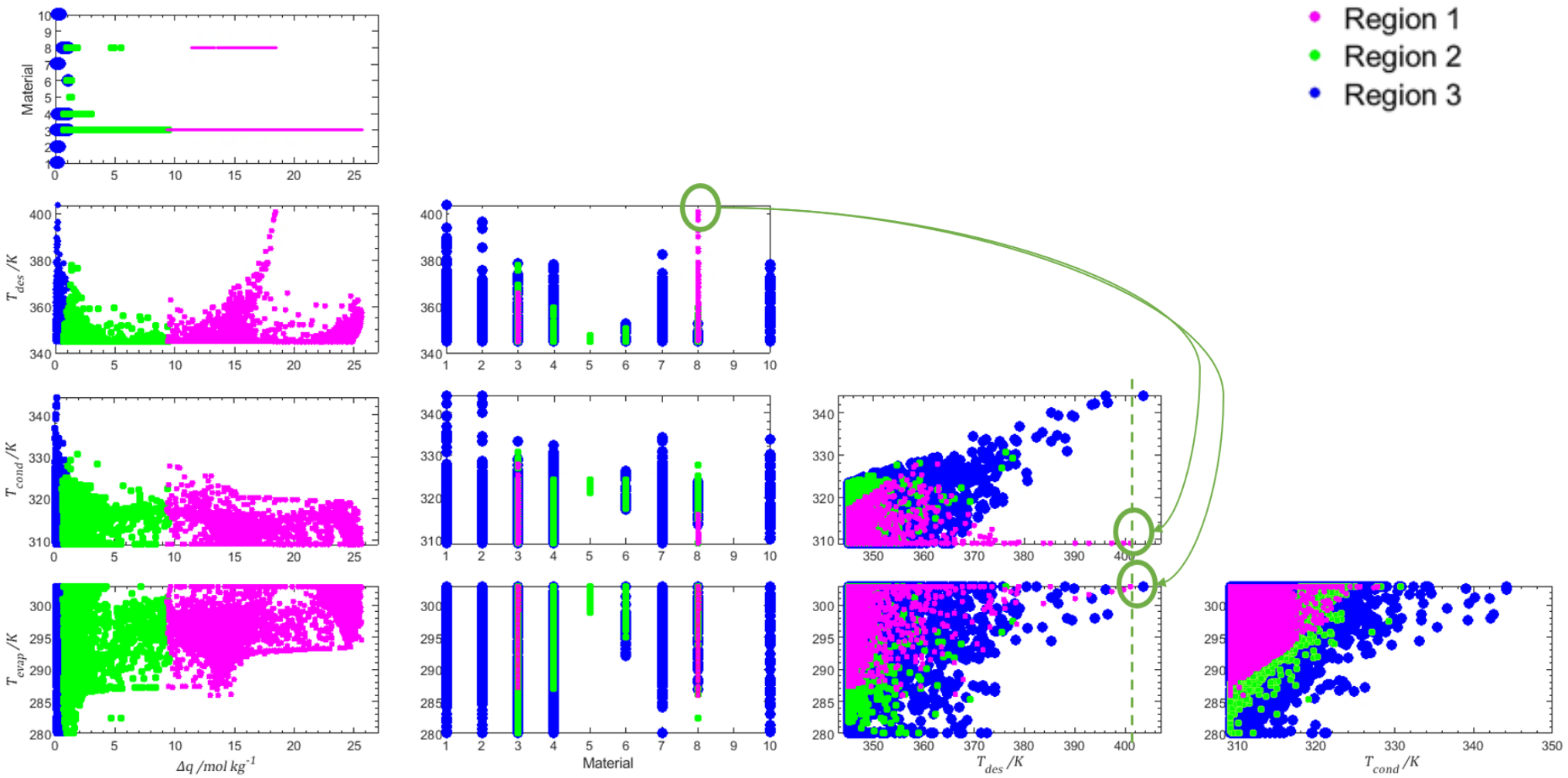

Figure C. 2. Mapping the temperature set and the material corresponding to T_{des} of ≈ 400 K for Region 1.

Appendix D. Appendix references

(1) Silva, M. P.; Ribeiro, A. M.; Silva, C. G.; Ho Cho, K.; Lee, U.-H.; Faria, J. L.; Loureiro, J. M.; Chang, J.-S.; Rodrigues, A. E.; Ferreira, A. Atmospheric Water Harvesting on MIL-100(Fe) upon a Cyclic Adsorption Process. Separation and Purification Technology 2022, 290, 120803. https://doi.org/10.1016/j.seppur.2022.120803.

(2) Silva, M. P.; Ribeiro, A. M.; Silva, C. G.; Narin, G.; Nogueira, I. B. R.; Lee, U.-H.; Faria, J. L.; Loureiro, J. M.; Chang, J.-S.; Rodrigues, A. E.; Ferreira, A. Water Vapor Harvesting by a (P)TSA Process with MIL-125(Ti)_NH2 as Adsorbent. Separation and Purification Technology 2020, 237, 116336. https://doi.org/10.1016/j.seppur.2019.116336.

(3) Silva, M. P.; Ribeiro, A. M.; Silva, C. G.; Nogueira, I. B. R.; Cho, K.-H.; Lee, U.-H.; Faria, J. L.; Loureiro, J. L.; Chang, J.-S.; Rodrigues, A. E.; Ferreira, A. MIL-160(Al) MOF's Potential in Adsorptive Water Harvesting. Adsorption 2021, 27 (2), 213–226. https://doi.org/10.1007/s10450-020-00286-5.

(4) Silva, M. Water Harvesting by Adsorption Based Processes on MOFs. Ph.D. Thesis, Universidade do Porto, 2021.

(5) Kim, K.-M.; Oh, H.-T.; Lim, S.-J.; Ho, K.; Park, Y.; Lee, C.-H. Adsorption Equilibria of Water Vapor on Zeolite 3A, Zeolite 13X, and Dealuminated Y Zeolite. Journal of Chemical & Engineering Data 2016, 61 (4), 1547–1554. https://doi.org/10.1021/acs.jced.5b00927.

(6) Wang, Y. Measurements and Modeling of Water Adsorption Isotherms of Zeolite Linde-Type A Crystals. Industrial & Engineering Chemistry Research 2020, 59 (17), 8304–8314. https://doi.org/10.1021/acs.iecr.9b06891.

(7) Llano-Restrepo, M.; Mosquera, M. A. Accurate Correlation, Thermochemistry, and Structural Interpretation of Equilibrium Adsorption Isotherms of Water Vapor in Zeolite 3A by Means of a Generalized Statistical Thermodynamic Adsorption Model. Fluid Phase Equilibria 2009, 283 (1), 73–88. https://doi.org/10.1016/j.fluid.2009.06.003.

(8) Lin, R.; Ladshaw, A.; Nan, Y.; Liu, J.; Yiacoumi, S.; Tsouris, C.; DePaoli, D. W.; Tavlarides, L. L. Isotherms for Water Adsorption on Molecular Sieve 3A: Influence of Cation Composition. Industrial & Engineering Chemistry Research 2015, 54 (42), 10442–10448. https://doi.org/10.1021/acs.iecr.5b01411.

(9) Gorbach, A.; Stegmaier, M.; Eigenberger, G. Measurement and Modeling of Water Vapor Adsorption on Zeolite 4A—Equilibria and Kinetics. Adsorption 2004, 10 (1), 29–46. https://doi.org/10.1023/B:ADSO.0000024033.60103.ff.

(10) Morris, B. Heats of Sorption in the Crystalline Linde-A Zeolite-Water Vapor System. Journal of Colloid and Interface Science 1968, 28 (1), 149–155.

(11) Grace. Process Adsorbents. https://grace.com/industries/general-industrial/process-adsorbents/ (accessed 2022-03-22).

(12) Wang, Y.; LeVan, M. D. Adsorption Equilibrium of Carbon Dioxide and Water Vapor on Zeolites 5A and 13X and Silica Gel: Pure Components. Journal of Chemical & Engineering Data 2009, 54 (10), 2839–2844. https://doi.org/10.1021/je800900a.

(13) Kim, J.-H.; Lee, C.-H.; Kim, W.-S.; Lee, J.-S.; Kim, J.-T.; Suh, J.-K.; Lee, J.-M. Adsorption Equilibria of Water Vapor on Alumina, Zeolite 13X, and a Zeolite X/Activated Carbon Composite. Journal of Chemical & Engineering Data 2003, 48 (1), 137–141. https://doi.org/10.1021/je0201267.

(14) Son, K. N.; Richardson, T.-M. J.; Cmarik, G. E. Equilibrium Adsorption Isotherms for H2O on Zeolite 13X. Journal of Chemical & Engineering Data 2019, 64 (3), 1063–1071. https://doi.org/10.1021/acs.jced.8b00961.

(15) Sun, B.; Chakraborty, A. Thermodynamic Formalism of Water Uptakes on Solid Porous Adsorbents for Adsorption Cooling Applications. Applied Physics Letters 2014, 104 (20), 201901. https://doi.org/10.1063/1.4876922.

(16) Wei Benjamin Teo, H.; Chakraborty, A.; Fan, W. Improved Adsorption Characteristics Data for AQSOA Types Zeolites and Water Systems under Static and Dynamic Conditions. Microporous and Mesoporous Materials 2017, 242, 109–117. https://doi.org/10.1016/j.micromeso.2017.01.015.

(17) Luo, Y.; Funke, H. H.; Falconer, J. L.; Noble, R. D. Adsorption of CO2, CH4, C3H8, and H2O in SSZ-13, SAPO-34, and T-Type Zeolites. Industrial & Engineering Chemistry Research 2016, 55 (36), 9749–9757. https://doi.org/10.1021/acs.iecr.6b02034.

(18) Fasano, M.; Falciani, G.; Brancato, V.; Palomba, V.; Asinari, P.; Chiavazzo, E.; Frazzica, A. Atomistic Modelling of Water Transport and Adsorption Mechanisms in Silicoaluminophosphate for Thermal Energy Storage. Applied Thermal Engineering 2019, 160, 114075. https://doi.org/10.1016/j.applthermaleng.2019.114075.

(19) Hussein, E. Numerical and Experimental Evaluation of Advanced Metal-Organic Framework Materials for Adsorption Heat Pumps. Ph.D. thesis, University of Birmingham, 2018.

(20) Gordeeva, L. G.; Solovyeva, M. v; Aristov, Y. I. NH2-MIL-125 as a Promising Material for Adsorptive Heat Transformation and Storage. Energy 2016, 100, 18–24. https://doi.org/https://doi.org/10.1016/j.energy.2016.01.034.

(21) Cui, S.; Marandi, A.; Lebourleux, G.; Thimon, M.; Bourdon, M.; Chen, C.; Severino, M. I.; Steggles, V.; Nouar, F.; Serre, C. Heat Properties of a Hydrophilic Carboxylate-Based MOF for Water Adsorption Applications. Applied Thermal Engineering 2019, 161, 114135. https://doi.org/10.1016/j.applthermaleng.2019.114135.

(22) Fröhlich, D.; Pantatosaki, E.; Kolokathis, P. D.; Markey, K.; Reinsch, H.; Baumgartner, M.; van der Veen, M. A.; de Vos, D. E.; Stock, N.; Papadopoulos, G. K.; Henninger, S. K.; Janiak, C. Water Adsorption Behaviour of CAU-10-H: A Thorough Investigation of Its Structure–Property Relationships. Journal of Materials Chemistry A 2016, 4 (30), 11859–11869. https://doi.org/10.1039/C6TA01757F.

(23) Jahan, I.; Islam, Md. A.; Palash, M. L.; Rocky, K. A.; Rupam, T. H.; Saha, B. B. Experimental Study on the Influence of Metal Doping on Thermophysical Properties of Porous Aluminum Fumarate. Heat Transfer Engineering 2021, 42 (13–14), 1132–1141. https://doi.org/10.1080/01457632.2020.1777005.

(24) Simo, M.; Sivashanmugam, S.; Brown, C. J.; Hlavacek, V. Adsorption/Desorption of Water and Ethanol on 3A Zeolite in Near-Adiabatic Fixed Bed. Industrial & Engineering Chemistry Research 2009, 48 (20), 9247–9260. https://doi.org/10.1021/ie900446v.

(25) Bakhtyari, A.; Mofarahi, M. Pure and Binary Adsorption Equilibria of Methane and Nitrogen on Zeolite 5A. Journal of Chemical & Engineering Data 2014, 59 (3), 626–639. https://doi.org/10.1021/je4005036.

(26) Lu, X.; Wang, Y.; Estel, L.; Kumar, N.; Grénman, H.; Leveneur, S. Evolution of Specific Heat Capacity with Temperature for Typical Supports Used for Heterogeneous Catalysts. Processes 2020, 8 (8). https://doi.org/10.3390/pr8080911.

(27) Kakiuchi, H.; Iwade, M.; Shimooka, S.; Ooshima, K.; Yamazaki, M.; Takewaki, T. Novel Zeolite Adsorbents and Their Application for AHP and Desiccant System. IEA-Annex 2005, 17.